Ph.D. degree in Systems Medicine

Curriculum in Human Genetics

European School of Molecular Medicine (SEMM)

University of Milan and University of Naples "Federico II"

Disciplinary sector: MED/03

AIRWAY SURFACE HYPERVISCOSITY AND DEFECTIVE MUCOCILIARY TRANSPORT BY IL-17/TNF-α ARE CORRECTED BY β-ADRENERGIC STIMULUS

Daniela Guidone

Telethon Institute of Genetics and Medicine (TIGEM)

University ID No.: R12695

Supervisor: Prof. Luis J.V. Galietta

External advisor: Prof. Gilles Crambert

Internal advisor: Prof. Roman Polishchuk

External examiner: Prof. Marcus A. Mall

Internal examiner: Prof. Mirko Cortese

Academic Year 2022-2023

INDEX

ABSTRACT

The fluid covering the surface of airway epithelia represents a first barrier against pathogens. The chemical and physical properties of the airway surface fluid are controlled by the activity of ion channels and transporters. In cystic fibrosis (CF), loss of CFTR chloride channel function causes airway surface dehydration, bacterial infection, and inflammation. We investigated the effects of IL-17A plus TNF-α, two cytokines with relevant roles in CF and other chronic lung diseases. Transcriptome analysis revealed a profound change with upregulation of several genes involved in ion transport, antibacterial defense, and neutrophil recruitment. At the functional level, bronchial epithelia treated in vitro with the cytokine combination showed upregulation of ENaC channel, ATP12A proton pump, ADRB2 β-adrenergic receptor, and SLC26A4 anion exchanger. The overall result of IL-17A/TNF-α treatment was hyperviscosity of the airway surface, as demonstrated by fluorescence recovery after photobleaching (FRAP) experiments. Importantly, stimulation with a β-adrenergic agonist switched airway surface to a low-viscosity state in non-CF but not in CF epithelia. Our study suggests that CF lung disease is sustained by a vicious cycle in which epithelia cannot exit from the hyperviscous state, thus perpetuating the proinflammatory airway surface condition.

1 INTRODUCTION

1.1 The human respiratory system

The respiratory system is a complex arrangement of organs and tissues involved in the breathing process. The upper airways include the nose, the oral cavity, the pharynx and the portion of the larynx above the vocal cords. They represent the air entryway and have the major role in filtering unwanted contaminants, maintaining the lower airways in a nearly sterile condition. The lower airways are divided into two parts. The first part is the conducting zone, that includes the portion of the larynx below the vocal cords, the trachea that bifurcates into left and right primary bronchi, which then enter the lungs on each side, followed by branching into secondary and tertiary bronchi. The second part is the respiratory zone, with the respiratory bronchioles and the alveoli, in which the exchange between oxygen and carbon dioxide occurs (Saint-Criq & Gray, 2017; Bustamante-Marin & Ostrowski, 2017).

1.2 Structure and cell composition of the surface airway epithelium

The inner surface of human airways is covered by a continuous layer of epithelial cells connected by tight junctions, forming a resistant barrier. The epithelial layer is sustained by a collagenous lamina propria, a connective tissue containing serous and mucous glands (Bustamante-Marin & Ostrowski, 2017). The epithelial cells are polarized: the membrane in touch with the connective tissue is called basolateral, whereas the side facing the external environment is named apical membrane (Saint-Criq & Gray, 2017). The airway epithelium progressively differs between large and small airways: in the large proximal airways it is pseudostratified, highly ciliated and taller, with columnar cells (about 50 μm) (Widdicombe, 2002); instead, in the small distal airways it becomes thinner and cuboidal (Figure 1) (Crystal et al., 2008).

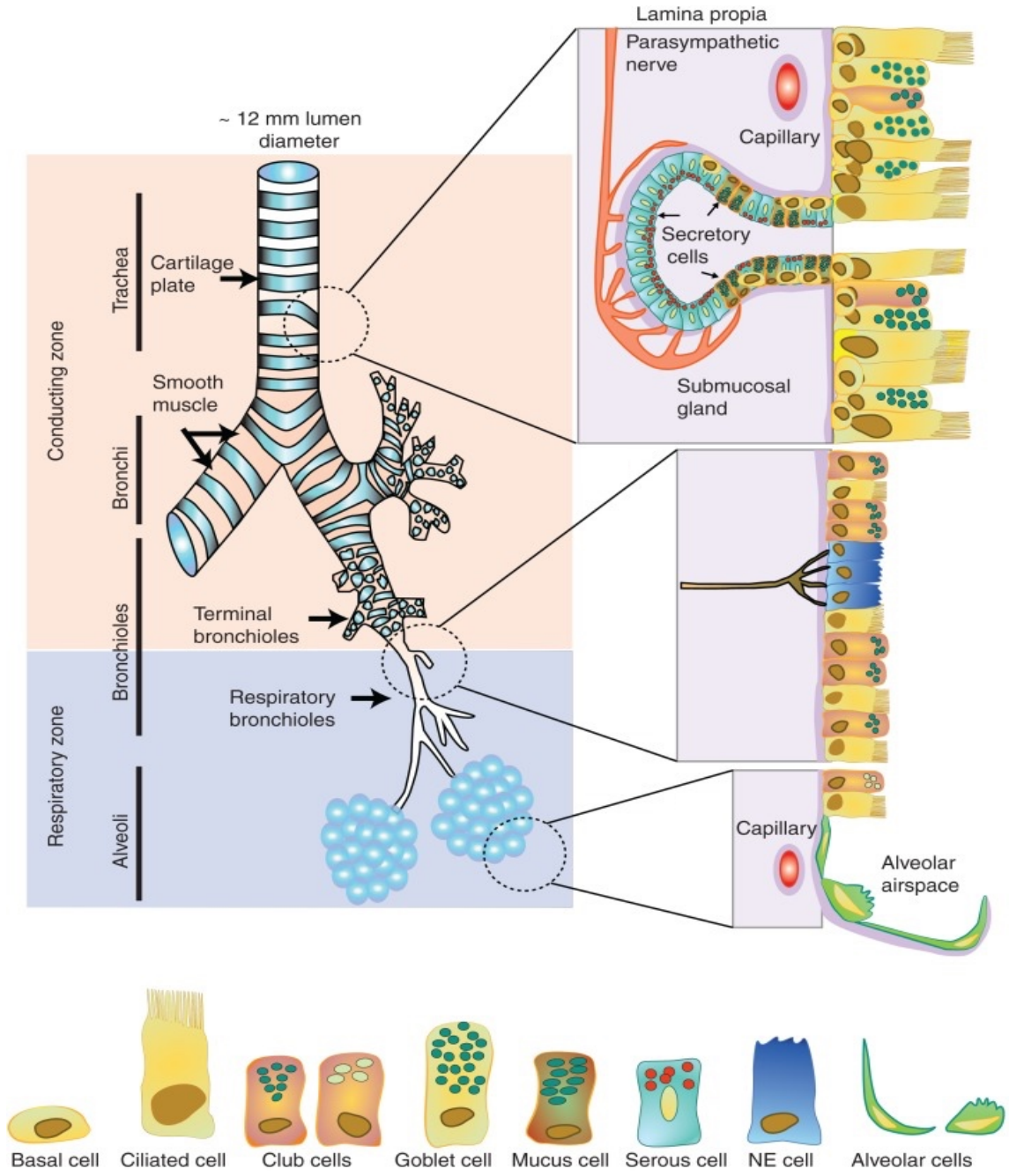

Figure 1. Schematic representation of human respiratory system. The image shows the separation between conducting and respiratory zones and how the respiratory system branches into bronchi, bronchioles and alveoli. In the bottom part, the cell types that compose the epithelial surface are indicated. Adapted from Bustamante-Marin & Ostrowski, 2017.

The epithelium consists of three main cell types: ciliated cells, goblet cells and basal cells. However, recent single cell RNAseq (scRNAseq) and in vivo lineage tracking techniques revealed the presence of novel cell types, such as neuroendocrine cells, tuft cells, and ionocytes. The distribution of these cells varies along the proximal-distal airways to achieve the local specific respiratory function (Ruysseveldt et al., 2021).

A population of multipotent stem cells p63- and KRT5-positive, called basal cells for their proximity to the underlying basal lamina, represents around 30% of the total cell population in the upper airways, whereas their number decreases to 6% in distal airways. They are found deeper in the epithelium, where they are protected from the external environment (Ruysseveldt et al., 2021). They are the principal stem cells of the airways and are responsible for the self-renewal and the differentiation of specialized cell types that compose the epithelial layer (Rock J.R. et al., 2009; Rock J.R. & Hogan, 2011). Basal cells are quiescent in the intact epithelium, with a relatively slow turnover, but they become active upon injury. Recently, also Hillock cells have been identified as another type of basal progenitor cells, but their function is still unknown (Ruysseveldt et al., 2021). Moreover, committed lung epithelial cells such as “club cells”, which are characterized by the SCGB1A1 marker, have the capacity to dedifferentiate and act as airway progenitor cells. In the small airways, in which the number of basal cells is particularly low, dedifferentiation of club cells is the main source of cells dedicated to tissue repair, although a population of bronchioalveolar stem cells (BASCs) has been reported to be involved in lung repair and regeneration (Liu et al., 2019).

1.2.1 Ciliated cells

Ciliated cells represent the 60% of epithelial cells in healthy airways. They are tall, columnar and terminally differentiated cells of the surface epithelium, enriched in mitochondria that produce high abundance of ATP as energy for ciliary beating. The differentiation process is dependent on Notch signaling pathway, whose inhibition turns on MCIDAS and consequently FOXJ1 expression. Given its role as master regulator of basal body docking, cilia formation and motility, FOXJ1 is considered a marker of ciliated cells. The basal bodies are docked to the apical membrane and allow the growth of cilia. One ciliated cell has more than 100 cilia on its surface. A single cilium is 6-7 μm long and has a diameter of 0.1 μm. The internal structure consists of 9+2 axonemes.

The nine outer doublet microtubules are formed by a complete A tubule and a partial B tubule, whereas the two microtubules forming the central pair are single complete microtubules. The radial spokes connect the outer and the central microtubules. The dynein arms connect the doublets microtubules, divided into outer dynein arms (ODA) and inner dynein arms (IDA), responsible for ciliary beat frequency (CBF) and waveform, respectively. The cilia beat in a whip-like motion and in a phase-shifted manner, generating a synchronous wave that moves toward the oro-pharynx (Figure 2).

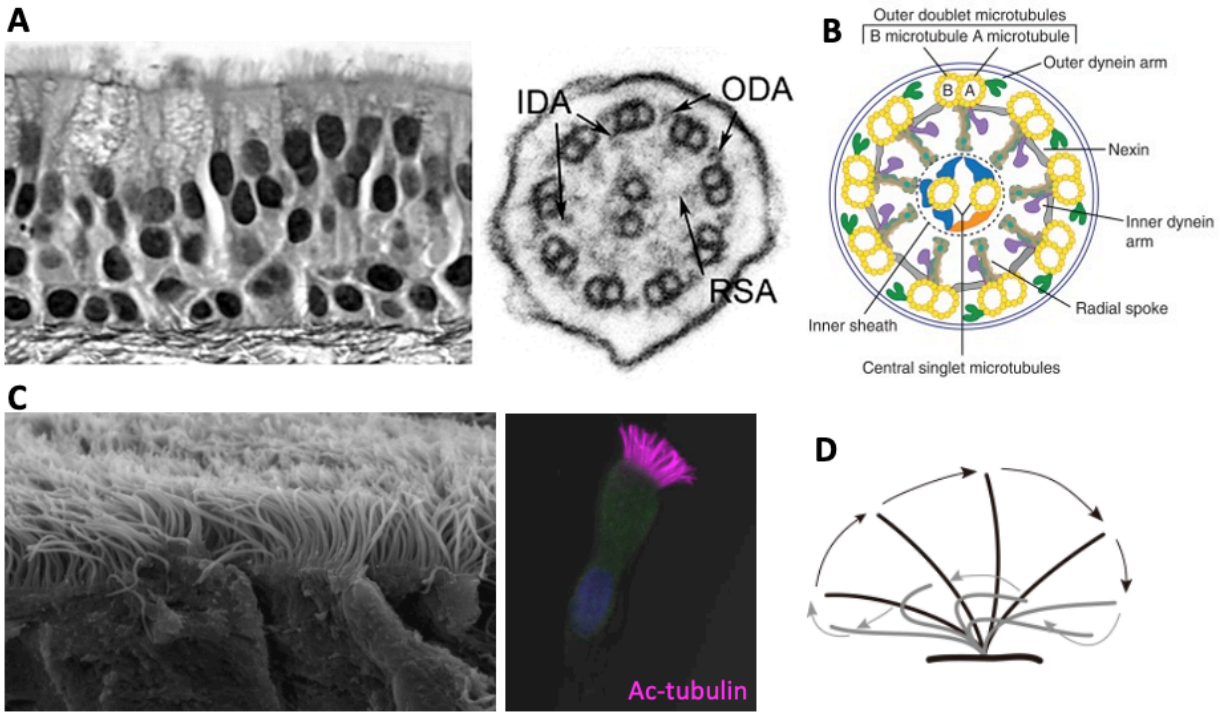

Figure 2. Ciliated cells, axonemal structure and ciliary beating. A, left: cilia localization in a human tracheobronchial epithelial cell culture. **A, right:** cross-section view of cilia axonemal structure by TEM microscopy. Modified from Livraghi & Randell, 2007. **B:** schematic representation of axonemal structure. Adapted from Bustamante-Marin & Ostrowski, 2017. **C, left:** image of nasal epithelium by SEM. Adapted from Gudis et al., 2012. **C, right:** immunofluorescence of ciliated cell from nasal brushing, staining for acetylated tubulin (Ac-tubulin, magenta). **D:** diagram of ciliary beat cycle. Adapted from Raidt et al., 2014.

In healthy human airways, the CBF has a frequency of 10-20 Hz, and it can increase upon different stimuli such as β-adrenergic or purinergic stimulation, intracellular cyclic-AMP (cAMP) or calcium (Ca^{2+}) elevation. CBF is also temperature-dependent (high temperature increases ciliary beating) and pH dependent (intracellular alkaline pH stimulates ciliary beating). Cilia are chemosensory organelles also expressing taste receptors, that sense noxious molecules and respond to them increasing CBF (Bustamante-Marin & Ostrowski, 2017). Primary ciliary dyskinesia (PCD) is a severe respiratory disease caused by mutations in genes involved in structure and function of motile cilia (Kurkowiak et al., 2015). However, in other chronic respiratory diseases such as CF, asthma, chronic obstructive pulmonary disease (COPD), despite normal cilia formation, their motility and function are impaired by other factors like mucus hyperproduction and collapse of airway surface liquid (ASL) (Knowles & Boucher, 2002), as discussed in the following paragraphs.

1.2.2 Goblet cells

The goblet cells are the main secretory cells within the surface epithelium, corresponding to 20% of epithelial cells in normal airways. They are highly polarized, with the nucleus and the organelles in the basal compartment. The apical cytoplasm is enlarged and full of mucins granules, that are secreted upon different autocrine and paracrine stimuli, in particular extracellular ATP (Bustamante-Marin & Ostrowski, 2017).

Mucins are cysteine-rich glycoproteins of high molecular weight classified as membrane-associated mucins (e.g., MUC1, MUC4, MUC16 and MUC20) and secreted mucins (e.g., MUC5AC and MUC5B). They are synthetized as polymers and receive post-translational modifications through the endoplasmic reticulum and Golgi network. In particular, glycosylation and disulfide bond formation are important for mucins network. Secreted mucins are stored in intracellular granules, in which they are compacted and dehydrated at a low pH (~5.5) and in presence of Ca^{2+} ions. Upon different stimulations, mucus is released through the replacement of Ca^{2+} ions with sodium (Na^{+}) ions (Ridley & Thornton, 2018). In this process, bicarbonate (HCO_3^{-}) is considered fundamental to alkalinize pH, neutralize protons (H^{+}) and Ca^{2+} ions and support mucus release and expansion (Figure 3) (Garcia et al., 2009; Gustafsson et al., 2012).

MUC5B is the most expressed secreted mucin in healthy airways (Bustamante-Marin & Ostrowski, 2017) and is predominantly involved in the response to bacterial infection and inflammation. It is secreted by submucosal glands in the upper airways and by goblet cells in the distal airways in the form of mucus strands and bundles. MUC5AC is less produced in normal airways but increases in response to different stimuli such as viral infections, asthma, allergies. It is mainly produced by epithelial surface goblet cells, for which is considered a specific marker, and released in threads. On the surface, MUC5B filaments can be partially covered by MUC5AC mucin.

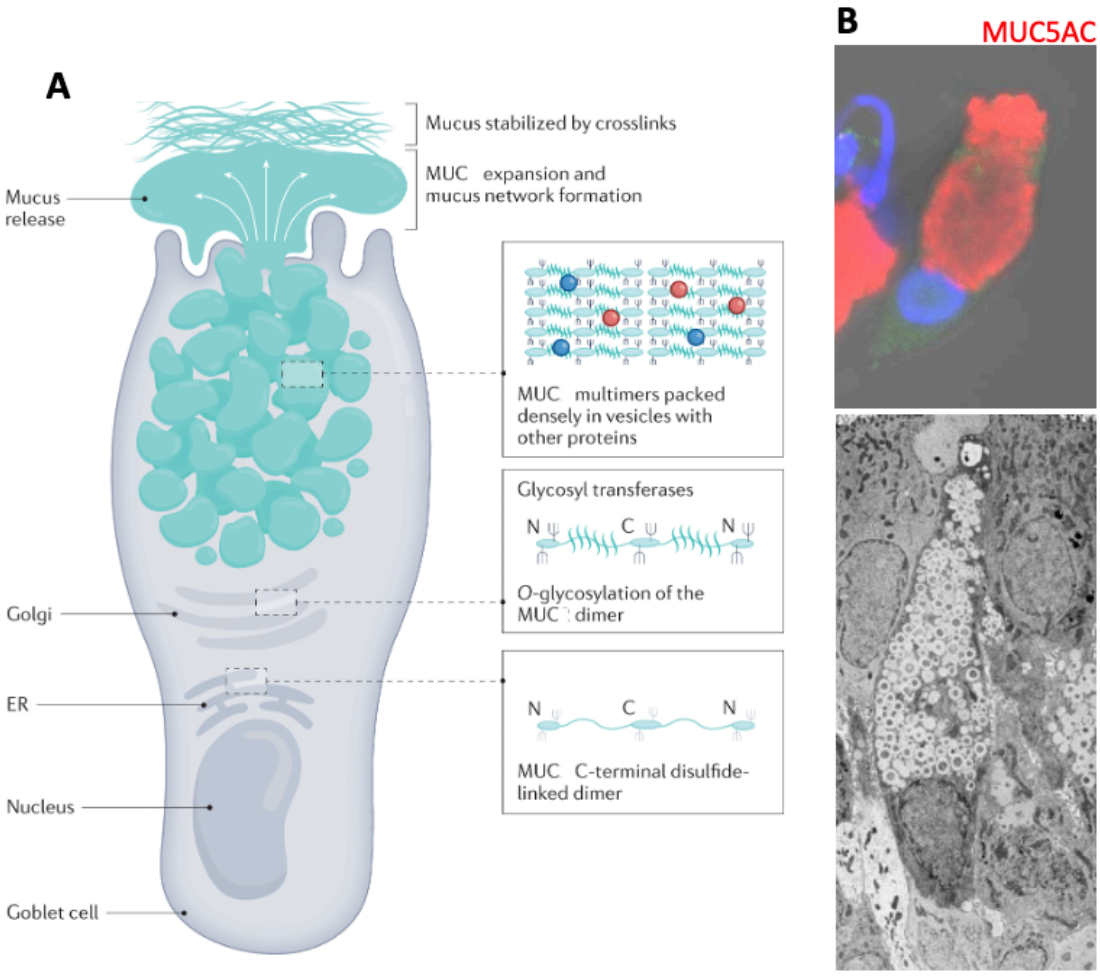

Figure 3. Structure and function of goblet cells. A: schematic representation of mucus production, packaging, expansion and release from a goblet cell. Modified from Gustaffson & Johansson, 2022. **B, top:** immunofluorescence of goblet cell from nasal brushing, staining for MUC5AC (red). **B, bottom:** image of tracheal guinea pig goblet cell by TEM. Adapted from Kondo et al., 2002.

Alterations of mucin granules storage, secretion and expansion, formation of cross-links, high concentration of mucins or changes in MUC5AC/MUC5B ratio may hamper the airway clearance. These processes are dependent on hydration, pH and HCO_3^- content of the airway surface (Ridley & Thornton, 2018). Mucus hyperproduction is a common feature of chronic lung diseases. Healthy airways contain relatively few mucous cells, that increase upon different inflammatory stimuli, in a pathological condition defined as mucous metaplasia (Evans et al., 2004).

1.2.3 Ionocytes and other rare cell types

Recent studies have completely revised the classification of cell types that compose the airway epithelium (Montoro et al. 2018, Plasschaert et al., 2018), identifying new rare cell types with specific functions, which are still poorly understood, but seem to involve the capacity of the epithelia to sense and respond to environmental stimuli. One rare cell type is represented by the Pulmonary Neuroendocrine Cells (PNeC), which are less than 0.5% of cells in the airway epithelium (Boers et al., 1996). They are present in the proximal airways and have neuroendocrine capability: they can sense chemical or mechanical stimuli and can generate immune and nervous system responses by releasing neuropeptides and neurotransmitters, functioning as "airway sensors" (Xu et al., 2020). The second type consists of Tuft cells that act as chemosensory cells expressing taste-sensing genes or immune-related genes. They are probably involved in sensing bacterial components and trigger the immune response and cytokine production (Xu et al., 2020; Montoro et al., 2018; Plasschaert et al., 2018). Finally, ionocytes, which were previously found in the gills of fish and skin of amphibia, is the third type of epithelial cells found by scRNAseq. The term "ionocyte" derives from the abundant expression of genes involved in ion transport. A specific marker of ionocytes is FOXI1, but they also express high levels of Cystic Fibrosis Transmembrane conductance Regulator (CFTR, the channel involved in CF) and vacuolar (V)-ATPase, thus highlighting their importance in airway surface physiology, pH regulation and mucus viscosity (Montoro et al., 2018, Plasschaert et al., 2018). Ionocytes are more present in nasal cells respect to bronchial epithelial cells, suggesting the presence of a proximal-distal gradient through the airways (Figure 4) (Scudieri et al., 2020).

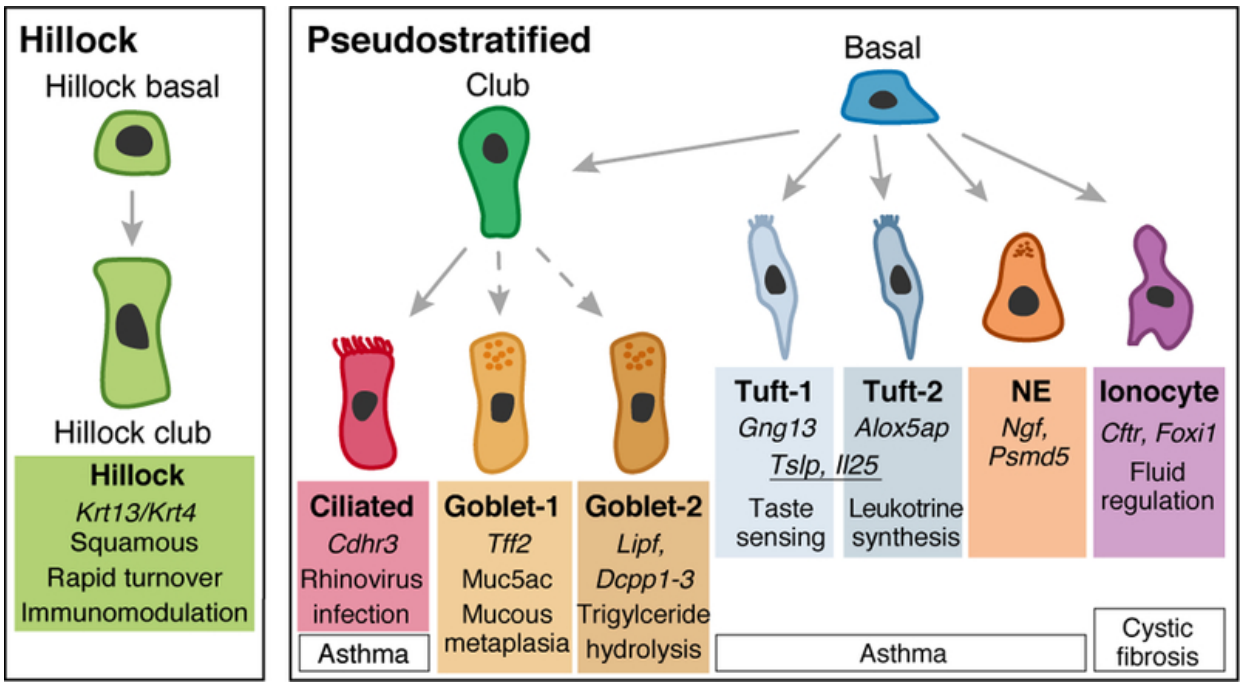

Figure 4. New schematic representation of cell types that compose the airway epithelium. Beside basal, ciliated and goblet cells, new rare cell types (Tuft, PNeC, ionocytes, Hillock) have been identified. Adapted from Montoro et al., 2018.

1.3 Airway Surface Liquid (ASL) properties and composition

The ASL is formed by two layers, the periciliary liquid (PCL) and the mucus layer (ML) (Knowles & Boucher, 2002). The PCL is a 5-8 μm thick (Ridley & Thornton, 2018) continuous, low-viscosity solution formed by glycolipids and membrane-anchored mucins, in which the cilia are immerged. The PCL is crucial both for proper and rapid cilia beating and as a shield for the underlying epithelium. Moreover, the lubricating function of the PCL allows the mucus movement during cough clearance (Knowles & Boucher, 2002). The thickness, pH and hydration state of the PCL are tightly regulated by a fine balance between fluid and electrolyte absorption and secretion. Above the PCL there is the ML, a 2-5 μm thick layer of a tangled net of mucins, mainly MUC5B and MUC5AC, that cover the epithelial surface (Knowles & Boucher, 2002). The ML is considered discontinuous in human airways, with some zones in which is deeper and some mucus-free zones in which PCL is exposed to the air (Knowles & Boucher, 2002). The cilia tips contact the ML, moving it in a rotational way and in a proximal direction through the airways (Bustamante-Marin & Ostrowski, 2017).

The mucociliary clearance (MCC) is the process obtained by the coordinated and dynamic activity of mucus and cilia: the goblet cells release mucins, that trap pathogens and particles from the air, then the cilia beating propel mucus in direction of the mouth where it is swallowed or expectorated (Widdicombe, 2002). The average basal rate of mucociliary transport is 5.5 mm/min, but various physiological factors, such as age, sex, posture, sleep, exercise, temperature and humidity conditions, may affect this value. Moreover, the number and length of cilia, the CBF, as well as mucus rheology and hydration, may influence MCC (Bustamante-Marin & Ostrowski, 2017). Since the epithelial system is non-innervated, the rate of MCC seems to be locally regulated by nucleotide release in response to cough-induced shear stress, that act as an autocrine and paracrine stimulus on epithelial ion transport, CBF, and mucus secretion (Button et al., 2013; Knowles & Boucher, 2002).

Alterations of MCC and ASL are a common feature of many chronic respiratory diseases such as asthma, COPD, PCD and CF, thus highlighting their fundamental functional role in the airway physiology (Mall, 2008; Button et al., 2012). The importance of MCC process is demonstrated by the different features displayed in PCD and CF lung diseases. PCD patients have alterations of

ciliary functions but, despite this, they have a milder respiratory disease compared to CF, since normal ASL and cough-dependent mucus clearance are preserved. In CF, active fluid absorption (Na^+ transport) cannot be contrasted by chloride (Cl^-) secretion through CFTR, with consequently reduced content of water in the ASL. This causes the collapse of the ML into the PCL, gluing secreted and anchored-membrane mucins in a dense stuck of mucus that impairs cilia movement and both mucociliary and cough clearance. Adherent mucus plaques create an environment favoring bacterial infection and chronic inflammation with progressive lung failure (Figure 5) (Knowles & Boucher, 2002; Ridley & Thornton, 2018; Higgings et al., 2015).

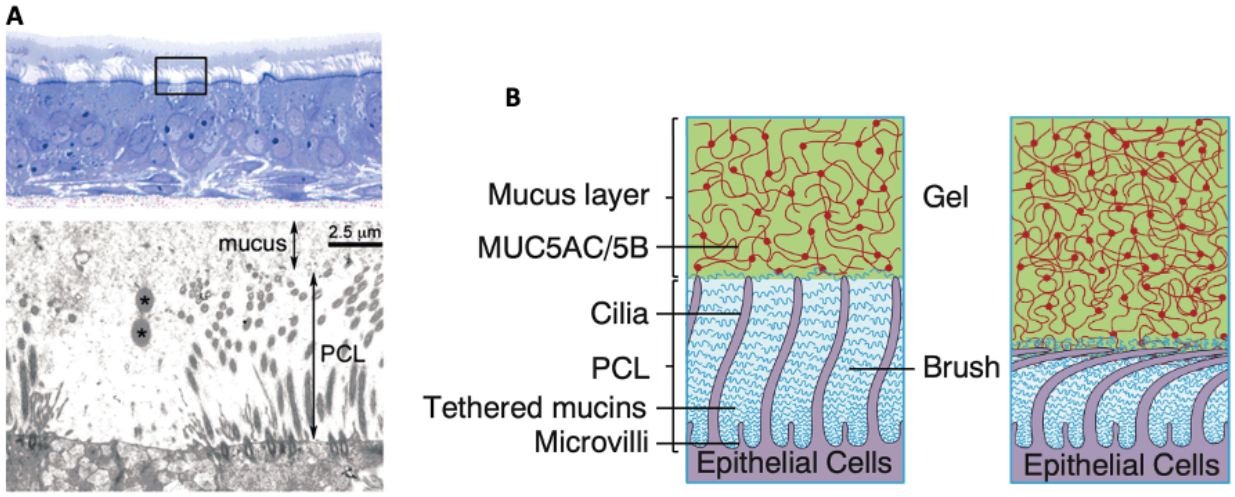

Figure 5. ASL composition. **A, top:** perfluorocarbon-OsO_4 fixation of cultured human tracheobronchial epithelial cells preserves PCL and ML structure. **A, bottom:** TEM of the black box area indicated in the top image, in which PCL an ML are indicated. Modified from Livraghi & Randell, 2007. **B:** schematic representation of normal and collapsed PCL and ML. Adapted from Button et al., 2012.

1.4 Transepithelial ion transport

The chemical and physical properties of the ASL (composition, pH, thickness, hydration) are finely tuned by the coordinated activity of a variety of ion channels, active transporters, ion exchangers and cotransporters, which control airway surface properties moving ions, other solutes, and water through the airway epithelium (Bartoszewski et al., 2017). The overall effect on the ASL involves the combinatorial activity of all channels and transporters in response to a plethora of different stimuli. Despite the complexity of the transepithelial ion transport network, elucidation of its regulation represents a fundamental aim to better understand molecular mechanisms occurring in lungs under healthy and pathological conditions (Figure 6) (Bartoszewski et al., 2017).

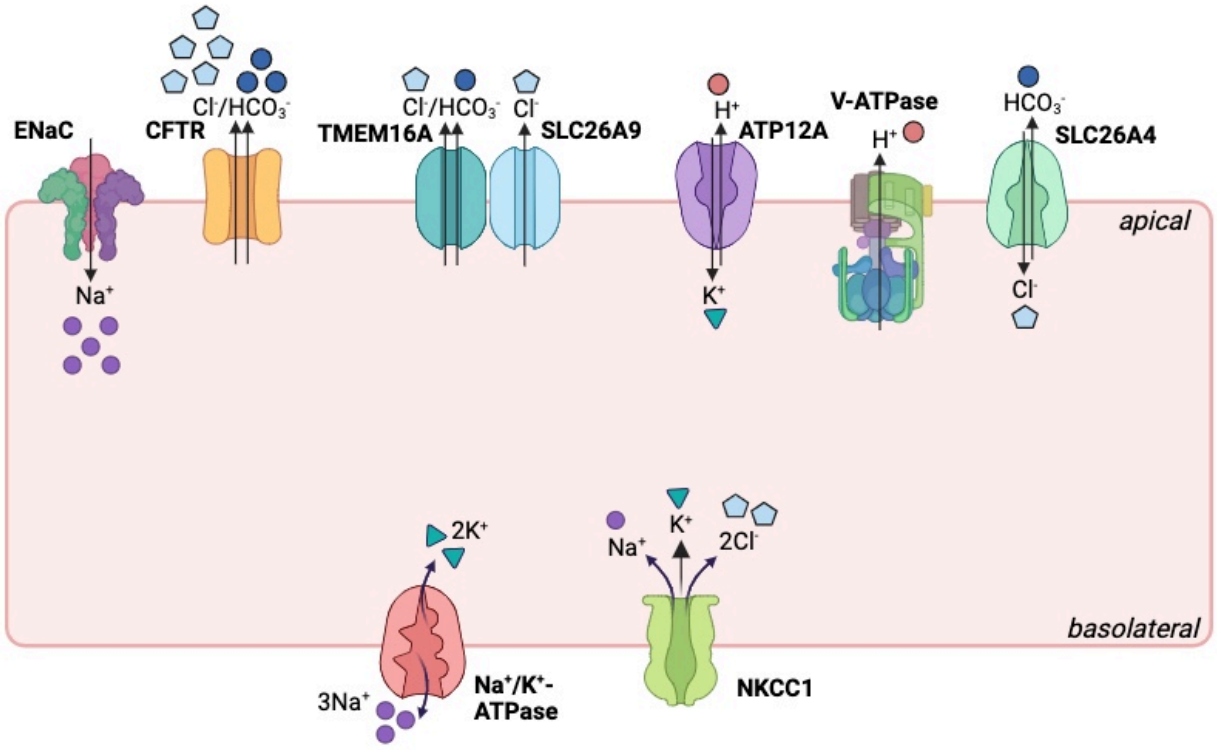

Figure 6. Schematic representation of transepithelial ion transport (simplified). The cartoon shows main ion channels and transporters that are expressed in the airway epithelial cells. The ion transport activity is indicated for each of them. This model does not depict other channels and transporters that are not taken into consideration in the following paragraphs and their differential expression in different cell types. Created with Biorender.com.

1.4.1 The Epithelial Sodium Channel (ENaC): sodium and fluid absorption

ENaC is an ion channel expressed in the apical membrane of different tissues where it is responsible for Na^+ flux from the external fluid into the cells. This process, coupled with water absorption by osmosis, contributes to salt absorption (Saint-Criq & Gray, 2017) and ASL dehydration. The driving force for apical Na^+ reabsorption through ENaC is the basolateral Na^+-K^+-ATPase activity, that transports Na^+ out and pumps potassium (K^+) inside the cell (Saint-Criq & Gray, 2017; Bartoszewski et al., 2017). ENaC regulates Na^+ balance, blood volume and pressure in aldosterone-responsive epithelia (kidney and colon), whereas control fluid reabsorption and mucus transport in glucocorticoid-responsive epithelia as the airways (Rossier & Stutts, 2009). ENaC is also involved in amniotic fluid reabsorption in the lungs at birth (Helve et al., 2009) and in the resolution of pulmonary edema (Rossier & Stutts, 2009).

ENaC is composed by three subunits (α, β, γ; gene names SCNN1A, SCNN1B, SCNN1G, respectively) that form a channel high selective for Na^+ and sensitive to the pore-blocker amiloride (Ki = 0.1 μM). Each subunit is formed by a large extracellular loop hand-like shaped, two transmembrane domains and short cytoplasmic tails formed by N- and C-termini (Rossier & Stutts, 2009; Gaillard et al., 2010). In addition to α, β and γ subunits, a novel subunit (δ; gene name SCNN1D), has been described (Bartoszewski et al., 2017). The δ subunit can replace the α, generating δβγ ENaC heterotrimers with ten-fold increase in amiloride-sensitive current. The δ subunit seems to promote γ subunit cleavage, constitutively activating the channel (Figure 7) (Gaillard et al., 2010).

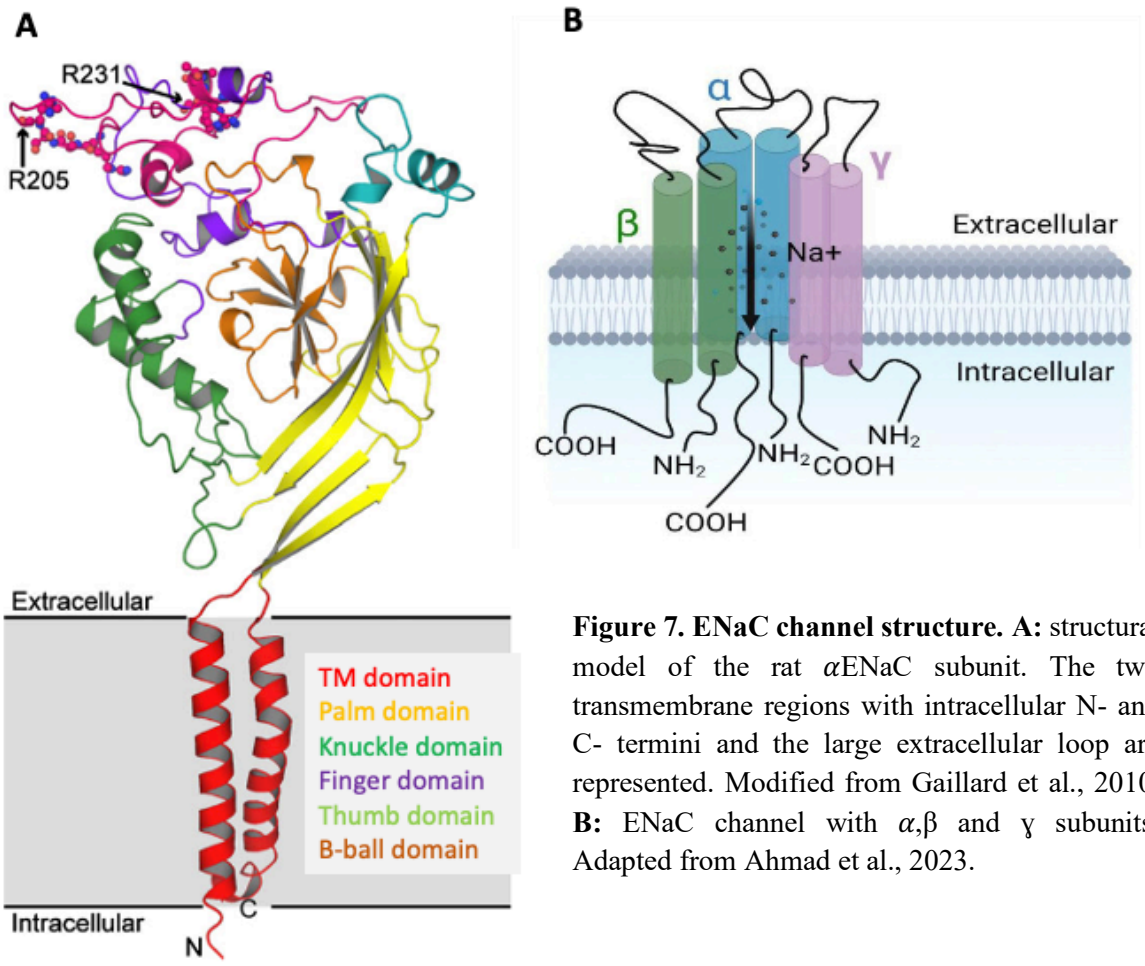

Figure 7. ENaC channel structure. A: structural model of the rat αENaC subunit. The two transmembrane regions with intracellular N- and C- termini and the large extracellular loop are represented. Modified from Gaillard et al., 2010. **B:** ENaC channel with α,β and ɣ subunits. Adapted from Ahmad et al., 2023.

A variety of physiological, environmental and genetic factors may modulate ENaC channel (Bartoszewski et al., 2017), influencing both the number of channels expressed at the plasma membrane and the channel gating. In particular, the presence of channels in the plasma membrane is mostly dependent on intracellular second messenger regulation, whereas the channel open probability depends on proteolytic regulation (Gaillard et al., 2010).

Intracellular second messenger regulation: a link between ENaC and chloride channels

Activation of purinergic receptors on the apical membrane through ATP or UTP stimuli and consequent intracellular Ca^{2+} elevation inhibit ENaC. ENaC is not directly Ca^{2+}-sensitive, but it is stabilized in the membrane by PIP_3 and PIP_2, so its inhibition is due to PIP_2 degradation through phospholipase C (Shei et al., 2018). In the same way, cAMP-elevating agents such as adenosine, forskolin or isoproterenol inhibit ENaC (Gaillard et al., 2010). Both Ca^{2+} and cAMP stimulates also Cl^- secretion through TMEM16A and CFTR, respectively. Moreover, ENaC activity is influenced by the potential difference across the apical membrane (Shei et al., 2018). A reduction of intracellular Cl^- concentration due to CFTR or TMEM16A stimulation further inhibits ENaC (Gaillard et al., 2010).

In general, activation of Cl^- secretion paralleled to Na^+ absorption inhibition is a way to switch the epithelium from absorptive state to secretory state (Saint-Criq & Gray, 2017). It is not surprising that these two activities need to be balanced relative to each other, given their common role in regulating ASL volume and salt balance.

The functional link between ENaC and CFTR has been discussed for many years and different research groups support the idea that ENaC is directly involved in the development of CF disease. The "low volume hypothesis" is based on the concept that CFTR is both a Cl^- channel and an ENaC regulator. Indeed, some authors report that in airway epithelia of CF patients, loss of functional CFTR promotes increase in ENaC activity, and Na^+ hyperabsorption contributes to worsen the airway dehydration caused by loss of CFTR-dependent fluid secretion (Boucher et al., 1988; Mall et al., 1998; Mall et al., 2004; Collawn et al., 2012; Bartoszewski et al., 2017). This hypothesis is supported by the fact that mice overexpressing β-ENaC mimic CFTR disease, showing airway obstruction, dehydrated mucus, neutrophilic inflammation and infections (Mall et al., 2004; Collawn et al., 2012). The hyperactivity of ENaC in CF has been questioned by others. Indeed, the team of Michael Welsh and coll. at the University of Iowa reported that there is no evidence of elevated Na^+ transport in CF human primary cultures respect to non-CF (Itani et al., 2011; Collawn et al., 2012). Furthermore, studies in newborn pigs showed that ASL Na^+ concentration is the same in CF and non-CF (Pezzulo et al., 2012). This idea has been further supported by the observation that CF pig spontaneously develop lung disease and do not show difference in PCL depth respect to wild-type pigs. The team at the University of Iowa is more supportive of the "compositional

hypothesis", in which defective CFTR leads to an altered anion composition of the ASL. Initially, it was proposed that CFTR is involved in NaCl reabsorption. Therefore, defective CFTR in CF airway epithelia resulted in high-salt ASL thus causing impairment of salt-sensitive antimicrobial peptides activity and chronic infection (Zabner et al., 1998). However, a low NaCl concentration in the ASL of non-CF epithelia has not been confirmed by others (Jayaraman et al., 2001). The compositional hypothesis is now oriented towards an alteration of the HCO_3^- secretion in CF epithelia which hampers mucus viscoelastic properties and release by submucosal glands, consequently destroying MCC and antimicrobial activity (Hoegger et al., 2014). In conclusion, the role of ENaC in the development of CF and the possible functional interaction between ENaC and CFTR is still debated (Collawn et al., 2012).

Proteolytic regulation

It is well known that ENaC requires proteolytic cleavage on multiple sites of its extracellular loops in α and γ subunits to allow channel activity, and this may occur by three different types of proteases: intracellular convertase-type proteases (e.g., furin), extracellular cell-attached proteases (e.g., channel-activating proteases, CAPs), and soluble proteases (e.g., trypsin and elastase). Uncleaved ENaC is first attacked by furin in the Golgi and then transported already active to the plasma membrane. An additional pool of uncleaved channels can bypass furin and insert in the membrane as "silent" channels. The existence of a pool of uncleaved channels in the plasma membrane suggests that they can act as a reservoir of channels that can be rapidly activated by extracellular cell-attached proteases or soluble proteases (Figure 8) (Knight et al., 2006). In contrast, ENaC cleavage is prevented by several endogenous protease inhibitors, like serpins (Rossier & Stutts, 2009), protease nexin-1 (PN-1) (Kitamura & Tomita, 2010), elafin, secretory leukocyte protease inhibitor (SLPI), and alpha-1 antytripsin (AAT) (Twigg et al., 2015). Recently, many efforts led to the identification of compounds that act as protease inhibitors for possible therapeutic application. Among them, camostat provides a potent inhibition of ENaC function in human airway epithelia (Coote et al., 2009; Gaillard et al., 2010). Protease and protease inhibitors activity is dependent on multiple factors, including tissue specificity. For example, it seems that furin-dependent cleavage is not relevant for ENaC activation in airway epithelial cells (Rossier & Stutts, 2009). Moreover, activity of protease and protease inhibitors may be influenced by ASL microenvironment (Gaillard et al. 2010).

Another possible inhibitor of ENaC activity is the short palate lung and nasal epithelial clone 1 (SPLUNC1), a secreted protein that comprises up to 10% of the total proteins in the ASL. SPLUNC1 was found to directly bind ENaC and prevent its cleavage by proteases. It has been proposed a model in which the concentration of SPLUNC1 in the ASL would allow ENaC to be sensitive to changes in ASL volume. When ASL volume is high, SPLUNC1, as well as other protease inhibitors, is diluted and ENaC is activated by cell-attached proteases. In contrast, when ASL volumes is low, concentrated protease inhibitors prevent ENaC activation and hence airway surface dehydration. This mechanism highlights the importance of soluble molecules as volume sensing ENaC regulators (Gaillard et al., 2010; Bartoszewski et al., 2017; Rotin & Staub, 2021).

Ubiquitination and degradation

Once both the active cleaved pool and the "silent" pool of ENaC channels reach the plasma membrane through exocytosis, active channels are removed from the membrane through endocytosis (Kabra et al, 2008). Intracellular channel turnover ($t_{1/2}$ = 40-70 min) is slower respect to ENaC channels in the plasma membrane ($t_{1/2}$ = 12-17 min), suggesting that cleaved channels are rapidly removed (de la Rosa, 2002). Following endocytosis, ENaC localizes in early endosomes and could be recycled back to the cell surface or be degraded in lysosomes (Kabra et al, 2008).

Nedd4-2 (NEDD4L), an E3 ubiquitin ligase that binds C-terminal PY motif of the ENaC subunits, reduces channels surface expression by increasing its endocytosis and, once in the endosome, targets them for degradation in lysosomes. ENaC endocytosis occurs in a biphasic time course, thus reflecting two possible overlapping mechanisms: i) distinct ENaC pools with different stability are present in the membrane and endocytosed in different times; ii) some channels could be recycled back into the membrane (Kabra et al, 2008).

Another important ENaC regulator is the serum-glucocorticoid kinase 1 (SGK1). SGK1 is a master kinase regulating ion and solute transport processes through epithelia. SGK1 is activated by phosphorylation of its hydrophobic motif (HM) in the carboxy-terminal domain by mTORC2 complex (Lu et al., 2010; Gleason et al., 2015). Active SGK1 phosphorylates Nedd4-2, interfering with its binding to ENaC and consequently its ubiquitination, thus increasing the number of channels in the membrane (Debonneville et al., 2001). It has also been reported that SGK1 directly

phosphorylates ENaC α subunit, enhancing its activity (Diakov & Korbmacher, 2004). mTOR pathway has been extensively studied as integrative on many inputs (growth factors like insulin, nutrients, energy, stress such as hypoxia) (Wullschleger et al., 2006) to modulate a variety of cell processes (Debonneville et al., 2001). The involvement of mTOR complex in ENaC regulation points out to the large number of stimuli that may affect its activity (Figure 8).

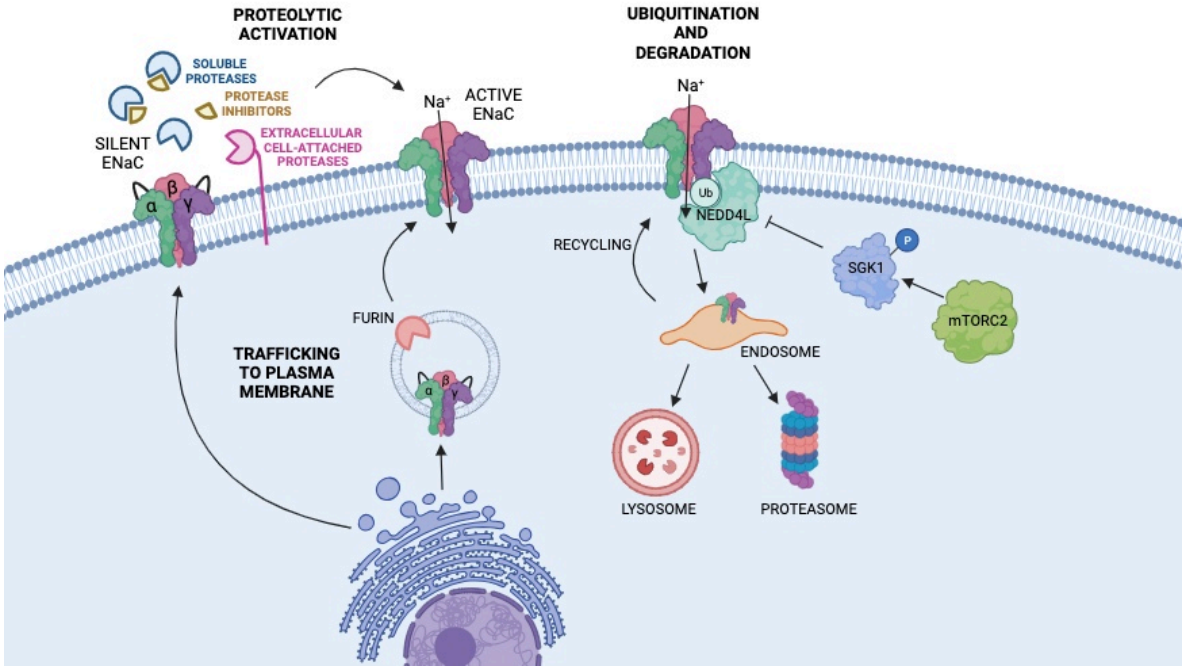

Figure 8. ENaC proteolytic activation, ubiquitination and degradation. Graphical representation of ENaC trafficking into the plasma membrane, activation by proteases and ubiquitination and degradation process controlled by SGK1. Created with Biorender.com.

Diseases associated to ENaC alterations

ENaC dysregulation is causative of different genetic pathologies. ENaC loss-of-function mutations cause severe renal salt-wasting syndrome and pseudohypoaldosteronism (PHA) and/or respiratory distress syndrome in newborns (Rossier & Stutts, 2009). Patients with PHA have airways obstruction and infection in childhood, then their lung function becomes normal. These features reflect the fact that PHA patients have an increase in ASL volume and accelerated MCC rate after exposure to β-adrenergic or purinergic agonist. Accordingly, if MCC is preserved, infections do not occur (Knowles & Boucher, 2002; Gaillard et al., 2010). In contrast to PHA, ENaC gain-of-function mutations cause Liddle's syndrome, characterized by hypertension due to excessive renal Na^+ absorption. Liddle's syndrome mutations occur in the C-terminal motif that binds Nedd4-2, interfering with ENaC ubiquitination and degradation (Knight et al., 2006; Rotin & Staub, 2021). Intriguingly, there is no evidence that patients with Liddle's syndrome have CF-like lung disease, which should be expected according to the low-volume hypothesis.

Enhanced ENaC activity can also be a consequence of other factors. Under conditions of chronic inflammation, like in CF and COPD, the increased levels of human neutrophilic elastase may indirectly activate ENaC and contribute to ASL hyper-dehydration. This highlights the therapeutic potential of ENaC inhibition to improve airway surface hydration and MCC in different genetic and non-genetic chronic respiratory disorders (Bartoszewski et al., 2017).

1.4.2 The Cystic Fibrosis Transmembrane conductance Regulator (CFTR): chloride and fluid secretion

The principal mechanisms through which epithelia regulates salt and water secretion is by Cl^- efflux across the apical membrane. Intracellular Cl^- accumulation is provided by active uptake from the basolateral membrane through the Na^+-K^+-$2Cl^-$ cotransporter NKCC1 (gene name SLC12A2), that uses the Na^+ gradient driven by the Na^+-K^+-ATPase to move Cl^-. Cl^- secretion through the apical membrane of many epithelia is dependent on CFTR activity (Saint-Criq & Gray, 2017).

CFTR is an integral membrane protein belonging to the ATP-Binding Cassette (ABC) superfamily, whereby it shares the general multi-domain structure (Moran, 2016). Despite this, CFTR is the unique member known to function as an ATP-gated ion channel (Moran, 2016; Liu et al., 2017), thus regulating Cl^- and HCO_3^- transport across apical membranes of many different epithelia (Moran, 2016). Localization of CFTR in the airway epithelium is still debated: for many years it was reported in ciliated cells (Kreda et al., 2005), but the discovery of high level of CFTR in ionocytes revised this concept (Montoro et al., 2018; Plasschaert et al., 2018). However, it has been reported that CFTR may be highly concentrated in ionocytes but also present in other cells, in particular ciliated cells. Further investigation would be needed to assess CFTR expression and function in different cell types (Scudieri et al., 2020).

CFTR protein, from the N-terminus to the C-terminus, is formed by the following domains: the first membrane-spanning domain (MSD1), the first nucleotide binding domain (NBD1), a regulatory R domain, the second membrane-spanning domain (MSD2), and the second nucleotide binding domain (NBD2) (Figure 9) (Liu et al., 2017). Each MSD includes six transmembrane helices (TM1-6 for MSD1, TM7-12 for MSD2) which form the channel walls and the pore. CFTR activation requires phosphorylation of the R domain in multiple serine and threonine sites. Phosphorylation occurs through increase of cAMP concentration that in turn activates protein kinase A (PKA). For this reason, CFTR is defined as a "cAMP-activated channel". Subsequently to the phosphorylation of the R domain, ATP binding to NBDs cause their dimerization with a conformational change that is transmitted to MSDs leading to channel opening. The hydrolysis of ATP terminates the gating cycle, closing the channel (Moran 2016).

Once the CFTR channel is fully activated, its activity lasts for long time, suggesting its central role in sustained anion secretion (Li et al., 2017).

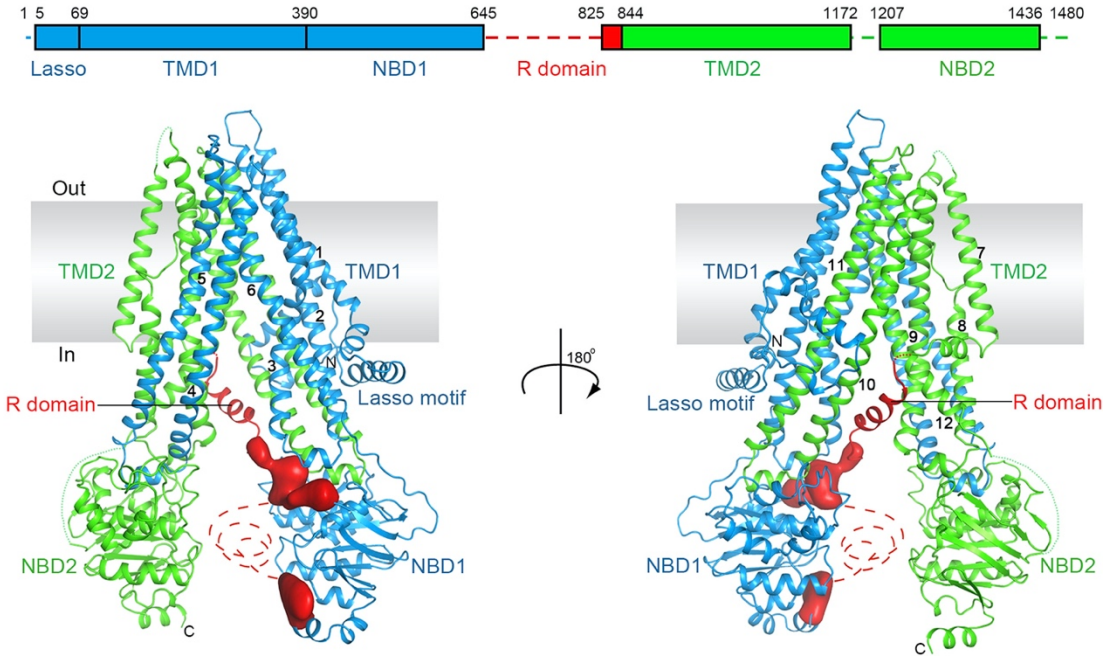

Figure 9. CFTR channel. Structure of human CFTR in the dephosphorylated, ATP-free conformation. Adapted from Liu et al., 2017.

In vivo, the increase in cAMP is triggered by various extracellular messengers, including adrenaline, prostaglandins, adenosine that, by binding the corresponding receptors, activate adenylyl cyclase. For in vitro experiments, CFTR is usually directly stimulated with adenylyl cyclase activators (forskolin) or cAMP analogues (CPT-cAMP) to bypass receptors and related regulatory mechanisms. In this way, maximal CFTR activity can be obtained. For experiments, it is also important to use selective CFTR specific inhibitors such as $CFTR_{inh}$-172 (Ma et al., 2002) which allow to evaluate CFTR contribution to total transepithelial transport.

Cystic fibrosis (CF) is an autosomal recessive genetic disorder that affects 1 newborn in 2500-4500 among the Caucasian population. It is a multi-organ disease that affects pancreas, liver, sweat glands, reproductive tracts and, particularly, the respiratory system. In 1989, mutations in CFTR gene were identified as causative of CF. Since the gene identification, more than 2000 mutation have been described. Among them, the most common one is F508del, affecting 70% of CF patients (Fanen et al., 2014; Elborn, 2016). More recently, the multi-center project CFTR2 has reexamined the listed CF mutations by testing their effect on CFTR expression and function. It appears that the number of CF-causing mutations is less than 500, with the other variants being polymorphisms.

Mutations are divided into six classes based on their effect on CFTR function (Figure 10):

- Class I: premature termination codons leading to truncated CFTR protein as well as formation of unstable truncated mRNA that is degraded by non-sense mediated decay (NMD) mechanisms (G542X, W1282X)
- Class II: formation of a misfolded protein with trafficking defect that is retained in the endoplasmic reticulum and degraded by proteases (F508del)
- Class III: formation of a protein with defective channel gating (G551D)
- Class IV: formation of a protein with decreased channel conductance (R117H)
- Class V: mutations that cause reduced synthesis of functional CFTR at mRNA or protein level or both (2789+5G->A)
- Class VI: formation of a protein with decreased stability in plasma membrane (Q1412X)

However, this classification is a simplification, since some mutations belong to more than one class, like F508del that causes CFTR misfolding (class II), channel gating defect (class III) and plasma membrane instability (class VI).

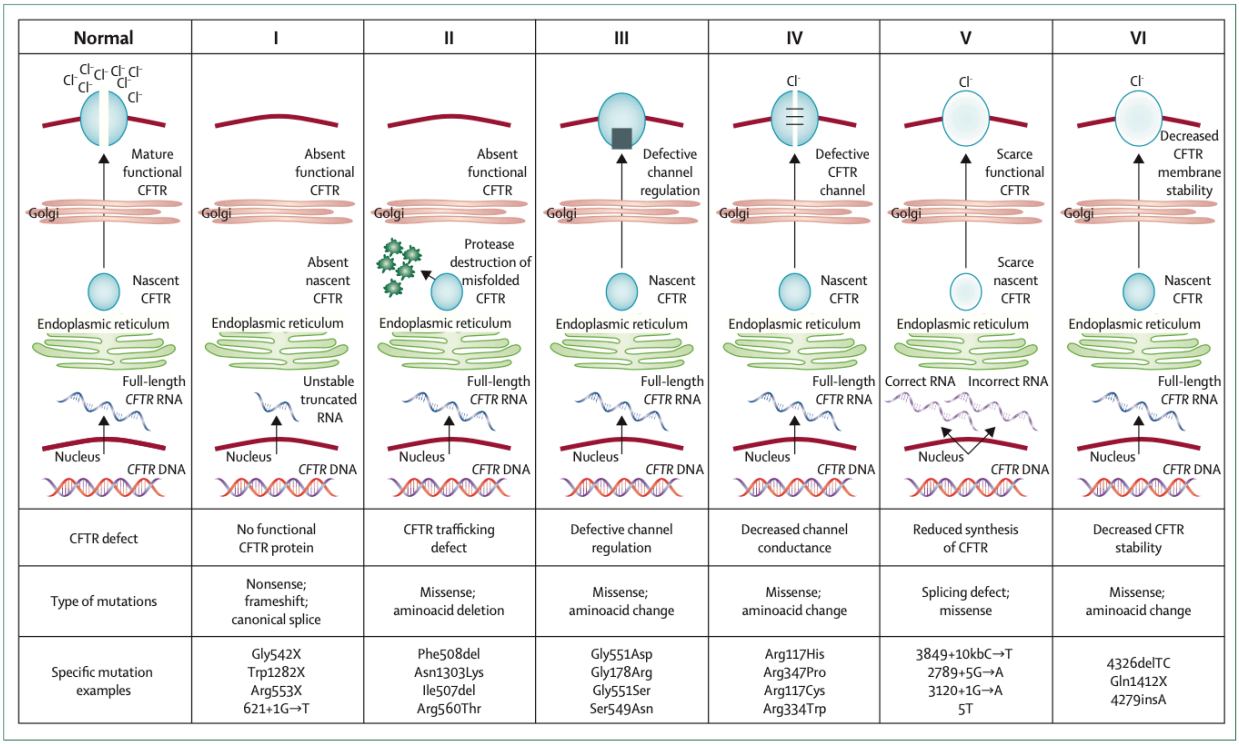

Figure 10. CFTR mutations. CFTR mutations are divided into six classes based on their implication on channel function. Adapted from Elborn et al., 2016.

For this reason, the present gold standard for the treatment of CF patients with F508del is a combinatorial therapy including correctors and potentiators (Fanen et al., 2014). The correctors are compounds that improve CFTR folding, trafficking and stability into the plasma membrane (VX-809, VX-445, and VX-661, also known as lumacaftor, elexacaftor, and tezacaftor, respectively), whereas potentiators (VX-770; ivacaftor) increase open channel probability thus overcoming the channel gating defect (Van Goor et al., 2009). Currently, patients with one or two copies of F508del are treated with the triple drug combination named Trikafta/Kaftrio, composed by VX-661 and VX-445 correctors plus the VX-770 potentiator (Keating et al., 2018). Patients with class III mutations, such as G551D, are treated with the VX-770 potentiator alone (drug name: Kalydeco). However, there are more than 10% of CF patients carrying undruggable mutations that cannot benefit from the therapy with correctors and potentiators (Fajac & Sermet-Gaudelus, 2021). For these “orphan mutations”, alternative targets should be considered.

1.4.3 Additional chloride channels: TMEM16A and SLC26A9

TMEM16A (gene name ANO1) is a Ca^{2+}-activated Cl^- channel (Caputo et al., 2008; Schroeder et al., 2008; Yang et al., 2008), belonging to the anoctamin membrane protein family. It is an homodimeric channel, in which each subunit includes ten transmembrane helices. The Ca^{2+} binding occurs in sites within the transmembrane domain, allowing a conformational rearrangement and pore opening (Figure 11) (Paulino et al., 2017; Dang et al., 2017).

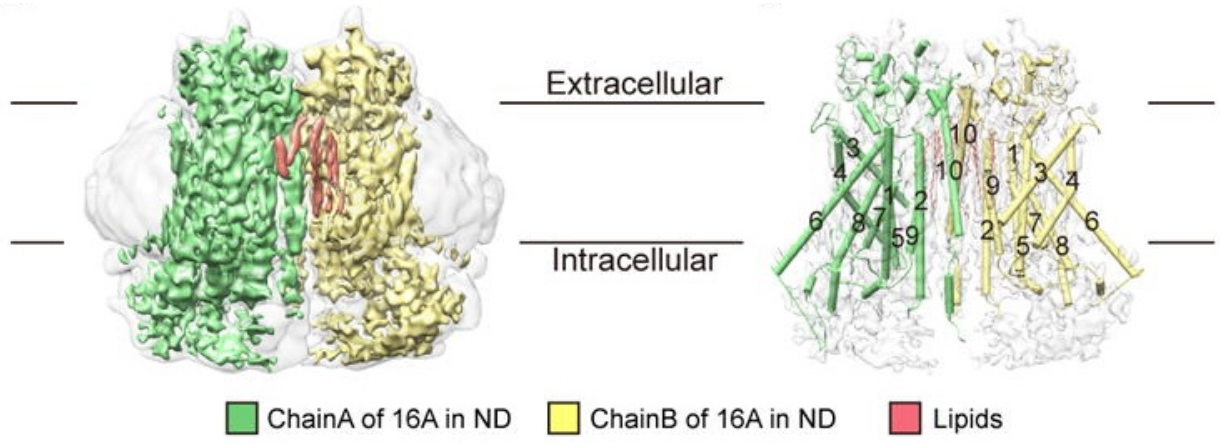

Figure 11. TMEM16A structure. Left: electron microscopy density map of TMEM16A. **Right:** TM1-10 superimposed on the electron microscopy density map. Adapted from Dang et al., 2017.

Activation of TMEM16A can be achieved through Ca^{2+}-mobilizing agents such as purinergic receptor agonists (ATP, UTP), which can be released in response to mechanical stress. In contrast to CFTR, Ca^{2+}-dependent Cl^- secretion through TMEM16A consists in a transient opening that rapidly returns to resting levels, suggesting that it functions only when increased anion secretion is required. Differently from CFTR, TMEM16A activity also depends on voltage, with activation and deactivation of the channel occurring at positive and negative membrane potentials, respectively (Pedemonte & Galietta, 2014). Long-lasting activation of TMEM16A by pharmacological agents is considered a potential therapeutic strategy to overcome defective Cl^- secretion caused by CFTR loss of function (Li et al., 2017).

By high-throughput screening of chemical libraries with a functional assay, a promising TMEM16A activator, ETX001 was found (Danahay et al., 2020). This compound improves fluid secretion and MCC in vitro and in animal models. Other compounds identified by high-throughput screening are not direct TMEM16A activators but pharmacological modulators of the Ca^{2+} signaling pathway (Genovese et al., 2022). Importantly, many compounds have been reported as inhibitors of TMEM16A channels, but almost all of them (except Ani9 compound) act indirectly on TMEM16A by altering intracellular Ca^{2+} mobilization (Genovese et al., 2023). This is an important information to consider when such compounds are used as research tools to investigate the role of TMEM16A in vitro and in vivo.

TMEM16A expression in bronchial epithelial cells is enhanced by Th2 cytokines, such as interleukin (IL)-4 (Caputo et al., 2008) and has been found in mucus-secreting cells (MUC5AC-positive), particularly under IL-4 induced mucus metaplasia (Scudieri et al., 2012). Since secretion of anions, particularly HCO_3^- is important for mucus expansion and release (Garcia et al., 2009; Hoegger et al., 2014), this may suggest a role of TMEM16A in mucus secretion and hydration under inflammatory conditions (Scudieri et al., 2012).

Another possible alternative Cl^- channel is SLC26A9. SLC26A9 works as a Cl^- channel (Salomon et al., 2016) with low permeability to HCO_3^-, although it may also function as a Cl^-/HCO_3^- exchanger and a Na^+ transporter based on cell and tissue context (Balázs & Mall, 2018). SLC26A9 belongs to the SLC26 solute-linker carrier family of anion transporter (such as SLC26A4) with which it shares common structural features, including the STAS domain, a region of SLC26 proteins that is used for interaction with other proteins, including CFTR (Walter et al., 2019). This indicates the possibility of interactions of SLC26A9 with CFTR. It has been demonstrated that SLC26A9 contributes to cAMP-stimulated Cl^- currents in human bronchial epithelial cells and co-expression with CFTR results in larger currents. Moreover, SLC26A9 activity is lowered in F508del homozygous patients and is restored using CFTR modulators. However, SLC26A9 current is not compromised by co-expression with G551D-CFTR, a mutant that normally traffics to the plasma membrane but displays gating defects. This suggests that SLC26A9 and CFTR share a common trafficking pathway to reach the plasma membrane. SLC26A9 has been identified as a modifier gene in CF, since the presence of the C allele of rs7512462 ameliorates lung function in G551D patients and improves the response to CFTR modulators (Balázs & Mall, 2018). Moreover,

studies on idiopathic diffuse bronchiectasis reported rare loss-of-function mutations in SLC26A9 (Bakouh et al., 2013). SLC26A9 is also upregulated by Th2 inflammation and contributes to mucus hypersecretion and airway mucus plugging in asthma mice models (Anagnostopoulou et al., 2012). Therefore, SLC26A9 has been proposed as an alternative therapeutic target and modifier gene in CF and in other chronic respiratory diseases (Balázs & Mall, 2018).

1.4.4 ATP12A proton-potassium pump: ASL pH regulation

ATP12A, the non-gastric form of H^+/K^+-ATPase (Crambert, 2014), is a pump belonging to the superfamily of type II P-type ATPases, which use the energy of ATP hydrolysis to transport ions across biological membranes against the electrochemical gradient. The P-type ATPases share a common highly conserved structure of the α subunit, with 10 transmembrane helices and a large intracellular loop with three domains: A (actuator), N (nucleotide-binding) and P (phosphorylation) in which the catalytic steps occur (Sweadner & Donnet, 2001). To be functional and for the correct localization in plasma membrane, the α subunit needs to be associated with a β subunit (Figure 12).

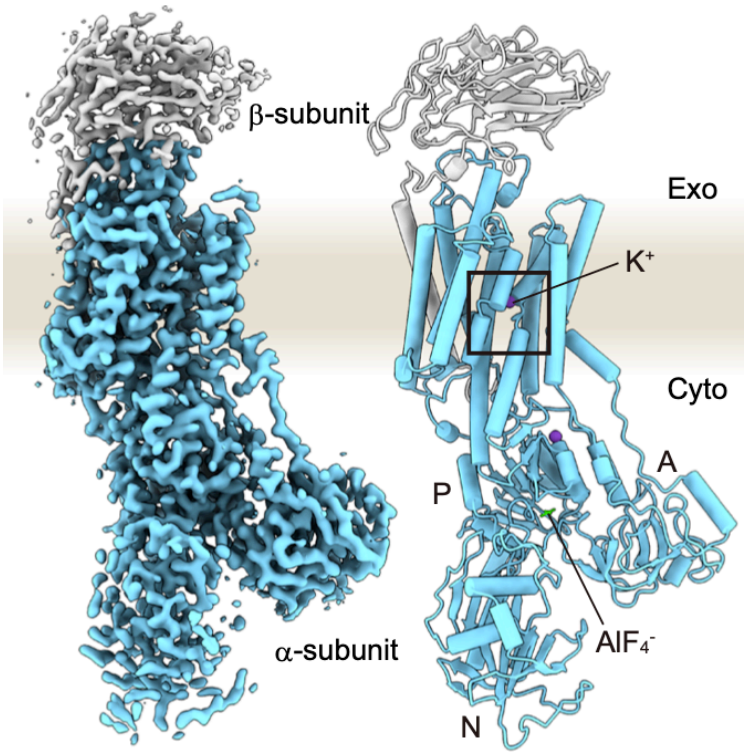

Figure 12. Structure of non-gastric H^+/K^+-ATPase (ATP12A). Electron density map and cartoon model of ATP12A. The *α* and β subunit (ATP1B1) are shown in cyan and gray, respectively. K^+ ions are shown as purple spheres. The cytoplasmic A, P and N domains are indicated. Adapted from Young et al., 2022.

In the case of ATP12A, it has been shown that its β subunit in airway epithelial cells corresponds to ATP1B1, the Na^+/K^+-ATPase β subunit (Scudieri et al., 2018). Actually, ATP12A and the Na^+/K^+-ATPase α subunits share 65% of their structure and both are inhibited by binding of cardiac glycosides like ouabain on the extracellular loop (Qiu et al., 2006; Sweadner & Donnet, 2001), although with low and high affinity, respectively (Qiu et al., 2006).

The extent of ATP12A expression in the airway epithelium is species-specific and this provide a possible explanation for the different lung disease in animal CF models and in CF patients. Newborn CF pigs spontaneously develop lung phenotype, resembling human CF disease. The lack of HCO_3^- secretion through CFTR causes acidic ASL pH that leads to impaired antimicrobial killing in pigs (Pezzulo et al., 2012). In contrast, CF mice do not develop a spontaneous CF lung phenotype (Snouwaert et al., 1992; Grubb & Boucher 1999). A possible explanation is that Ca^{2+}-activated Cl^- channels are abundant in mice, but not in humans, so mice can compensate defective Cl^- and HCO_3^- secretion due to CFTR loss of function through other Cl^- channels. However, also pigs have high levels of Ca^{2+}-activated Cl^- channels, therefore another factor should be involved. Shah and colleagues demonstrated that ATP12A is highly expressed in the airways of both human and pigs, but not in mice, and it is responsible for ASL acidification, that is extremely worsened in airways lacking CFTR-mediated HCO_3^- secretion, thus leading to impaired bacterial killing. This work pointed out the importance of ATP12A as alternative therapeutic target: its inhibition could normalize ASL and host defense abnormalities in CF (Shah et al., 2016).

ATP12A expression has been reported in MUC5AC-positive cells on the surface epithelium and in submucosal glands of human bronchi (Scudieri et al., 2018). Moreover, ATP12A is increased in CF bronchi compared with healthy controls. However, ATP12A expression does not differ between cultured CF or wild-type human bronchial epithelial cells under sterile conditions (Scudieri et al., 2018). On the other hand, treatment of bronchial epithelial cells with bacterial supernatant and IL-4/IL-13 strongly increases ATP12A expression. Therefore, the upregulation of ATP12A in CF airways in vivo appears to be due to infection/inflammation rather than to a direct link to CFTR defect (Gorrieri et al., 2016; Scudieri et al., 2018; Lennox et al., 2018). ATP12A also seems involved in regulating ASL viscosity caused by IL-13, thus suggesting that inhibition of ATP12A may mitigate mucus dysfunction in Th2 inflammatory conditions (Lennox et al., 2018).

Despite its canonical localization in mucus-producing cells, ATP12A may also localize in ciliated cells and this feature has been reported as an early sign of trans-differentiation from ciliated to goblet cells in response to inflammatory stimuli (Vieira-Braga et al., 2019). Taken together, these results indicate an involvement of ATP12A in airway inflammation.

Although ATP12A is the principal protein responsible for H^+ secretion, its expression is different throughout the airways, being more expressed in large airways. This suggests that another mechanism is involved in mediating H^+ secretion in small airways. V-ATPase seems to be expressed in small airways, where it contributes to ASL pH and viscosity (Li et al., 2021). V-ATPases are ubiquitously expressed and are multi-subunit pumps formed by two domains: the V0 domain represents the transmembrane part whereas the V1 domain is cytosolic. The V1 domain hydrolyzes the ATP necessary for the rotation of the pump and the V0 domain is responsible for H^+ translocation. The role of the V-ATPases has been extensively characterized as fundamental for the acidification of intracellular organelles and vesicles such as vacuoles, endosomes, lysosomes and in regulation of extracellular pH in epithelia and osteoclasts. V-ATPase localization and function are regulated by differential expression of its subunits (Breton & Brown, 2007). Some evidence regarding the involvement of ATP6V0D2 isoform in plasma membrane localization has been reported (Li et al., 2021). Intriguingly, V-ATPase subunits, including ATP6V0D2, are specifically expressed in ionocytes (Montoro et al., 2018), pointing out to a possible common regulation with CFTR, as already reported in enterocytes (Collaco et al., 2013). However, given the complexity of V-ATPase structure, isoforms, function and regulation, further studies will be needed to characterize its role in the airways and its possible interaction with CFTR.

1.4.5 Pendrin (SLC26A4): chloride-bicarbonate exchange

SLC26A4, also known as Pendrin, belongs to the solute carrier SLC26 family, a relatively new family of transporters with many structural and functional diversities that are still not completely understood. Members of the family can be divided into three groups: the SO_4^{2-} transporters, the Cl^-/HCO_3^- exchangers, and the ion channels (Ohana et al., 2009). SLC26A4 is classified as an electroneutral Cl^-/HCO_3^- exchanger, although it can transport other different substrates including iodide (I^-) and thiocyanate (SCN^-) (Pedemonte et al., 2007; Ohana et al., 2009).

Recently, the structure of pendrin has been determined by cryo-EM (Liu et al., 2023). It is formed by a domain-swapped homodimer, in which each protomer has an N-terminal domain (NTD), a transmembrane domain (TMD), a sulfate transporter and anti-sigma factor antagonist domain (STAS) and a C-terminal domain (CTD). The STAS intracellular domains is responsible for the interaction between the protomers to form a dimeric knob in the cytoplasmic side. On the other side, the 14 helices of TMD are divided into two parts, forming the core and the gate regions. An anion-binding site for Cl^- is observed between the core and the gate region within the TMD. HCO_3^- binding occurs in the same pocket as Cl^-. When exposed to a mixture of Cl^- and HCO_3^-, three distinct states of pendrin are shown: 15% are in inward-open state, 15% are in outward-open state and about 70% form an asymmetric homodimer, with one inward-open and one outward-open protomer. The authors hypothesize that, in the presence of Cl^-, the inward-open conformation is the favorite state. When HCO_3^- is added, it replaces Cl^- from the binding site in protomer B, causing the rotation of the core region against the gate region, in a movement like an elevator. This conformational change end with the outward-open state, in which HCO_3^- diffuses out and Cl^- binds to reverse the exchange process. The coincidence of secretion and uptake points out to an inverted alternate-access mechanism through which the electroneutral exchange by pendrin occurs (Figure 13) (Liu et al., 2023).

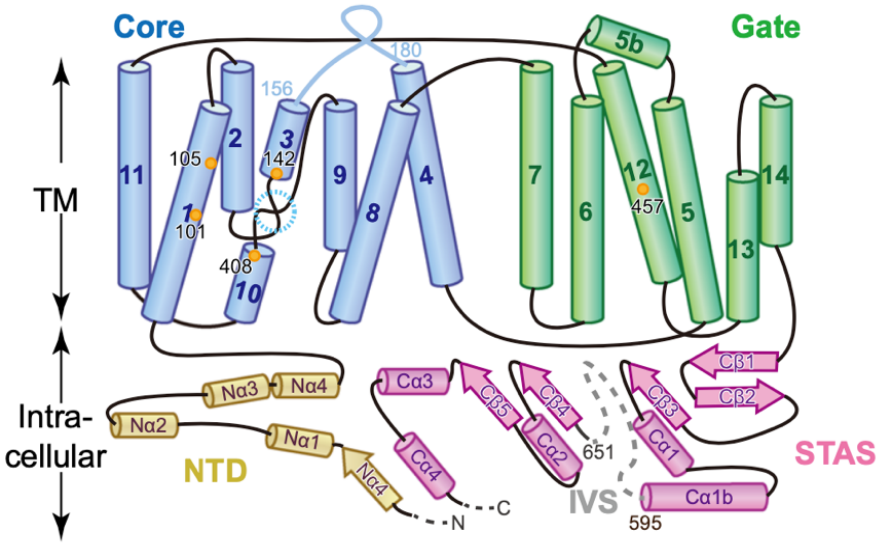

Figure 13. Structure of SLC26A4 (Pendrin). Schematic topology of pendrin: the NTD, core region, gate region and STAS domain are indicated in yellow, blue, green and pink, respectively. The anion binding pocket is shown as a dashed circle in cyan. Adapted from Liu et al., 2023.

SLC26A4 was originally found as the gene causative of Pendred syndrome, a disease characterized by congenital deafness and thyroid goiter (Everett et al., 1997). The deafness is due to altered acid-base balance of endolymphatic fluid in the inner ear. Instead, the thyroid disfunction is due to impaired I^-/HCO_3^- and Cl^-/I^- exchange and loss of I^- secretion in the thyroid follicular space (Ohana et al., 2009). Besides thyroid and inner ear, SLC26A4 expression has also been found in the kidney, in which it is involved in renal Cl^- absorption and HCO_3^- secretion, and in the airway epithelium (Pedemonte et al., 2007).

In the airway epithelium, HCO_3^- is possibly needed to alkalinize ASL, since acidic pH impairs ciliary beating and bacterial killing. HCO_3^- is also required for mucus homeostasis (Garnett et al., 2011), and Cl^- and HCO_3^- exchange may regulate thickness and hydration properties of the ASL. For many years, it was believed that HCO_3^- secretion was operated by CFTR alone. The discovery of the SLC26 transporters led to a revision of this concept (Ko et al., 2004; Shcheynikov et al., 2006). Pendrin-mediated Cl^-/HCO_3^- exchange activity in combination with CFTR-mediated HCO_3^- secretion has been described in Calu-3 cells (Garnett et al., 2011), although some authors found that the contribution of pendrin to HCO_3^- secretion in Calu-3 cells is negligible (Kim et al., 2018). Pendrin function in the airways is still controversial (Nozfiger et al., 2011; Adams et al., 2014), also taking into consideration that Pendred patients do not develop respiratory disease (Pedemonte et al., 2007). This indicate that the absence of pendrin may be protective against some pulmonary diseases (Adams et al., 2014).

Since Cl^- and HCO_3^- transport requires a common regulation, it has been proposed that CFTR operates in parallel with pendrin, forming a Cl^- and HCO_3^- transporting complex. Cl^- secretion through CFTR is predicted to support apical Cl^-/HCO_3^- exchange by maintaining a Cl^- gradient for efficient anion exchange (Garnett et al., 2011). Actually, some studies report that CFTR and SLC26 transporters bind through interaction between the R domain on CFTR and the STAS domain of SLC26 proteins. This interaction is markedly enhanced when the R domain is phosphorylated by PKA, and results in mutual activation of both transporters (Ko et al., 2004; Shcheynikov et al., 2006). However, the physical interaction may obviously only occur if CFTR and pendrin are expressed within the same cell. Kim and colleagues showed colocalization of CFTR and pendrin in ciliated cells but did not exclude the possibility of pendrin expression in goblet cells (Kim et al., 2018). Instead, Adams et al., reported pendrin expression in non-ciliated mucus producing cells, particularly in IL17-A treated cells (Adams et al., 2014).

In nasal and bronchial epithelial cells, it has been reported that pendrin slightly contributes to Cl^-/HCO_3^- exchange under resting condition (Kim et al., 2018). Instead, its role becomes predominant following exposure to Th2-type cytokines IL-4/IL-13 (Nozfiger et al., 2011) and IL-17A (Adams et al., 2014), thus linking pendrin to the pathogenesis of respiratory diseases such as bronchial asthma and COPD. In IL-4 and IL-17A treated bronchial epithelial cells, pendrin contributes to both pH and HCO_3^- transport, and its activity is enhanced by forskolin stimulation of CFTR activity (Adams et al., 2014; Kim et al., 2018). In contrast, Haggie and coll. (Haggie et al., 2016) reported

that pendrin is not a key determinant in regulating ASL pH but is instead a contributor to ASL dehydration under inflammatory conditions. Accordingly, treatment of epithelia in vitro with a pharmacological pendrin inhibitor increases ASL hydration (Haggie et al., 2016). Another possible role of SLC26A4 is in anti-microbial activity. Indeed, SLC26A4 mediates SCN^- transport into the ASL, where it is oxidized to hypothiocyanite ($OSCN^-$) in the presence of hydrogen peroxide produced by DUOX1/2 and lactoperoxidase (Pedemonte et al., 2007; Nozfiger et al., 2011). $OSCN^-$ is an innate antimicrobial molecule, it also activates NF-κB and boosts the production of pro-inflammatory cytokines. Pendrin inhibition suppress pro-inflammatory response and prevent LPS-induced acute lung injury in mice (Lee et al., 2020). Since hyper-reactivity and inflammation induces lung damage in asthma, allergies and COPD, pendrin inhibition may represent a potential therapeutic intervention to hydrate ASL and reduce excessive inflammation (Lee et al., 2020).

1.5 Development of differentiated airway primary cultures as an in vitro model for human respiratory diseases

In the past decades, the airway epithelium was studied on ex vivo samples taken from individuals with lung diseases or from control individuals. However, this approach was seriously limited by the poor availability of biological samples. Many animal models have also been employed, but they do not always resemble the features of human respiratory diseases due to species-specific differences. A clear example is the generation of CF mouse models, that resemble the intestinal phenotype of CF patients, but dot not spontaneously develop a lung disease (Snouwaert et al., 1992; Grubb & Boucher 1999; Collawn et al., 2012). In the last years, primary human bronchial and nasal epithelial cells, obtained from explanted lungs, biopsies and nasal brushings, have been used as an efficient in vitro model for respiratory diseases. The first step consists in the isolation of basal stem cells, that can be expanded in a proliferative medium on plastic dishes for various passages. One of the limitations is the reduced proliferation capacity of stem cells, that undergo cellular senescence. This has been overcome using Rho kinase (ROCK) and BMP/TGFβ inhibitors of SMAD pathway (Mou et al., 2016), which enable the primary cells to proliferate avoiding a squamous cell phenotype and without losing their differentiation capacity (Fulcher et al., 2005). When these cells are then shifted to a condition enabling cellular polarization (seeding on a porous membrane), a dramatic phenotypic change occurs with the development of a polarized epithelium (Fulcher et al., 2005). To allow polarization, the cells are also kept under air liquid interface (ALI) condition, which means that the medium from the apical side is removed so the cells are exposed to air, and the nutrients only come from the basolateral medium (Fulcher et al., 2005). The ALI culture now represents a gold standard for the development of more physiologically relevant airway epithelia that: i) differentiate into a pseudostratified epithelium; ii) are formed by multiple cell types (ciliated cells, goblet cells, basal cells); iii) develop tight junction and a relatively high transepithelial electrical resistance; iv) generate distinct apical and basolateral membranes with significant transepithelial ion transport; v) show mucociliary transport. Currently, patient-derived nasal and bronchial epithelial cells represent the most relevant in vitro model that perfectly mimics the in vivo airways (Fulcher et al., 2005). For more details on bronchial epithelial cells culture preparation, see Material and Methods 2.2.

1.6 Airways defense mechanisms and inflammation

1.6.1 Innate immune response

Epithelia in the body represent a barrier between the internal and the external environment. In particular, the respiratory epithelium represents the first point of contact for molecules, particles, bacteria, and viruses delivered with inhaled air. For this reason, airway epithelial cells represent not only a passive barrier, but also actively contribute to the innate defense system, thus providing an initial protection against inhaled pathogens (Bals & Hiemstra, 2004; Bartoszewski et al., 2017) during the early stage of infection (Hemmi & Akira, 2005). The epithelium contributes to host defense in different ways (Bals & Hiemstra, 2004). In particular, MCC is considered a primary innate defense mechanism (Mall, 2008; Knowles & Boucher, 2002).

Furthermore, the airway epithelium can sense bacterial components called pathogen-associated molecular patterns (PAMPs), conserved regions of pathogens that can be recognized by pattern-recognition receptors (PRRs) (Bals & Hiemstra, 2004), like Toll-like receptors (TLRs), protease activated receptors (PARs), and chemoreceptors mainly expressed by Tuft cells (Lambrecht et al., 2019). TLRs are expressed in airway epithelial cells (Bals & Hiemstra, 2004) and in dendritic cells (DCs) resident in the lung (Hemmi & Akira, 2005; Sertl et al., 1986). Each TLR responds to different bacterial, fungal and viral components. For example, TLR4 is responsible for lipopolysaccharide (LPS) recognition, whereas TLR3 senses the presence of double-stranded RNA during viral infection (Bals & Hiemstra, 2004). Activation of epithelial TLRs stimulates local innate immune responses. In this way, epithelial cells activate the expression, production and secretion of antimicrobial peptides, such as lactoferrin, lysozyme, and defensins (Bals & Hiemstra, 2004), and of cytokines/chemokines that further orchestrate anti-bacterial activity by recruiting/activating cells of the innate immune system present in the airways, including innate lymphoid cells (ILCs), basophils, eosinophils, mast cells and macrophages (Lambrecht et al., 2019). Innate immune cells produce many effector cytokines and mediators that sustain inflammation (Lambrecht et al., 2019), contribute to hamper bacterial growth during short-time infections (Knowles & Boucher, 2002), to induce wound healing and angiogenesis in response to injury and to orchestrate the initiation of an adaptive immune response (Bals & Hiemstra, 2004).

Most antimicrobials produced by airway epithelial cells are salt-sensitive (Knowles & Boucher, 2002; Bals & Hiemstra, 2004) and/or pH-sensitive (Pezzulo et al., 2012). Therefore, the homeostasis of the ASL is fundamental for the initial host protection. Pezzulo and colleagues (Pezzulo et al., 2012) demonstrated that the ASL of newborn wild-type pigs rapidly kills bacteria in only 30 second of application, whereas bacterial killing is reduced in CF newborn pigs. Such results indicate that impaired bacterial killing is not due to dysfunctional MCC or to abnormal inflammation, that are common features of advanced lung disease, but that defective killing is caused by an intrinsic alteration of ASL composition (probably acidic pH), already present at birth, that impairs antimicrobial molecules. These results reflect the importance of ASL properties on bacterial killing in order to reduce the number of viable microorganisms that undergo fast replication, thus preventing lung colonization.

1.6.2 Adaptive immune response

Activation of TLR on antigen-presenting cells (APCs) initiates the adaptive immune response. In particular, DCs are a specialized type of APCs (Kaiko et al., 2008), although ILCs also may act as APCs (Lambrecht et al., 2019). ILCs are innate tissue-resident lymphocytes residing below the mucosal surface. They are involved in the response to epithelial-derived signals in the early phase of response to pathogens (Hagner et al., 2021). DCs are resident in peripheral tissues susceptible to infections and are able to process pathogens peptides and expose them on the surface on major histocompatibility complex (MHC) molecules. The activated DCs migrates into the lymphoid organs and activate naïve T lymphocyte (Th0). The epithelium itself release cytokines that boost the activity of DCs (Lambrecht et al., 2019), which in turn release costimulatory molecules and polarizing signals (predominantly cytokines) that bind Th0-cell receptors activating the JAK-STAT signaling pathway.

The different stimuli selectively promote the lineage of different activated T cells, with peculiar and tuned immune function. The T lymphocytes can be divided into three main classes with different phenotype and cytokines production: T helper type-1 (Th1), T helper type-2 (Th2), T helper type-17 (Th17). Th1 cells development is prevalently dependent on IL-12 and type 1 interferons (IFNs). These cells produce interferon-γ (IFNγ) and tumor necrosis factor-β (TNFβ)

and have a main role in protection against intracellular pathogens like viruses, some bacteria, and other types of microorganisms. The stabilization of Th2 cells requires IL-4, IL-6, IL-10 and IL-11. Activated Th2 cells release IL-4, IL-5, IL-10 and IL-13 to target extracellular parasites. Th2 pathway is particularly involved in asthma. Recently, the third class of immune response, Th17, has emerged. Th17 differentiation is dependent on IL-23 and TGF-β. Th17 cells secrete IL-17A, IL17F, IL-6, IL-22 and tumor necrosis factor-α (TNF-α) which act on epithelial cells to induce tissue inflammation and neutrophil activation. This response plays a fundamental role against extracellular bacteria (Bals & Hiemstra, 2004; Kaiko et al., 2008).

In the last years, CF has been defined as a Th17-related disease, since IL-17A has been found elevated in the sputum and in the lung of patients with CF and correlated with bacterial infection, neutrophilic infiltration, lung damage and lung function decline (Decraene et al., 2010; Hagner et al., 2021). IL-17A is mainly produced by $CD3^+CD4^+$ Th lymphocytes, but other innate and adaptive immune cells may also be a source of IL-17A, including $CD3^+CD8^+$ T cells, γδ T-cells and invariant natural killer T (iNKT) cells. Moreover, a small population of ILCs has also been found to contribute to IL-17A production. Intriguingly, CFTR -/- mice, which do not develop CF-like airway disease, show low levels of IL-17A. Instead, mice overexpressing β-ENaC show IL-17A-mediated airway inflammation, thus supporting the idea that is not the CFTR deficiency per se to trigger IL-17A production, but the mucociliary disfunction and ensuing infection/inflammation. The same authors found a reduction of lung damage in IL-17A -/- mice. This observation paves the way to study new anti-inflammatory therapeutic interventions targeting Th17 immune response in CF patients (Hagner et al., 2021).

1.6.3 Remodeling of airway epithelium in response to inflammatory stimuli

The airway epithelium itself is able to reshape its properties in response to chemokines and cytokines to boost its defense function. The first examples of epithelial remodeling derive from studies on Th2 cytokines, in particular IL-4 and IL-13, that are involved in allergic pulmonary inflammation and airway hyperreactivity in asthma. Both IL-4 and IL-13 bind to the IL-4Rα receptor, sharing signaling cascade and biological activities (Galietta et al., 2002). These cytokines induce changes in the overall architecture of the epithelium, resulting in a hypersecretory

phenotype (Galietta et al., 2002; Danahay et al., 2002; Kim et al., 2009; Lachowicz-Scroggins et al., 2010). In general, ciliation is strongly reduced (Lachowicz-Scroggins et al., 2010) and goblet cell metaplasia and mucus hypersecretion are induced, particularly that of MUC5AC mucin (Kim et al., 2009; Scudieri et al., 2012). The hypersecretory phenotype is achieved by changes in epithelial ion transport: amiloride-sensitive current is markedly decreased by Th2 cytokines, through reduction of ENaC activity. Interestingly, IL-4 has been shown to downregulate expression of ENaC γ and β subunit, whereas α subunit is not affected (Galietta et al., 2002). Moreover, bronchial epithelial cells stimulated with IL-4 show a large upregulation of NKCC1 in the basolateral membrane, with consequent increase in the Cl^- uptake (Gorrieri et al., 2016), paralleled with upregulation of anion channels/transporters in the apical membrane: SLC26A4 (Pedemonte et al., 2007), CFTR (Galietta et al., 2002) and TMEM16A (Caputo et al., 2008; Gorrieri et al., 2016).

In summary, these cytokines promote the activity of Cl^- and HCO_3^- channels/transporters and reduce Na^+ absorption through ENaC, causing a general increase in ASL hydration and a net HCO_3^- secretion, which may in turn favor mucus expansion and release (Garcia et al., 2009; Gustafsson et al., 2012) and also improve MCC and airway clearance (Hoegger et al., 2014) in order to clear particulate and secreted mucus out of the airways (Danahay et al., 2002; Galietta et al., 2002; Gorrieri et al., 2016). Moreover, HCO_3^- secretion alkalinizes pH, supporting antimicrobial activity (Pezzulo et al., 2012), and both IL-4/IL-13 alkalinize ASL pH (Scudieri et al. 2018, Lennox et al., 2018). Similar evidence of increased mucus production, ASL hydration and alkalinization has been reported for other pro-inflammatory cytokines such as IL-1β (Gray et al., 2004).

IL-4/IL-13 also increase ATP12A expression (Gorrieri et al., 2016; Scudieri et al., 2018; Lennox et al., 2018). Since H^+ secretion trough ATP12A causes ASL acidification with consequent impairment of bacterial killing (Pezzulo et al., 2012; Shah et al., 2016), its upregulation seems to be in contrast with high HCO_3^- secretion rate in IL-4 condition (Gorrieri et al., 2016). Moreover, enhanced ATP12A expression in IL-13 treated bronchial epithelial cells has been associated with increased ASL viscosity, suggesting that altered pH might influence ASL properties (Lennox et al., 2018). In the end, the role of ATP12A in inflammatory condition needs to be further investigated.

Some studies have started to evaluate the remodeling of epithelial properties by Th17 inflammatory cytokines, particularly the combination of IL-17A with TNF-α. Recent observations pointed out that ASL pH is abnormally acidic in CF neonates (Abou Alaiwa et al., 2014) and newborn CF pigs (Pezzulo et al., 2012) compared to non-CF individuals, but then it normalizes few months after birth (Schultz et al., 2017). It has been hypothesized that Th17 inflammation increases ASL pH over time, enhancing HCO_3^- secretion (Rehman et al., 2021), as already reported for Th2 inflammatory stimuli (Gorrieri et al., 2016). At least two research groups demonstrated that IL-17+TNF-α combination alkalinizes ASL pH by increasing pendrin expression and consequently HCO_3^- secretion (Adams et al., 2017; Rehman et al., 2020; Rehman et al., 2021). Upon stimulation with cytokines, alkalinization is driven also by enhanced CFTR activity (Rehman et al., 2020) and an increase in pH is also achieved in CF patients (F508del homozygous) treated with the triple modulator (Trikafta) combination (Rehman et al., 2021). This finding suggests that, despite excessive inflammation may lead to lung damage (Higgins et al., 2015), suppressing inflammation may impact on modulators efficacy (Rehman et al., 2021).

1.7 Aim of the thesis

Despite many efforts have been done in the last years by different research groups, it is still not clear to what extent the functional abnormalities occurring in the lungs of CF patients are a direct consequence of CFTR loss of function or the result of subsequent infection and inflammation. The recent findings of Th17 immune response in CF patients highlights the need to explore how the respiratory system responds to these stimuli and how the general epithelial homeostasis is modified by pro-inflammatory cytokines. The initial aim of my thesis was to particularly focus the attention on ATP12A H^+/K^+ pump and investigate its link with airway inflammation. By testing different proinflammatory stimuli, we discovered that the treatment of bronchial epithelia in vitro with IL-17A (IL-17) and TNF-α triggers a complex program that, besides upregulating ATP12A, alters the expression and function of multiple channels and transporters. Therefore, our starting aim was followed by new ideas to deeply analyze the effect of ATP12A, SLC26A4, ENaC and CFTR enhanced activity and their impact on the chemical and physical properties of airway surface. Finally, our conclusion is that these changes seem to have a physiologically relevant role in the innate defense mechanisms and barrier functions of the airway epithelium, probably boosting its response to bacterial infection.

2. MATERIALS AND METHODS

The present materials and methods are included in Guidone et al., 2022.

2.1 Analysis of nasal epithelial cells

The collection of nasal epithelial cells by brushing was previously described (Scudieri et al., 2020). For nasal epithelial cell collection, the Endobrush® (Biogyn, Mirandola, Italy) cytological sampling brush was used to collect the cells from the nasal turbinate. The brush was immediately placed in a 15 mL tube containing 10% neutral buffered formalin (05-01005Q; Bio-Optica, Milan, Italy) and shipped to the laboratory, where cells were detached from the brush, centrifuged and deposited on silanized glass slides. After attachment (2–3 hours) in a humidified chamber, cells were treated for antigen retrieval with 10 mM citrate buffer and then permeabilized with 0.3% Triton X-100 in PBS for 5 minutes, blocked with 1% bovine serum albumin (BSA) in phosphate-buffered saline (PBS) (2 hours), and incubated overnight at 4 °C with primary antibodies diluted in PBS containing 1% BSA (A7030, Sigma-Aldrich). Primary antibodies and dilutions were rabbit anti-ATP12A (HPA039526, Sigma-Aldrich), 1:400; mouse IgG1 anti-MUC5AC (MA5-12178; Thermo Fisher Scientific), 1:200; and mouse IgG2B anti-acetylated tubulin (MilliporeSigma), 1:300. Samples were washed 3 times in PBS and incubated for 1 hour in the dark with the following secondary antibodies diluted 1:200 in PBS containing 1% BSA: goat anti–rabbit Alexa Fluor 488 (catalog A11008), goat anti–mouse IgG1 Alexa Fluor 546 (catalog A2112), and goat anti–mouse IgG2B Alexa Fluor 633 (catalog A21146) antibodies (all from Thermo Fisher Scientific). After 3 further washes in PBS, slides were mounted using Fluoroshield with DAPI (MilliporeSigma) to stain cell nuclei. Immunofluorescence images were acquired with a laser scanning confocal microscope (TCS SPE; Leica Microsystems). For each sample, 200–500 cells were analyzed (Figure 14).

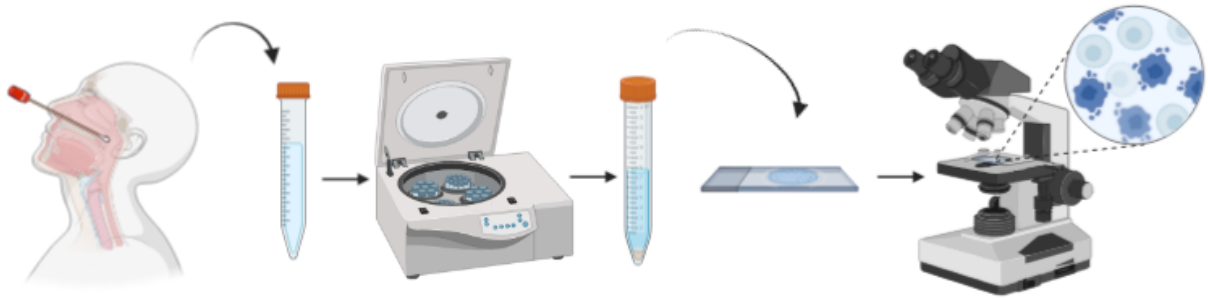

Figure 14: Experimental workflow for analysis of freshly collected nasal epithelial cells. The nasal cells collected by cytological brush were freshly fixed and shipped to the laboratory, where were processed for immunofluorescence. Created with Biorender.com.

To quantify ATP12A expression in the apical membrane (AM) of cells, two regions of interest (ROIs) were selected: one on the AM and another placed halfway between the AM and the nucleus - i.e., the cytosol (C). ROI positioning was done in merged fluorescence and brightfield images to easily detect the AM in cells with low ATP12A expression. The mean fluorescence intensity of each ROI was calculated with the ImageJ software (NIH), and only cells with AM/C ratio higher than two were considered positive for ATP12A.

2.2 Bronchial epithelial cell culture: expansion and differentiation

Human bronchial epithelial cells from CF patients (homozygous for F508del mutation) and non-CF individuals were provided by "Servizio Colture Primarie" of Italian Cystic Fibrosis Research Foundation (FFC). A detailed description of methods for the isolation and expansion of basal airway stem cells ($p63^+$/ $KRT5^+$) with a serum-free medium has been previously reported (Scudieri et al., 2012; Scudieri et al., 2020). To further promote cell proliferation, the medium was supplemented with bone morphogenetic protein (BMP) antagonist (DMH-1, 1 µM), TGF-β antagonist (A 83-01, 1 µM), and the rho-associated protein kinase 1 (ROCK1) inhibitor (Y-27632, 10 µM) (Mou et al., 2016). After 5–6 passages, cells were seeded at high density on Snapwell (cc3801, Corning Costar) or Transwell (cc3470, Corning Costar) porous inserts. After 24 hours from seeding, the proliferative medium on the basolateral side was switched to differentiation medium PneumaCult ALI (Stemcell Technologies), whereas the medium on the apical side was removed to obtain the ALI condition. Epithelia were kept in culture for at least 2–3 weeks to

achieve full mucociliary differentiation (Figure 15). When needed, cells were treated basolaterally for 72 h with IL-17A (20 ng/mL, SRP3080, Sigma-Aldrich) plus/minus TNF-α (10 ng/mL, T6674, Sigma-Aldrich), IL-4 (10 ng/mL, 14269, Sigma-Aldrich), IFN-α (10 ng/mL, H6041, Sigma-Aldrich), IFN-γ (10 ng/mL, I3265, Sigma-Aldrich), IL-1β (10 ng/mL H6291, Sigma-Aldrich), or IL-6 (10 ng/mL, I1395, Sigma-Aldrich).

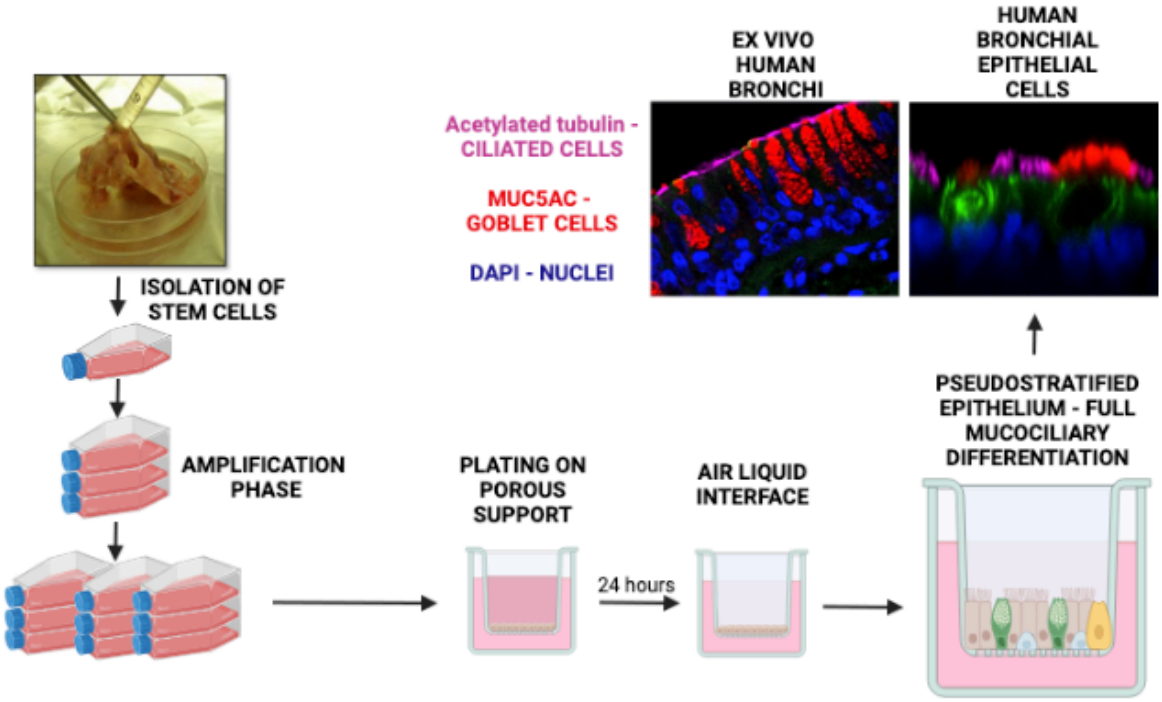

Figure 15: Expansion and differentiation steps for bronchial epithelial cells. Stem cells were collected by explanted lungs and expanded in a proliferative medium containing SMAD and Rho kinase inhibitors. The cells were then plated on porous support and after 24 hours the apical medium was completely removed, starting the differentiation process under ALI configuration. After 14-21 days, full mucociliary differentiation was achieved. Created with Biorender.com.

2.3 Immunofluorescence of cultured epithelia

Snapwell supports carrying differentiated bronchial epithelial cells were fixed in 10% neutral buffered formalin and then washed in PBS 3 times. After antigen retrieval with 10 mM citrate buffer, the samples were permeabilized with 0.3% Triton X-100 in PBS for 5 minutes, blocked with 1% BSA in PBS for 2 hours, and then incubated overnight at 4 °C with primary antibodies diluted in PBS containing 1% BSA. The following antibodies and dilutions were used: rabbit anti-ATP12A (HPA039526, Sigma-Aldrich), 1:400; mouse IgG1 anti-MUC5AC (MA5-12178, Thermo Fisher Scientific), 1:200; mouse IgG2B anti–acetylated tubulin (T7451, Sigma-Aldrich), 1:300; anti-SCNN1A (HPA012743, Sigma-Aldrich), 1:200. After 3 washes with PBS, cells were incubated with appropriate combinations of secondary fluorescent antibodies. After 3 further washes in PBS, slides were mounted using Fluoroshield with DAPI to stain cell nuclei. Images were acquired using a laser scanning confocal microscope (TCS SPE; Leica Microsystems) (Figure 16).

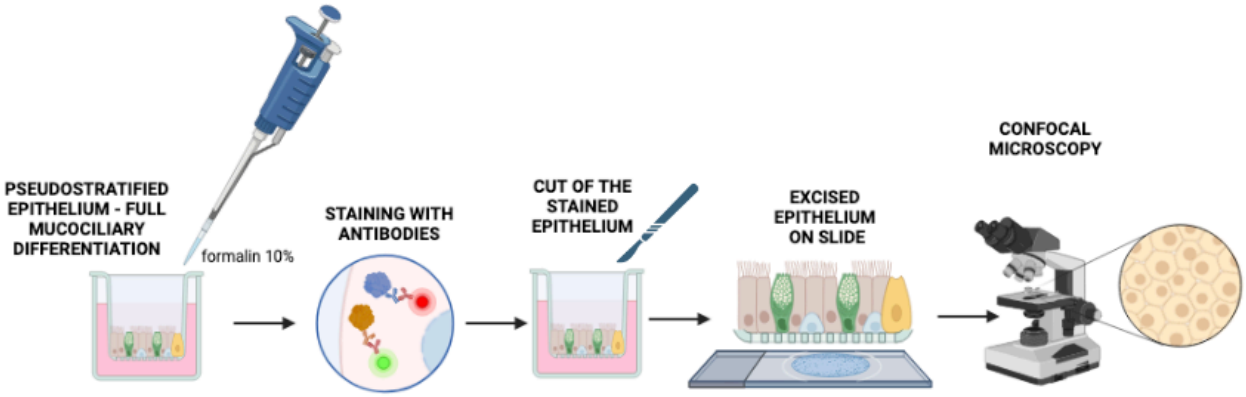

Figure 16: Experimental workflow for immunofluorescence of cultured bronchial epithelial cells. The bronchial epithelial cells grown on porous supports were fixed in formalin once achieved full differentiation. They were stained with appropriate primary and secondary antibodies, then the porous membrane was excised and mounted on slide for confocal microscopy imaging. Created with Biorender.com.

2.4 Western blot

Differentiated epithelia on Snapwell inserts were lysed in RAS buffer containing Complete Protease Inhibitor Cocktail (Roche). Cell lysates were centrifuged at 14,500 g at 4 °C for 15 minutes. Supernatant protein concentration was calculated using the Bio-Rad DC Protein Assay. In total, 20 µg of lysates were resolved in gradient (4%–15%) Criterion TGX precast gels (Bio-Rad) and transferred to nitrocellulose membranes with a Trans-Blot Turbo system (Bio-Rad). After 2 hours of blocking in 5% milk in TBS-Tween 0.5%, membranes were incubated overnight with primary antibodies in 5% milk in TBS-Tween 0.5%: anti-ATP12A (1:4000, HPA039526, Sigma-Aldrich) or anti-GAPDH (1:5000, MAB374, MilliporeSigma). After 3 washes in TBS-Tween 0.5%, secondary antibodies were incubated for 1 hour at room temperature in the dark: polyclonal anti–rabbit (catalog P0448) and anti–mouse (catalog P0447) HR-conjugated secondary antibodies (Dako, Agilent). After 3 further washes, the signals were subsequently visualized by chemiluminescence using the SuperSignal West Femto Substrate (Thermo Fisher Scientific). Signals were acquired with the Molecular Imager UVITEC Cambridge System. ATP12A and GAPDH band intensities were analyzed with ImageJ software (NIH) (Figure 17).

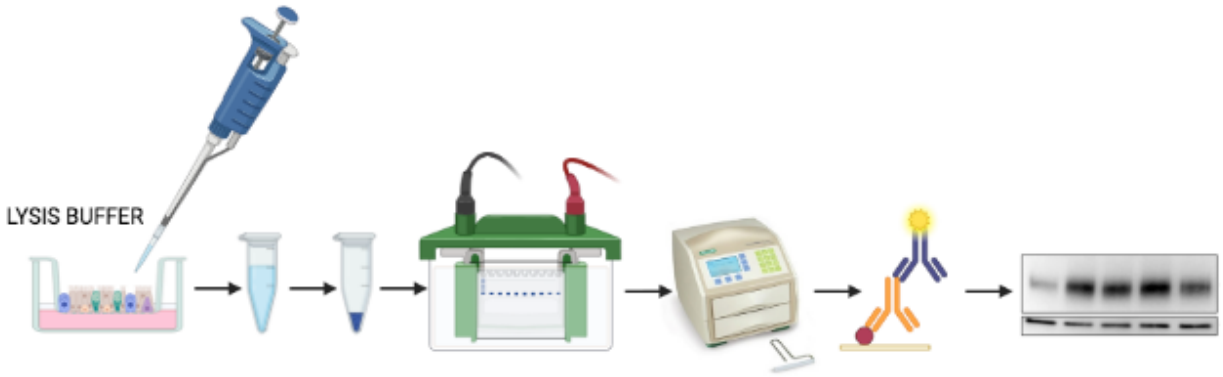

Figure 17: Experimental workflow for Western blot of bronchial epithelial cells. The bronchial epithelial cells grown on porous support were lysed. The obtained lysates were then processed for Western blot as described. Created with Biorender.com.

2.5 Short-circuit current recordings

Snapwell supports carrying differentiated bronchial epithelia were mounted in Ussing-like vertical chambers (EM-CSYS-8, Physiologic Instruments). Both apical and basolateral chambers were filled with 5 mL of a Ringer solution containing (in mM): 126 NaCl, 0.38 KH_2PO_4, 2.13 K_2HPO_4, 1 $CaCl_2$, 1 $MgSO_4$, 24 $NaHCO_3$, 10 glucose, and phenol red. Solution on both sides were bubbled with 5% CO_2/95% air and kept at 37°C. The transepithelial voltage was clamped at 0 mV with an 8-channel voltage-clamp amplifier (VCC MC8, Physiologic Instruments) connected to apical and basolateral chambers via Ag/AgCl electrodes and agar bridges (1M KCl in 2% agar). The resulting short-circuited current from each channel was recorded with the Acquire & Analyze 2.3 software (Physiologic Instruments) (Figure 18).

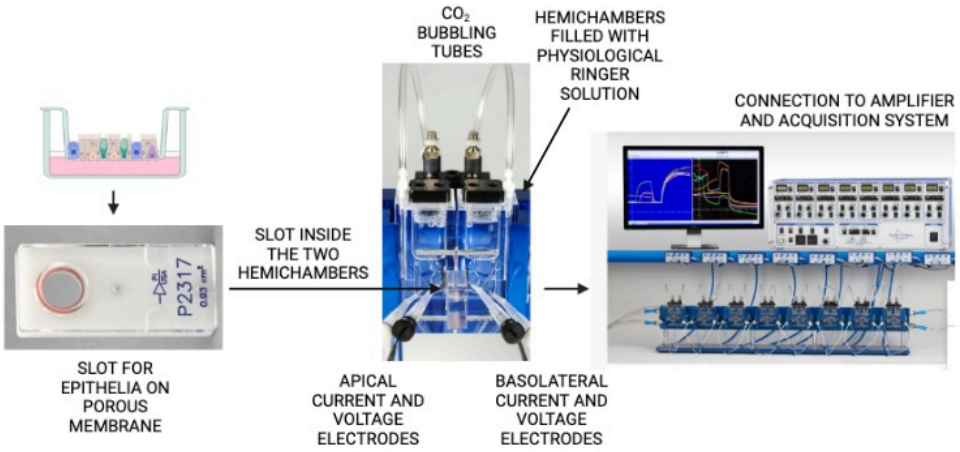

Figure 18: Schematic representation of short-circuit current recordings. The porous supports carrying the differentiated airway epithelia were mounted on a specific slot for Transwell or Snapwell and inserted in the vertical Ussing-like chamber, formed by the apical and basolateral hemichambers, both filled with Ringer solution and connected to voltage and current electrodes. Two connecting tubes allow 5% CO_2/95% air bubbling, and the instrument was heated to 37 °C. Every chamber is connected to a pre-amplifier and to the acquisition system. Created with Biorender.com.

2.6 Analysis of airway surface liquid (ASL) properties

2.6.1 Fluorescence Recovery After Photobleaching (FRAP) assay

Epithelial cells were plated on the bottom part of "flipped" Snapwell inserts. After cell adhesion, Snapwell inserts were returned to their normal position and medium was added to the top part of the Snapwell (basolateral with respect to cells) and removed from the bottom part. Epithelia were allowed to differentiate (2–3 weeks). For experiments done in the presence of HCO_3^-, the basolateral medium was PneumaCult ALI. For experiments done under HCO_3^--free conditions, the basolateral medium was Coon's modification of F12 containing 20 mM HEPES (pH 7.4). The apical epithelial surface was stained with 5 µL PBS containing FITC-Dextran (70 kDa, 2 µg/mL, Thermo Fisher Scientific). After 3 hours, Snapwells with epithelia were mounted on the stage of a Nikon Eclipse Ti-E Spinning Disk inverted microscope within a chamber that allowed control of temperature (37 °C) and atmosphere (humidified 5% CO_2/95% air or pure air depending on the presence of HCO_3^- in the basolateral medium). Images of the stained epithelial surface were sequentially acquired for 5 seconds before and 60 seconds after photobleaching of a preselected circular ROI (50 µm diameter). After normalization for the initial value, the recovery of fluorescence at 30 seconds from bleach pulse was measured (Figure 19).

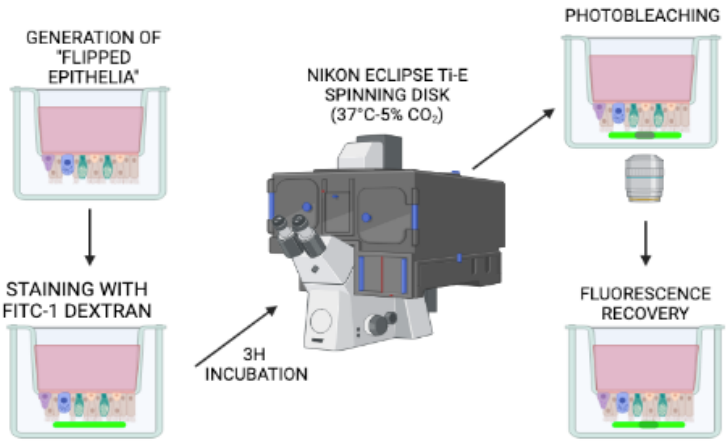

Figure 19: Experimental workflow for FRAP experiments. The bronchial epithelial cells were seeded on porous supports in upside-down configuration. The apical surface was stained with FITC-dextran and, after 3 hours of incubation, they were mounted on Nikon Eclipse Ti-E Spinning Disk in a controlled atmosphere. The photobleaching of a circular ROI was applied and the fluorescence recovery was followed. Created with Biorender.com.

2.6.2 Micro Particle Transport (MPT) assay

Black micro beads (6 µm diameter; 24293-5 Polybead Black Dyed Microspheres, Polysciences) suspended in 2 µL PBS were added to the apical side of epithelia. Microbead movement was recorded with a Leica M205FA Stereo microscope. Microbeads velocity was calculated with ImageJ using Manual Tracking plug-in (Figure 20).

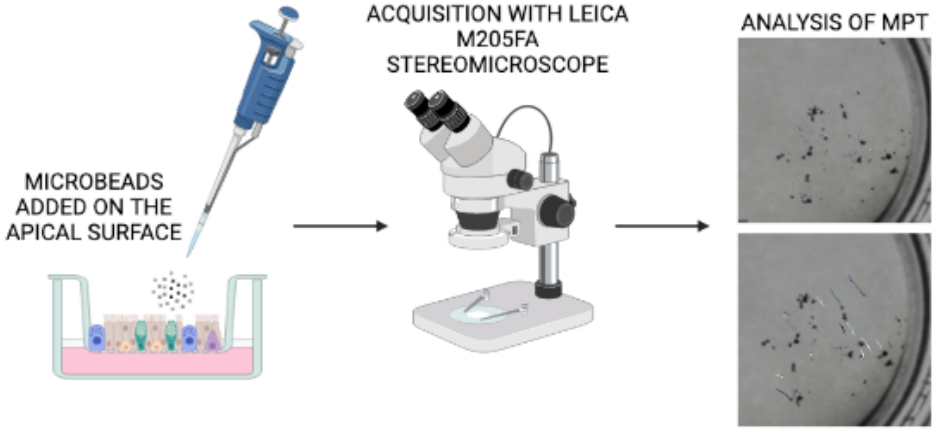

Figure 20: Experimental workflow for MPT. The bronchial epithelial cells were seeded on porous and black microbeads were added on the apical surface. Then MPT was acquired with Leica M205FA stereomicroscope and analyzed as reported. Created with Biorender.com.

2.7 pH measurements

2.7.1 Large-volume in situ pH assay

This assay was used to measure net ATP12A activity in HCO_3^--free conditions. In total, 60 µL of a modified PBS solution with low buffer capacity containing the pH-sensitive SNARF-1 probe coupled to 70 kDa dextran (0.1 mg/mL, D3304, Thermo Fisher Scientific) was added on the apical side of epithelia formed on Transwell inserts. The modified PBS solution had the following composition (in mM): 145 NaCl, 2.7 KCl, 0.81 Na_2HPO_4, 0.15 KH_2PO_4, 1 $CaCl_2$, 0.5 $MgCl_2$ (pH 7.35). The microplates carrying Transwell inserts were introduced in a FLUOstar Omega microplate reader (BMG LABTECH). Fluorescence was measured using single excitation (544

nm) and double emission (590 and 640 nm) at the beginning of treatment and every 60 minutes for 3 hours. The ratio of fluorescence emitted at 590 and 640 nm was converted to pH values using a calibration curve (Figure 21).

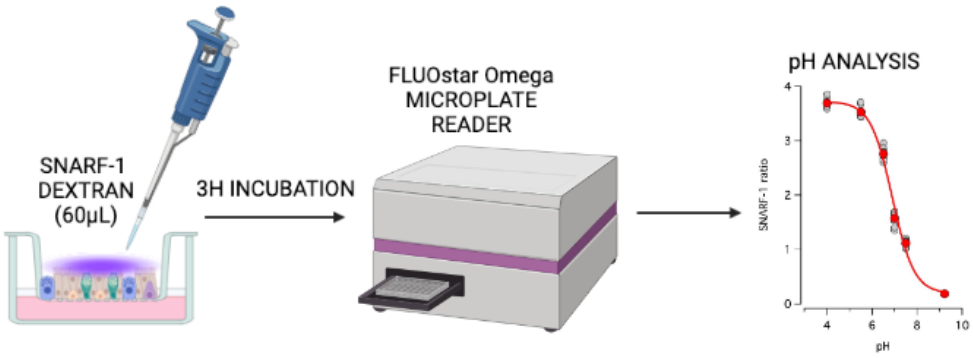

Figure 21: Experimental workflow for large volume in situ pH assay. 60 µl of SNARF-1 dextran +/- compounds were added on the apical surface and incubated for 3 hours. Then, fluorescence was read in a microplate reader and values of fluorescence were converted to pH through a calibration curve. Created with Biorender.com.

2.7.2 Large-volume ex situ pH assay

In total, 200 µL of PBS with/without compounds was added on the apical side of epithelia formed on Snapwell inserts. The saline solution was covered by 200 µL of mineral oil to avoid evaporation and CO_2 exchange with atmosphere. The basolateral medium was PneumaCult ALI for experiments done in the presence of HCO_3^- or Coon's modification of F12 containing 20 mM HEPES (pH 7.4) for HCO_3^--free conditions. Epithelia were then incubated at 37 °C in 5% CO_2/95% air or pure air atmosphere. After 6 hours, the apical fluid was recovered, centrifuged (2,000 g, 1 minute, room temperature) to separate the 2 phases of mineral oil and PBS. Then, 50 µL of the aqueous phase from each sample plus 0.5 µL of SNARF-1 were rapidly transferred to the wells of 96-well microplates. The fluorescence was measured in a FLUOstar Omega microplate reader (BMG LABTECH) using single excitation (544 nm) and double emission (590 and 640 nm). The ratio of fluorescence emitted at 590 and 640 nm was converted to pH values using a calibration curve (Figure 22).

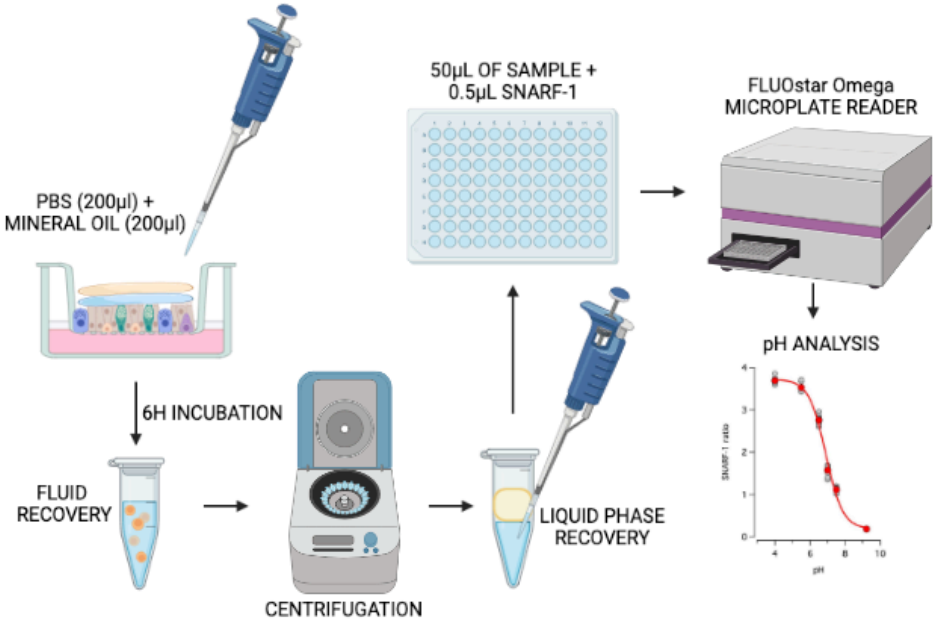

Figure 22: Experimental workflow for large volume ex situ pH assay. 200 µl of PBS +/- compounds plus 200 µl of mineral oil were added on the apical surface and incubated for 6 hours. Then, the fluid was recovered and centrifuged to separate the oil from the aqueous solution. 50 µl of the liquid phase were added to a 96-well plate with 0.5 µl of SNARF-1 dextran. Fluorescence was read in a microplate reader and values of fluorescence were converted to pH through a calibration curve. Created with Biorender.com.

2.7.3 Small-volume in situ pH assay

In total, 5 µL of PBS containing the SNARF-1 dextran conjugate was spotted on the apical side of epithelia on Snapwell inserts. After staining, epithelia were incubated for 3 hours at 37 °C. The basolateral medium was PneumaCult ALI medium (5% CO_2/95% air atmosphere). After incubation, the fluorescence was measured with a FLUOstar Omega microplate reader (BMG LABTECH) using single excitation (544 nm) and double emission (590 and 640 nm). The ratio of fluorescence emitted at 590 and 640 nm was converted to pH values using a calibration curve (Figure 23).

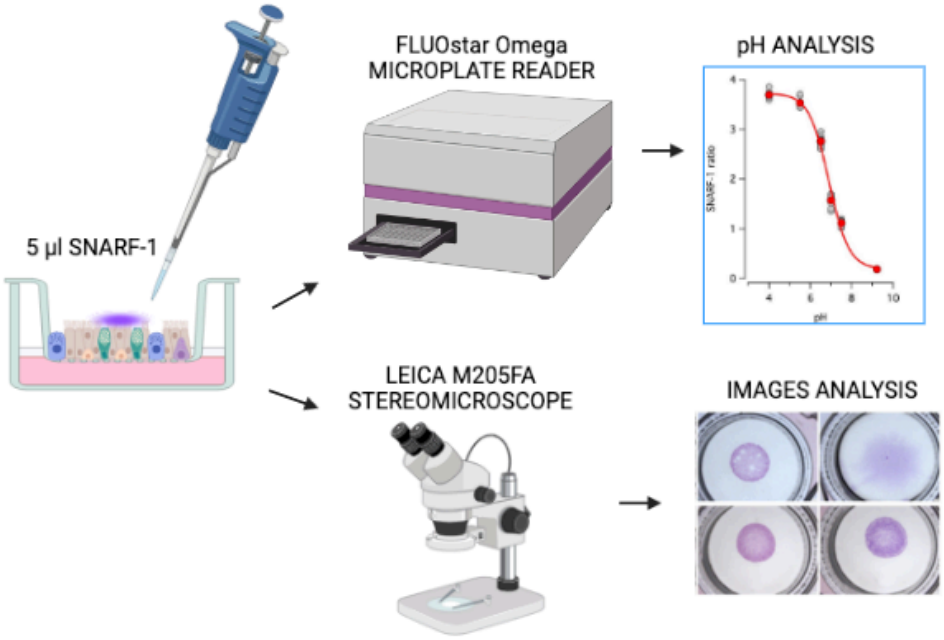

Figure 23: Experimental workflow for small volume in situ pH assay. 5 µl of SNARF-1 dextran were added on the apical surface and incubated for 3 hours. Then, fluorescence was read in a microplate reader and values of fluorescence were converted to pH through a calibration curve. At the same time, images of SNARF-1 spot were taken by Leica M205FA stereomicroscope. Created with Biorender.com.

2.8 Bulk mRNA sequencing

2.8.1 QuantSeq 3′ mRNA sequencing library preparation

Analysis of epithelial transcriptome was done on four non-CF and three CF separate preparations in which epithelia were treated with/without IL-17/TNF-α. An additional set of data included four separate non-CF epithelia preparations treated with/ without IL-4. Total RNA was extracted with Relia Prep RNA Cell Miniprep System (Z6011, Promega) according to the manufacturer's instructions. RNA concentration was determined with the Qubit 2.0 fluorimetric Assay (Thermo Fisher Scientific) and adjusted at 10 ng/µL. Libraries were prepared from 125 ng of total RNA using the QuantSeq 3′ mRNA-Seq Library Prep Kit FWD for Illumina (Lexogen GmbH). Quality of libraries was assessed using screen tape High Sensitivity DNA D1000 (Agilent Technologies). The amplified fragmented cDNA of 300 bp in size was sequenced in single-end mode using the

Illumina NovaSeq 6000 with a read length of 100 bp. Illumina NovaSeq base call (BCL) files were converted in fastq file through bcl2fastq (http://emea.support.illumina.com/content/dam/illuminasupport/documents/documentation/software_documentation/bcl2fastq/bcl2fastq2-v2-20-software-guide-15051736-03.pdf; version v2.20.0.422).

2.8.2 QuantSeq 3' mRNA sequencing data processing and analysis

Sequence reads were trimmed using bbduk software (https://jgi.doe.gov/data-and-tools/software-tools/bbtools/bb-tools-user-guide/bbduk-guide/) to remove adapter sequences, poly-A tails, and low-quality end bases (regions with average quality below 6). Alignment was performed with STAR 2.6.0a (Dobin et al., 2013) on hg38 reference assembly obtained from Cell Ranger website (https://support.10xgenomics.com/single-cell-gene-expression/software/release-notes/build#mm10_3.0.0; Ensembl assembly release 93). Expression levels of genes were determined with htseq-count (Anders et al., 2015) using Gencode/Ensembl gene model. Genes with an average number of CPM (counts per million) < 1 and percentage of duplicated reads > 20% were filtered out. Differential expression analysis was performed using edgeR (Robinson et al., 2010), a statistical package based on generalized linear models, suitable for multifactorial experiments. The threshold for statistical significance chosen was FDR < 0.05. Figure 32 (see Results 3.3) includes the 151 genes significantly induced in CF and non-CF epithelia by IL-17/TNF-α. Gene Ontology (GO) and Functional Annotation Clustering analyses were performed on these 151 genes 0by using DAVID Bioinformatic Resources (Huang et al., 2009a; Huang et al., 2009b) restricting the output to Biological Process terms (BP_FAT). The threshold for statistical significance of GOEA was FDR < 0.1 and enrichment score (i.e., the amount to which the genes in the cluster of Gene Ontology are overrepresented) was > 1.5.

2.8.3 Accession codes

The gene expression data were deposited in GEO with the SuperSeries accession no. GSE182958. The SuperSeries includes 3 data sets: the treatment with/without IL-4 on non-CF cells (GSE182955), the treatment with IL-17/TNF-α on CF cells (GSE182956), and the treatment with IL-17/ TNF-α on non-CF (GSE182957).

2.9 Single cell RNA-seq

Bronchial epithelial cells were detached from Snapwell inserts as single cells through the following protocol: both apical and basolateral side were washed with PBS without Ca^{2+} and Mg^{2+}, and they were then incubated for 30 minutes with Versene and for a further 15 minutes in 10x concentrated trypsin solution at 37 °C. Cells were collected directly in New Zealand serum plus 10% DMSO, frozen for 24 hours at –80 °C, and then stored in liquid nitrogen. For sequencing, single cells were suspended in phosphate buffered saline containing 0.04% BSA, filtered using a 40 μm cell strainer (Biologix), and counted with LUNA-II Automated Cell Counter (Logos Biosystems). The cell suspension was loaded onto the Chromium Single Cell G Chip Kit (10x Genomics) and run on the Chromium Single Cell Controller (10x Genomics) to generate single-cell gel bead emulsion, according to the manufacturer's protocol. The single cell 3′ Library and Gel Bead Kit V3.1 (10x Genomics) was used to generate cDNA and the final libraries. The cDNA quality was assessed using high-sensitivity D5000 screen tape on Agilent 4200 TapeStation system (Agilent Technologies). Quality of libraries was assessed by using screen tape High sensitivity DNA D1000 (Agilent Technologies). Finally, the libraries were sequenced on Novaseq6000 sequencer (Illumina) according to manufacturer specifications. Sequencing was done by Next Generation Diagnostics. Raw base call generated by sequencing was demultiplexed by using cellranger mkfastq (Zheng et al., 2017) with standard parameters. Then, FASTQ files from cellranger mkfastq were aligned, filtered, and counted with cellranger count (Zheng et al., 2017) with standard parameters. The output counted data were then used for downstream analysis using Seurat (4.0.4) (Hao et al., 2021). Only cells with mitochondrial rate < 15% were retained. Moreover, cells showing less than 500 genes and less than 1,000 unique molecular identifiers (UMIs) were discarded. Data were normalized using NormalizeData() function with LogNormalize method and scale factor = 10,000. Data were then scaled through the ScaleData() function, by taking all genes as features parameter. PCA dimensionality reduction was performed using RunPCA(), using, as features, the ones obtained by running the function VariableFeatures() on the data sets. Then, FindNeighbors(), FindClusters(), and the nonlinear dimensionality reduction RunUMAP() functions were used in order to obtain the 2D maps and the clusters for each analysis. Marker genes of each cluster were identified by using the FindAllMarkers() function using the Wilcoxon rank-sum test comparing cells in each cluster with all other cells in the data set.

2.10 Data visualization

Heatmaps and Venn diagrams were generated using custom annotation scripts. All graphs and figures were prepared with Igor Pro (WaveMetrics).

2.11 Statistics

Quantitative data are shown as scatter dot plots with mean ± SD. Each symbol in the plots represents the result of an independent experiment. To assess significant differences between groups of data, we first used the Kolmogorov-Smirnov test to evaluate normal distribution. For normally distributed data, we then used 2-tailed Student's *t* test, in case of two groups, or one-way ANOVA, for more than two groups. ANOVA was followed by Dunnett's or Tukey's post hoc tests, as appropriate. For data with nonnormal distribution, we used nonparametric tests: Mann-Whitney *U* for two groups and Kruskal-Wallis with Dunn's test for more than two groups. Statistical analysis was done with PRISM software (GraphPad).

2.12 Study approval

The collection of nasal epithelial cells by brushing and the collection of human bronchi from explanted lungs to generate cultures of epithelial cells were approved by the relevant Ethical Committee with the registration numbers CER 28/2020 and ANTECER 042-09/07/2018.

3. RESULTS

All present results have been published in Guidone et al., 2022.

3.1 ATP12A expression in nasal brushing

In a previous study, we found strong ATP12A expression in the bronchial epithelium of CF patients undergoing lung transplants (Scudieri et al., 2018). We asked whether ATP12A upregulation was a consequence of the advanced stage of the disease. Therefore, we investigated ATP12A expression in the nasal mucosa of CF patients of various age and clinical conditions. For this purpose, we adopted a simple nasal brushing procedure that we recently developed (Scudieri et al., 2020). After brushing, detached cells were immediately fixed and processed for immunofluorescence. Figure 24 shows that cells from many CF patients have enhanced expression of ATP12A in the apical membrane (AM). Furthermore, many CF samples showed unusual ATP12A expression in ciliated cells (Figure 24, CF7 sample).

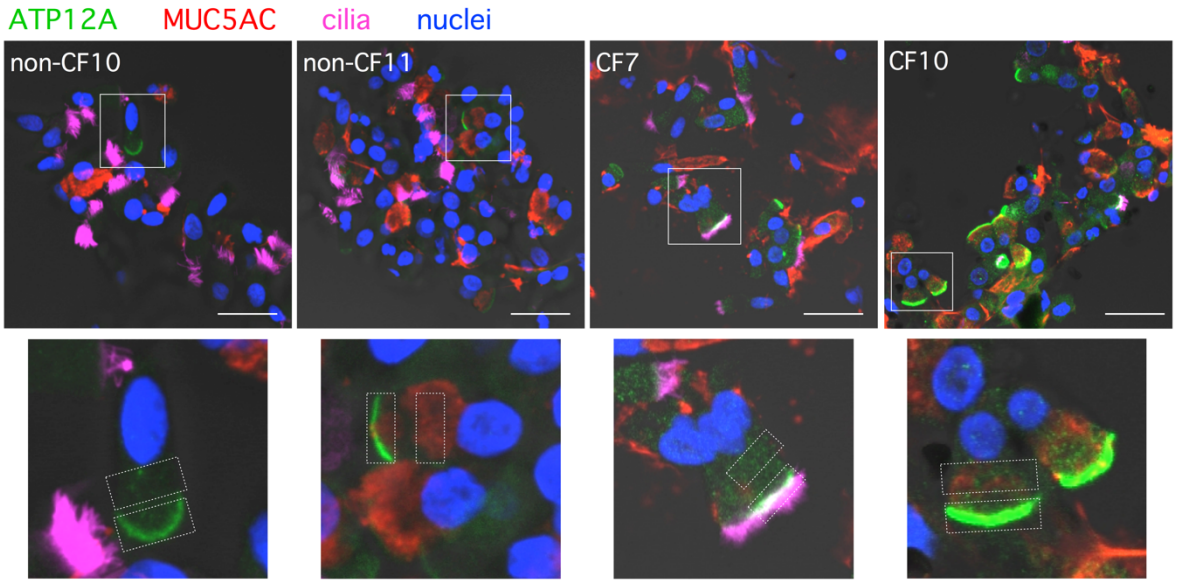

Figure 24. Detection of ATP12A protein in nasal brushings. Low-magnification (top) and high-magnification (bottom) of representative confocal microscope images showing ATP12A protein (green) in freshly fixed nasal brushings derived from non-CF (left) and CF (right) patients. MUC5AC (red) and acetylated tubulin (i.e., cilia, magenta) were also detected. Rectangles in the low-magnification images indicate the magnified regions. Rectangles in the high-magnification images show areas that were considered for ATP12A expression analysis. Scale bar: 20 μm. Adapted from Guidone et al., 2022.

By combining results from 14 non-CF control individuals and 35 CF patients, we found that ATP12A was significantly more expressed in CF, with some patients showing a percentage of ATP12A-expressing cells as high as 50% to 60% (Figure 25, top left). Interestingly, ATP12A was also significantly upregulated in non-CF individuals with rhinitis at the time of brushing (Figure 25, top left). Because of the broad range of ATP12A expression in CF samples, we plotted the percentage of ATP12A-expressing cells versus age or pulmonary function indicated by forced expiratory volume in the first second (FEV1). We found no correlation (Figure 25, top right and bottom left). There was high ATP12A expression irrespective of age, so that even very young patients (<10 years) had high expression. ATP12A is typically expressed in non-ciliated mucus-producing cells (Scudieri et al., 2018). However, it has been shown, by scRNA-Seq, that ATP12A expression can appear in ciliated cells as an early sign of inflammation and trans-differentiation to goblet cells (Vieira-Braga et al., 2019). Interestingly, in nasal samples, we found a correlation between ATP12A expression in the global cell population and extent of localization in ciliated cells (Figure 25, bottom right). This finding suggests that ATP12A expression is related to the status of mucosal inflammation.

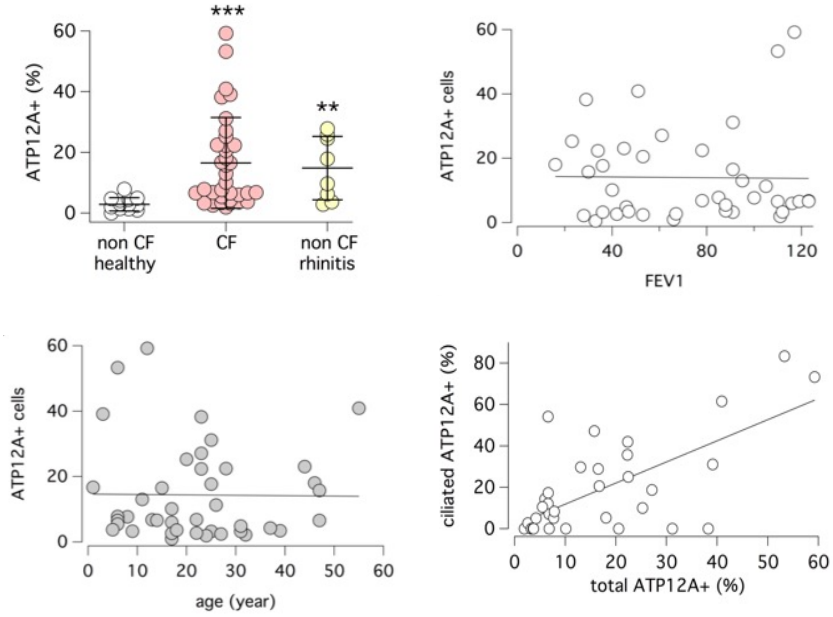

Figure 25. Analysis of ATP12A protein detection in nasal brushings. Top, left: scatter dot plot showing percentage of ATP12A$^+$ cells in non-CF healthy individuals, CF patients, and in subjects with rhinitis. **, $p < 0.01$; ***, $p < 0.001$ versus healthy control group (Kruskal-Wallis followed by Dunn's post hoc test). Top, right: percentage of ATP12A$^+$ cells vs. FEV1, the straight line shows the best linear fit of the data. Bottom, left: percentage of ATP12A$^+$ cells vs. age, the straight line shows the best linear fit of the data. Bottom, right: percentage of ATP12A$^+$ ciliated cells versus percentage of ATP12A$^+$ cells in the total population, the straight line shows the best linear fit of the data (Pearson's $R = 0.6743$, $p < 0.001$). In all graphs: each symbol reports the average value of a single patient. Adapted from Guidone et al., 2022.

3.2 ATP12A expression in bronchial epithelial cells treated with proinflammatory cytokines

We treated bronchial epithelia in vitro with a panel of proinflammatory cytokines to further investigate the link between ATP12A expression and inflammation. In particular, we chose IL-1β and IL-17 plus TNF-α, stimuli that are associated with mucus hypersecretion and neutrophilic infiltration, respectively (Chen et al., 2020; Rehman et al., 2020). In parallel, we also tested IFN-α, IFN-γ, and IL-6 as representative of other types of proinflammatory stimuli. After treatment (72 hours), ATP12A expression was investigated by immunofluorescence. We found that the IL-17/TNF-α combination was particularly effective in increasing the percentage of cells expressing ATP12A with respect to control and all other treatments (Figure 26).

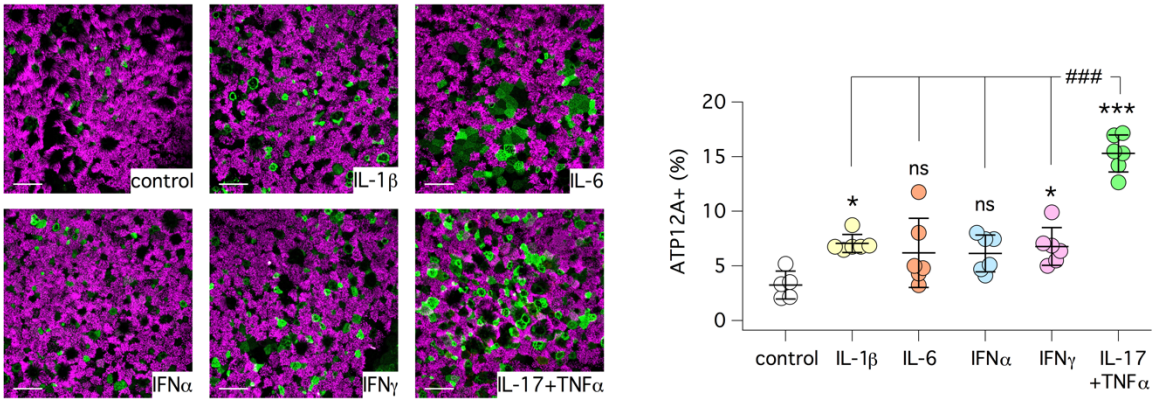

Figure 26. Upregulation of ATP12A by IL-17/TNF-α by immunofluorescence analysis. Left: representative confocal microscope images showing detection of ATP12A (green) and acetylated tubulin (i.e., cilia, magenta). Images are xy scans of CF cultured bronchial epithelial cells treated for 72 hours with/without cytokines (10 ng/mL for IL-6, IL-1β, TNF-α, IFN-α, and IFN-γ; 20 ng/mL for IL-17). Scale bar: 25 μm. Right: scatter dot plot reporting percentage of $ATP12A^{+}$ cells in bronchial epithelia with indicated treatments. *, $p < 0.05$; ***, $p < 0.001$ versus control; ###, $p < 0.001$ between indicated conditions (ANOVA and Tukey's post hoc test). Adapted from Guidone et al., 2022.

This effect was also investigated by immunoblot. The IL-17/TNF-α combination, as well as IL-4, significantly increased the ATP12A band in both CF and non-CF epithelia (Figure 27).

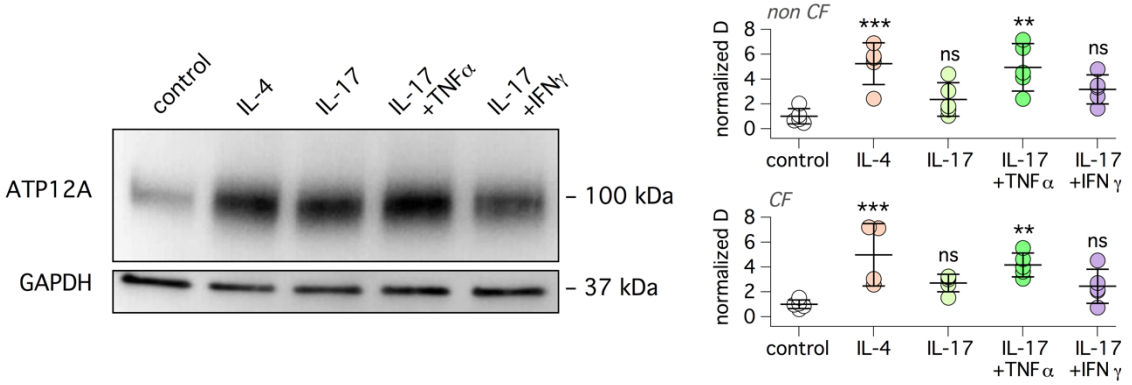

Figure 27. Upregulation of ATP12A by IL-17/TNF-α by Western blot analysis. Representative images (left) and summary of data (right) deriving from Western blot analysis of ATP12A protein in lysates of bronchial epithelial cells treated with/without single cytokines or cytokine combinations. The scatter dot plots report the band intensity for ATP12A normalized for GAPDH expression. Data were obtained from 5 CF and 5 non-CF bronchial cell preparations. **, $p < 0.01$; ***, $p < 0.001$ versus control (ANOVA and Dunnett's post hoc test). Adapted from Guidone et al., 2022.

We evaluated ATP12A function by measuring pH under HCO_3^--free conditions (large volume in situ pH assay, see Materials and Methods 2.7.1). We added the pH-sensitive fluorescent probe SNARF-1 conjugated to high–molecular weight dextran, dissolved in a modified PBS (60 µL, pH 7.3) with low buffer capacity, to the apical side of epithelia. This solution also contained ouabain (ATP12A inhibitor), bafilomycin A1 (V-ATPase inhibitor), both compounds together, or vehicle. The basolateral culture medium was buffered with Hepes (pH 7.4). Fluorescence was recorded and pH was calculated at the starting point and after 1- and 3-hours following probe addition. Figure 28 shows that non-CF and CF epithelia acidify the apical solution after 3 hours. Unexpectedly, acidification was more marked in non-CF epithelia, with pH values close to 6.5 (Figure 28, left). Inclusion of proton pump inhibitors also led to some unexpected results. In non-CF cells, bafilomycin A1 and ouabain were both effective in partially reducing the acidification, and combination of the two compounds had an additive effect. In contrast, CF cells were mostly sensitive to ouabain and not to bafilomycin A1 (Figure 28, right).

Treatment of CF and non-CF epithelia with IL-17/TNF-α induced marked acidification that was exclusively sensitive to ouabain. In fact, the bafilomycin-sensitive component observed in non-CF epithelia under untreated conditions disappeared after cytokine treatment.

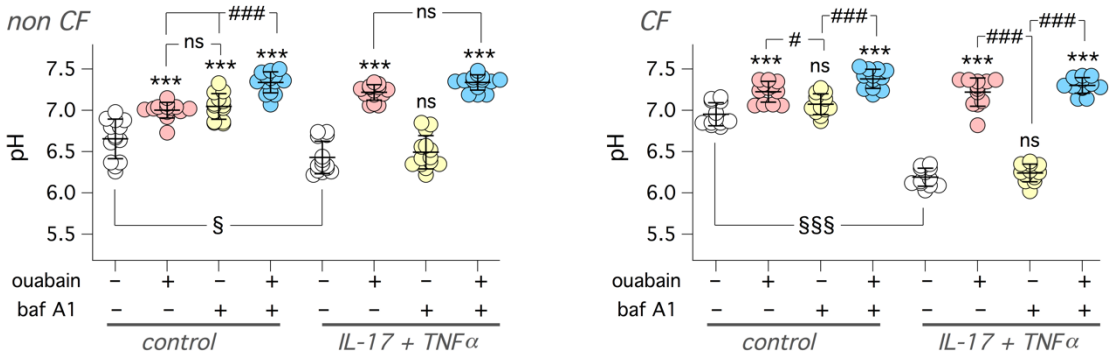

Figure 28. Upregulation of ATP12A function by IL-17/TNF-α. Apical fluid pH measurements with SNARF-1 dextran probe in non-CF (left) and CF (right) bronchial epithelia. Cells were treated with/without IL-17 + TNF-α. Experiments were done in HCO_3^--free conditions. Where indicated, the apical solution contained ouabain (200 μM), bafilomycin A1 (100 nM), or both compounds together. pH was measured after 3 hours of incubation under CO_2-free conditions. ***, $p < 0.001$ versus control; #, $p < 0.05$ and ###, $p < 0.001$ between indicated conditions; §, $p < 0.05$ and §§§, $p < 0.001$ for treated versus untreated epithelia (ANOVA and Tukey's post hoc test). Adapted from Guidone et al., 2022.

3.3 QuantSeq analysis of IL-17 plus TNF-α treatment on bronchial epithelial cells

We analyzed the effect of IL-17 plus TNF-α at the transcriptome level using the QuantSeq 3′ mRNA-Seq. For comparison, we also investigated the individual effects of IL-17, TNF-α, and IL-4. This analysis revealed a profound change elicited by the IL-17/TNF-α combination, with upregulation of many genes. Figure 29 shows data for the 80 top upregulated genes, with SLC26A4 at the top of the list. The extent of upregulation ranged from approximately 60-fold (SLC26A4) to 4-fold (KCNE3). The list includes genes involved in transepithelial transport (SLC26A4, SLC5A8, SLC5A1, SLC6A20), cytokine/chemokine signaling (CSF3, IL-19, CCL20, CXCL6, CXCL5, CXCL1), and modulation of immune response and antimicrobial activity (IDO1, NOS2, DEFB4A, LTF, DEFB4B).

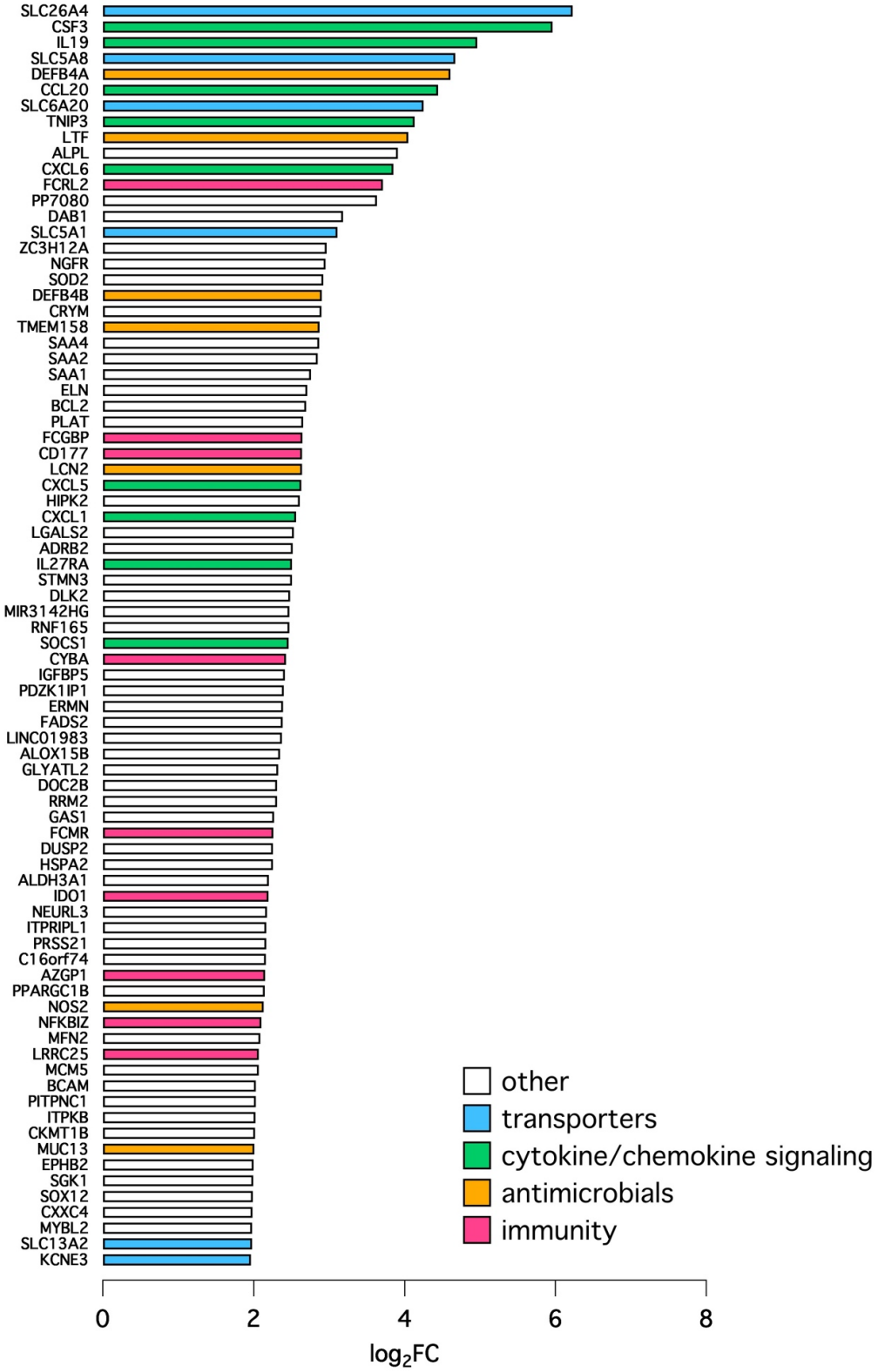

Figure 29. Top 80 genes upregulated by IL-17/TNF-α combination in cultured bronchial epithelia. The bar graph shows the extent of expression of indicated genes as determined by bulk RNAseq in non-CF cultured bronchial epithelia, in term of log_2fold change respect to control. Color codes indicate gene function. Adapted from Guidone et al., 2022.

A selection of genes, with relevance to the topic of our study — i.e., ion transport and defense function — is shown in Figure 30. In addition to SLC26A4, the IL-17/TNF-α combination also increased the expression of ADRB2 (the β2-adrenergic receptor), the kinase SGK1, the ENaC subunits SCNN1B and SCNN1A, mucin MUC5B, and ATP12A. The extent of gene expression increase was relatively modest (between 5- and 2-fold) compared with that of the most upregulated genes (Figure 29). The effects of IL-17/TNF-α combination for these selected genes were more like those of IL-17 alone (Figure 30). For example, SLC26A4 was upregulated by IL-17 but not by TNF-α. It is important to note that the analysis of IL-4 treatment revealed important differences (Figure 30). For example, IL-4 increased the expression of MUC5AC and not of MUC5B, which was instead downregulated. Also, in agreement with our previous studies (Scudieri et al., 2012; Gorrieri et al., 2016; Caputo et al., 2008), IL-4 enhanced the expression of the ANO1 (TMEM16A) Ca^{2+}-activated Cl^- channel, which was instead unaffected by IL-17/TNF-α (Figure 30). Furthermore, the upregulation of ATP12A was more marked in IL-4–treated epithelia.

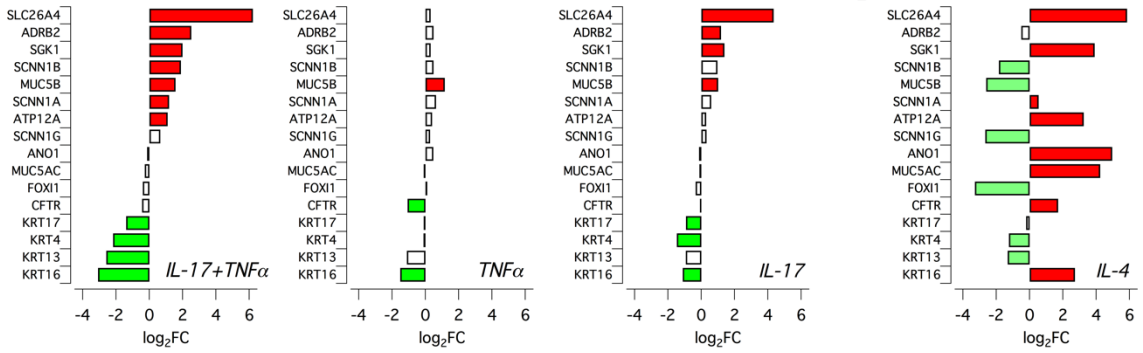

Figure 30. Analysis of gene expression changes in epithelia treated with inflammatory stimuli. Bar graphs report the expression changes for indicated genes in epithelia treated with IL-17 + TNF-α, TNF-α, IL-17, and IL-4. Data were obtained by RNA-Seq. Red and green indicate statistically significant upregulation and downregulation, respectively. Adapted from Guidone et al., 2022.

The transcriptomic changes elicited by IL-17/TNF-α were investigated with functional annotation tools to identify the specific biological processes involved. Enriched processes include the response to bacteria and to bacterial components, cytokine production, mucosal immune response, and TLR signaling pathway (Figure 31, left). The Venn diagram (Figure 31, right) instead shows the comparison of the 3 gene expression profiles of cells treated with the IL-17/TNF-α in combination and with the single cytokines.

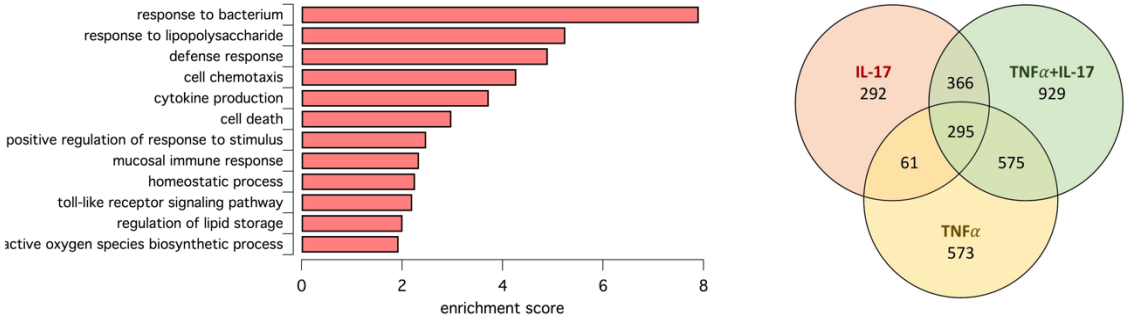

Figure 31. Analysis of biological processes modulated in epithelia treated with inflammatory stimuli. Left: biological processes that were associated with gene expression changes induced by TNF-α/IL-17 treatment. Right: Venn diagram showing extent of overlap for genes whose expression was upregulated by indicated cytokine treatment. Adapted from Guidone et al., 2022.

The heatmaps in Figure 32 show that the gene expression changes in CF and non-CF epithelia elicited by IL-17/TNF-α were quite similar.

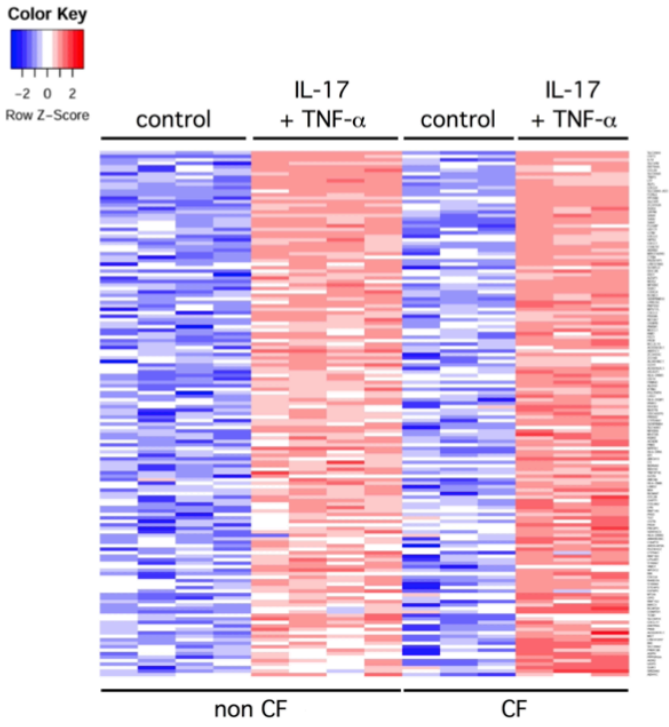

Figure 32. Comparison of gene expression changes induced by IL-17/TNF-α in non-CF and CF cultured bronchial epithelia. The heat maps show the change in expression for the top 150 upregulated genes in CF and non-CF epithelia. Adapted from Guidone et al., 2022.

3.4 Single cell RNA-Seq of IL-17 plus TNF-α treatment on bronchial epithelial cells

We applied scRNA-seq to further analyze the effects of IL-17/TNF-α treatment. The images in the top part of Figure 33 summarize the gene expression profile under control conditions and after treatment. The top graphs report the position of cells in the 2D uniform manifold approximation and projection (UMAP). Each dot represents a single cell. Cells with similar transcriptomes are positioned close to each other, forming clusters numbered from 0 to 10. The images in the bottom part of Figure 33 show expression of particular genes selected because they are either markers of specific cell types (e.g., KRT5 for basal cells, FOXJ1 for ciliated cells, FOXI1 for ionocytes) or because they are modulated by IL-17/TNF-α. The cytokine combination markedly changes gene expression in the epithelium, as highlighted by the nature of the clusters. For example, cluster 2, which corresponds to basal cells (high KRT5 expression), almost does not contain treated cells. Instead, cluster 1 is strongly enriched in treated cells and shows predominant expression of genes induced by IL-17/TNF-α: SLC26A4, MUC5B, ADRB2, and ATP12A (Figure 33, bottom). Also, clusters 4–6 — which, based on FOXJ1 expression, probably represent ciliated cells — show a change in their transcriptional state. Clusters 4 and 6 contain more cells in untreated epithelia, while cluster 5 is enriched in treated epithelia.

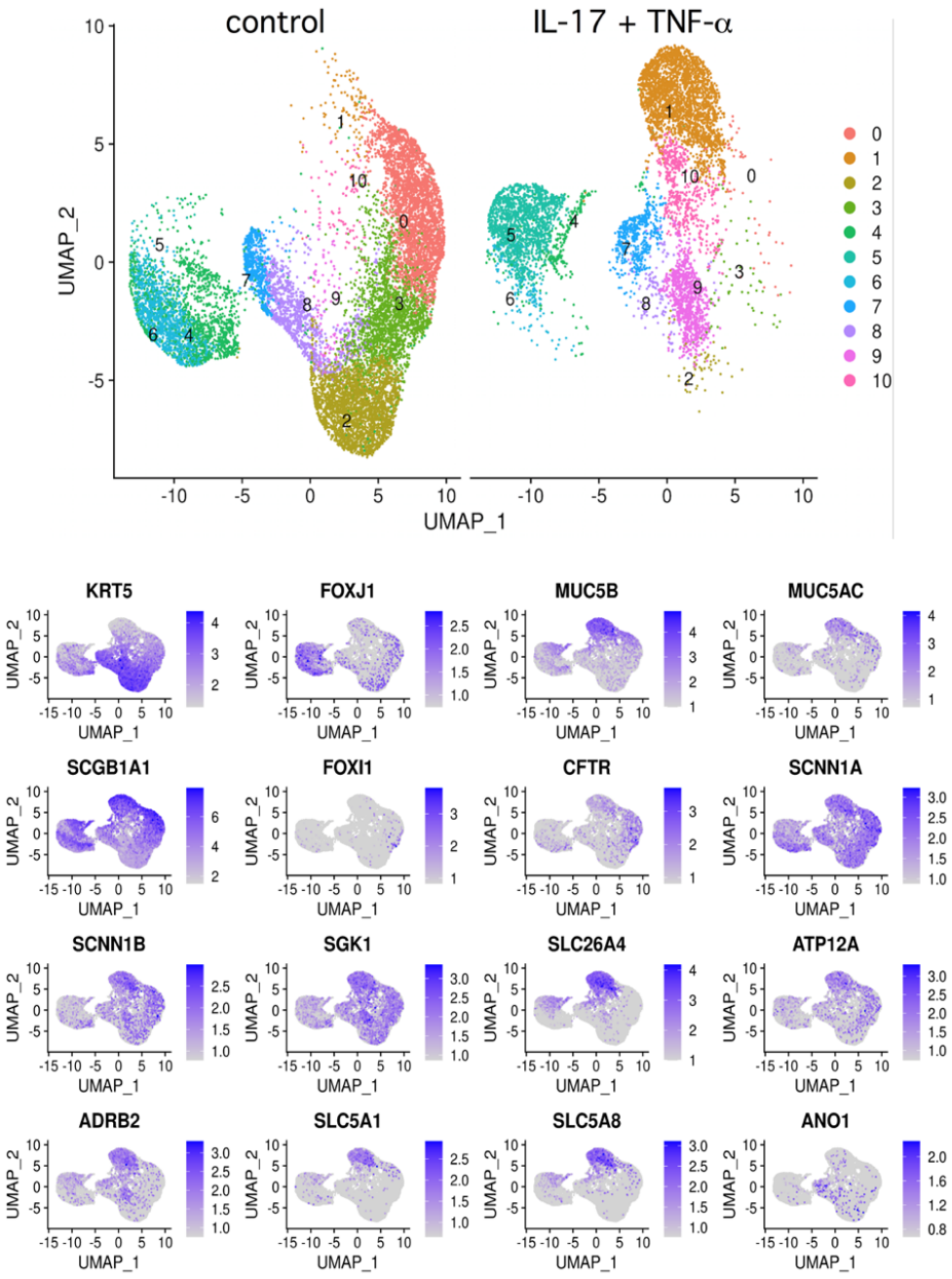

Figure 33. Analysis of epithelial transcriptome by scRNA-Seq. Top: global representation of gene expression in epithelia kept under control conditions (left) or treated with IL-17/TNF-α (right). Each dot represents a single cell, whose position in the 2D map reports the transcriptional similarity with respect to the neighbor cells. The different colors and numbers correspond to cells clusters with similar transcriptome. Bottom: two-dimensional maps showing the expression of indicated genes within the epithelial cell population. MUC5B, SLC26A4, ATP12A, ADRB2, SLC5A1, and SLC5A8 expression is particularly concentrated in the region corresponding to cluster 1, which is enriched by IL-17/TNF-α treatment. Adapted from Guidone et al., 2022.

3.5 Modification of electrogenic ion transport by IL-17/TNF-α

We carried out short-circuit current recordings on non-CF and CF epithelia to evaluate the effect of IL-17/TNF-α on electrogenic ion transport (Figure 34). During recordings, we sequentially added: (a) amiloride (10 μM), to block ENaC-dependent Na^+ absorption; (b) CPT-cAMP (100 μM) followed by $CFTR_{inh}$-172 (10 μM) to activate and inhibit CFTR, respectively; and (c) UTP (100 μM) and Ani9 (10 μM) to induce and block Ca^{2+}-activated Cl^- secretion through TMEM16A (ANO1). Treatment with IL-17/TNF-α induced a significant increase in ENaC activity (i.e., the amplitude of amiloride effect) in both CF and non-CF epithelia. This effect was unexpected, since other cytokines — namely, IL-4, IL-13, and IL-1β — actually decrease ENaC activity (Danahay et al., 2002; Galietta et al., 2002; Gray et al., 2004). CFTR current was also increased by IL-17/TNF-α, as recently reported (Rehman et al., 2021), and this effect could be even detected in CF epithelia, despite the very low level of CFTR function. Instead, the response to UTP was not increased, in agreement with unaltered TMEM16A gene expression.

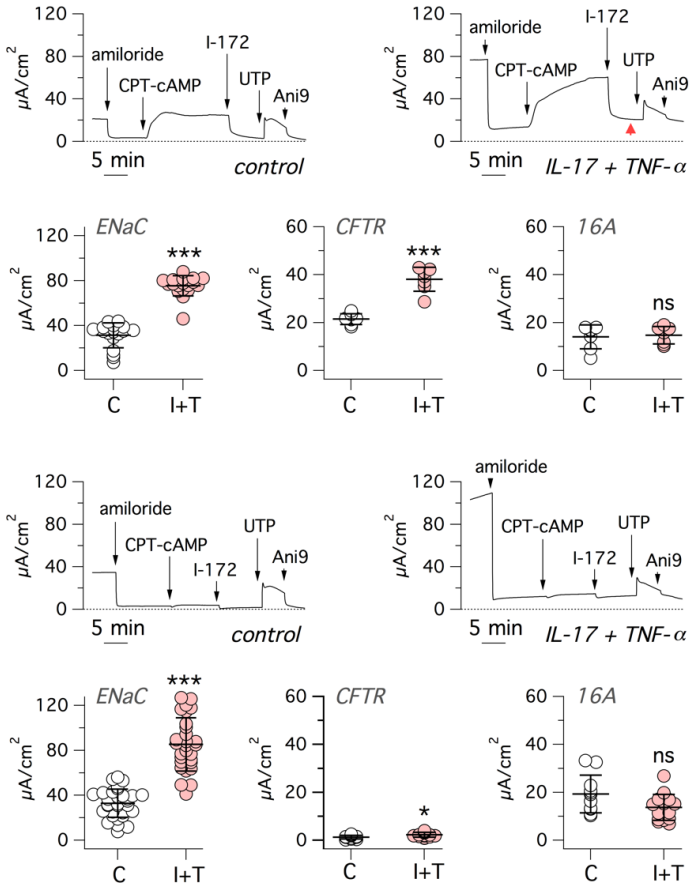

Figure 34. Modification of electrogenic ion transport by IL-17/TNF-α. Representative traces and summary of data from short-circuit current recordings done on non-CF (top) and CF (bottom) bronchial epithelia, treated with/without IL-17/TNF-α combination. During recordings, epithelia were sequentially exposed to: amiloride (10 μM), CPT-cAMP (100 μM), $CFTR_{inh}$-172 (I-172, 20 μM), UTP (100 μM), and Ani9 (5 μM). Red arrowhead: higher residual current in cytokine treated epithelia. The scatter dot plots report, for control and IL-17/TNF-α–treated (I+T) epithelia, the amplitude of amiloride, $CFTR_{inh}$-172, and UTP effects, which are representative of ENaC, CFTR, and TMEM16A function, respectively. *, $p < 0.05$; **, $p < 0.01$; and ***, $p < 0.001$ versus control (Mann-Whitney U test). Adapted from Guidone et al., 2022.

It can be noticed in the representative traces shown in Figure 34 (red arrowhead), that epithelia treated with IL-17/TNF-α show higher levels of basal current that persist even after addition of amiloride and $CFTR_{inh}$-172. This current was also resistant to Ani9, an effective blocker of TMEM16A (Figure 34). We hypothesized that the baseline current elicited by the cytokine combination is due to another electrogenic transport, possibly Na^+-dependent glucose uptake at the apical membrane. Indeed, the mRNA for SLC5A1 (also referred to as SGLT1, the sodium/glucose cotransporter) was upregulated (8-fold; Figure 29) by IL-17/TNF-α. Accordingly, we tested mizagliflozin, a potent and selective inhibitor of SLC5A1. This compound caused a large drop of the baseline current in cytokine treated epithelia (Figure 35). In fact, the currents remaining after mizagliflozin addition in control and cytokine-treated epithelia were comparable.

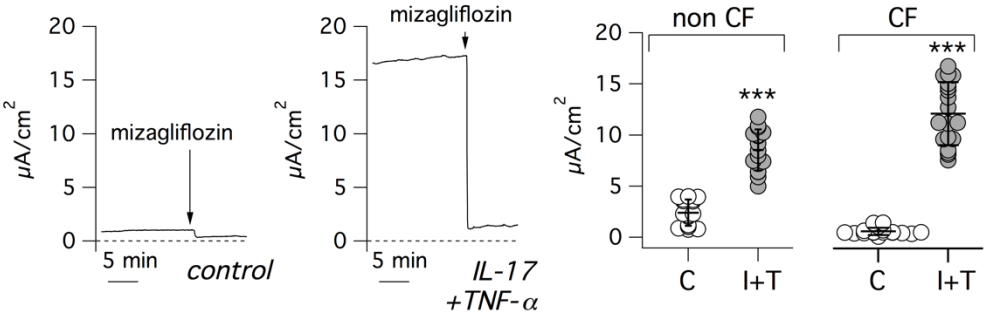

Figure 35. Functional upregulation of SLC5A1 transport by IL-17/TNF-α. Representative short-circuit current recordings (left) and summary of data (right) showing effect of mizagliflozin (10 μM) on control and IL-17/TNF-α–treated (I+T–treated) epithelia. Mizagliflozin was added in the presence of amiloride, $CFTR_{inh}$-172, and Ani9. ***, $p < 0.001$ versus control (Mann-Whitney U test). Adapted from Guidone et al., 2022.

3.6 Mechanism of ENaC upregulation by IL-17/TNF-α

We were intrigued by the marked upregulation of ENaC function elicited by IL-17/TNF-α. Since the increase in SCNN1A and SCNN1B transcripts was small (Figure 30), we considered the possibility of a post-transcriptional mechanism. ENaC activity is known to be regulated by proteolytic activation (Gaillard et al., 2010; Rossier & Stutts, 2009). Therefore, we tested the effect of elastase (Figure 36). Elastase was ineffective on epithelia kept under control conditions or treated with IL-17/TNF-α (Figure 36, top traces), indicating that ENaC is fully cleaved in both conditions and that the effect of the cytokine combination is not mediated by an increase in ENaC proteolysis. In parallel experiments, we incubated epithelia for 18 hours with the protease inhibitor camostat, which is effective on the proteases that regulate ENaC (Coote et al., 2009). As expected, camostat treatment reduced the size of ENaC currents and subsequent addition of elastase to camostat-treated epithelia resulted in rapid activation of currents (Figure 36, bottom traces). The activating effect of elastase demonstrates that camostat reduces ENaC activity by preventing its proteolysis. Interestingly, we noticed a difference in the fraction of the total current that was sensitive to elastase treatment. This parameter was smaller in epithelia treated with IL-17/TNF-α (Figure 36).

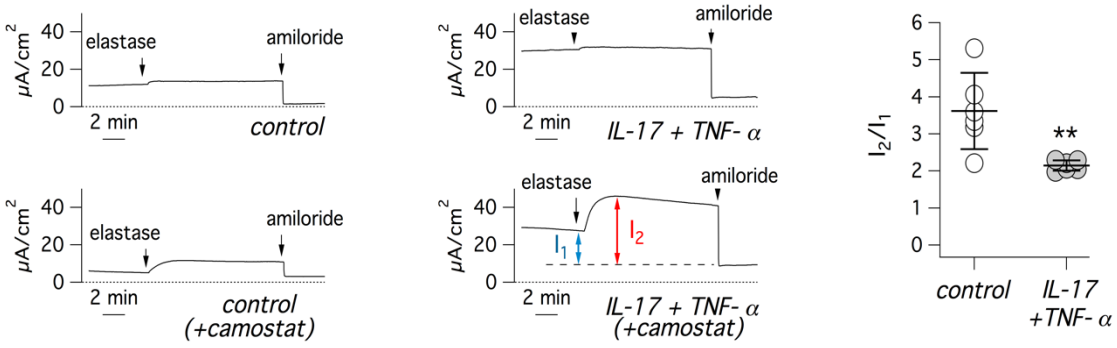

Figure 36. Mechanism of ENaC upregulation by IL-17/TNF-α. Representative short-circuit current traces (left) and summary of data (right) for experiments on epithelia treated with/without IL-17/TNF-α for 72 hours. During recordings, elastase (1.5 μM) and amiloride (10 μM) were sequentially added. Where indicated, epithelia were apically treated with camostat (3 μM) for 18 hours. The scatter dot plot shows, for experiments with camostat pretreatment, the ratio I2/I1, where I1 and I2 are the current amplitudes before and after elastase, as indicated by blue and red arrows, respectively. **, $p < 0.01$ (Student's t test). Adapted from Guidone et al., 2022.

Since the ENaC turnover at the plasma membrane — dependent on channel insertion, proteolytic activation, and internalization — is quite fast (de la Rosa et al., 2002; Kabra et al., 2008), we also added camostat during recordings of epithelia previously treated with/without IL-17/TNF-α (Figure 37). Camostat caused a rapid reduction in transepithelial current. We added amiloride during this decay phase. There was a sharp drop of the current that then reached a stable level. This behavior indicates that the current rundown caused by camostat is based on ENaC inhibition; otherwise, it would have continued in the presence of amiloride. Importantly, we noticed a difference in the time course of the decay between control- and IL-17/TNF-α–treated cells. The time required to reach half of the initial amplitude in control-treated epithelia was 10–14 minutes, a value comparable with what was previously reported: 11–17 minutes (de la Rosa et al., 2002; Kabra et al., 2008). With IL-17/TNF-α, the decay was instead significantly slower, with a mean half-time of ~28 minutes in both CF and non-CF epithelia (Figure 37). It is also interesting to note that the trend of the camostat-induced decay is different between control- and IL-17/TNF-α–treated epithelia. In the control condition, the decay appears to follow a single exponential fashion. With the cytokine combination, the decay appears biphasic, with an initial small and relatively rapid decay followed by a large and slower linear phase.

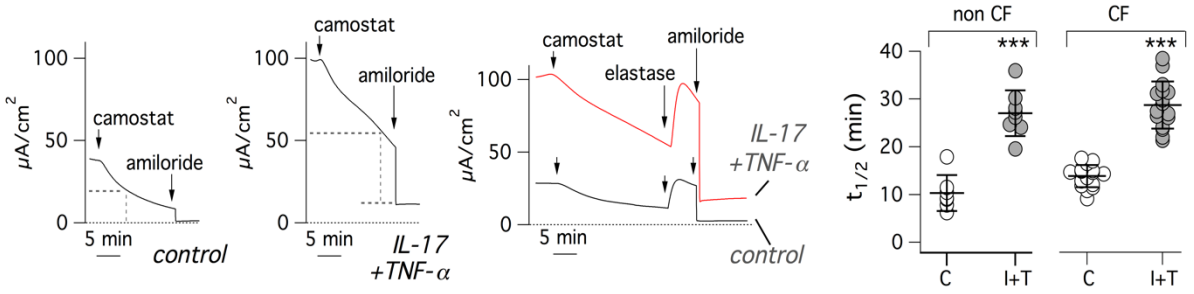

Figure 37. Analysis of ENaC current rundown induced by camostat. Left: Representative traces from experiments with/without IL-17/TNF-α treatment in which camostat (3 μM) and amiloride were sequentially added. Where indicated, experiments also included addition of elastase (1.5 μM) after camostat. Right: summary of data showing the rate of ENaC current decay after camostat addition (C, control; I+T, IL-17/TNF-α). Data ($t_{1/2}$) report the time at which the current decayed to half of initial amplitude. ***, $p < 0.001$ (Student's t test). Adapted from Guidone et al., 2022.

The representative immunofluorescence images in Figure 38 show that SCNN1A protein is indeed increased on the apical side of cells treated with IL-17/TNF-α.

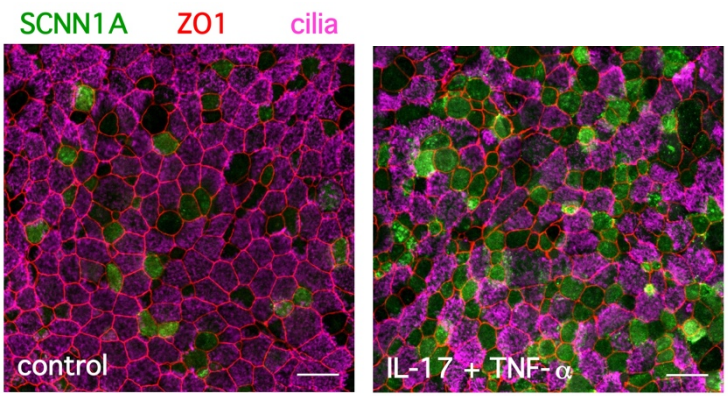

Figure 38. Detection of SCNN1A protein in bronchial epithelial cells. Representative confocal microscope images, from control- and IL-17/TNF-α–treated epithelia, in which SCNN1A, ZO-1, and cilia were detected by immunofluorescence. Scale bar: 25 μm. Adapted from Guidone et al., 2022.

Internalization and degradation of ENaC is blocked by SGK1-dependent phosphorylation (Debonneville et al., 2001), which prevents ENaC ubiquitination by NEDD4L. Since SGK1 was one of the genes upregulated by IL-17/TNF-α (Figure 30), we used a SGK1 inhibitor to assess the effect on ENaC activity (Figure 39, top). GSK650394 caused a rapid rundown of ENaC currents. The rundown was not significantly different between control- and IL-17/TNF-α–treated CF epithelia and only modestly different in non-CF epithelia. Furthermore, elastase was ineffective when added during the GSK650394-induced current rundown (Figure 39, bottom), indicating that the inhibitor is acting downstream the proteolytic step.

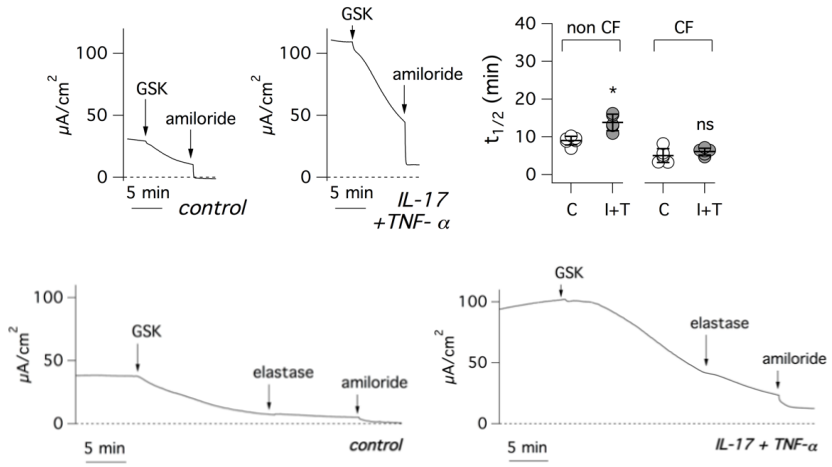

Figure 39. ENaC current rundown induced by SGK1 inhibition. Top: representative short-circuit current traces (left) and summary of data (right) for experiments where control- and IL-17/TNF-α–treated epithelia were apically exposed to 25 μM GSK650394 before amiloride. The scatter dot plot reports the $t_{1/2}$ values for each condition, *, $p < 0.05$ versus control (Student's t test). Bottom: the figure shows representative short-circuit current recordings from cultured bronchial epithelia treated in control conditions or with IL-17/TNF-α, in which the addition of elastase in epithelia treated with GSK650394 is ineffective. Adapted from Guidone et al., 2022.

We also inhibited mTORC2, since this regulatory complex acts upstream from SGK1 to control ENaC function (Lu et al., 2010, Gleason et al., 2015). The mTORC2 inhibitor PP242 also caused ENaC rundown, and the kinetics between control- and cytokine-treated epithelia were not significantly different (Figure 40). These results support SGK1 upregulation as the mechanism responsible for the enhanced ENaC function in epithelia exposed to IL-17/TNF-α. Indeed, SGK1 inhibition cancels the difference between control and treated epithelia.

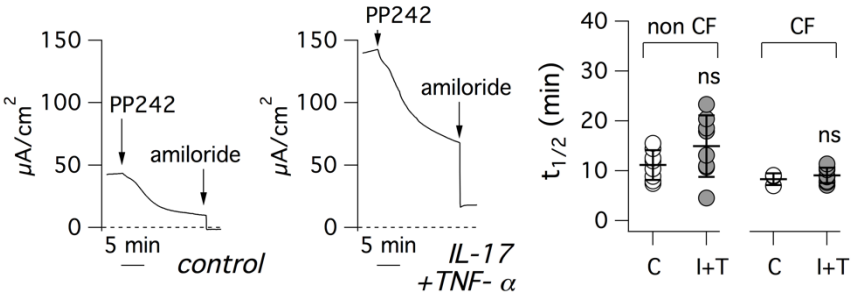

Figure 40. ENaC current rundown induced by mTORC2 inhibition. Representatives short-circuit current traces and summary of data for experiments where control- and IL-17/TNF-α–treated epithelia were apically exposed to 5 μM PP242 before amiloride. The scatter dot plots report the $t_{1/2}$ values for each condition (ns = not significant). Adapted from Guidone et al., 2022.

3.7 Effect of β-adrenergic stimulus on transepithelial ion transport

We were also interested in investigating the consequences of ADRB2 transcript upregulation by IL-17/TNF-α (Figure 30). ADRB2 activation results in intracellular cAMP elevation, which should, in turn, activate CFTR. We carried out short-circuit current recordings, during which the ADRB2 agonist isoproterenol was added on the basolateral side of epithelia. Addition of 10 and 100 nM of isoproterenol elicited rapid activation of currents that could be similarly blocked by $CFTR_{inh}$-172 and by the ADRB2 antagonist propranolol (Figure 41). Epithelia treated with IL-17/TNF-α showed a more than two-fold increase in isoproterenol-induced currents.

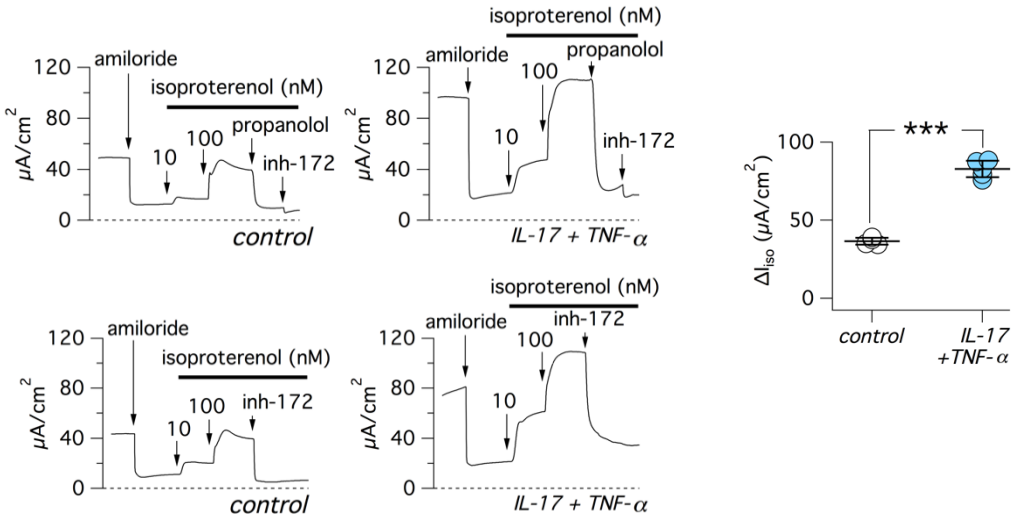

Figure 41. Effect of β-adrenergic stimulus on short circuit current recordings. Representative traces (left) and summary of data (right) for short-circuit current experiments on epithelia treated with/without IL-17/TNF-α, in which isoproterenol (10 and 100 nM) was added to stimulate CFTR activity. Where indicated $CFTR_{inh}$-172 (20 μM) and propranolol (5 μM) were also added. The scatter dot plot shows the amplitude of $CFTR_{inh}$-172 effect in epithelia previously stimulated with isoproterenol. ***, $p < 0.001$ versus control (Student's t test). Adapted from Guidone et al., 2022.

3.8 Alteration of Micro Particle Transport (MPT) by IL-17/TNF-α

Given the alteration by IL-17/TNF-α of multiple mechanisms involved in controlling airway surface chemical/physical properties and MCC (ENaC-dependent Na^+ absorption, CFTR-dependent anion secretion, ATP12A-dependent proton secretion), we carried out a series of functional assays to define the overall effect. First, we evaluated the transport of microbeads on the apical surface. Black microbeads dispersed in a small volume of saline solution were deposited on epithelial surface, and MCC was determined by time-lapse microscopy. Under control conditions, microbeads visibly moved with a velocity of approximately 10 μm/second in both CF and non-CF epithelia (Figure 42). Instead, epithelia treated for 72 hours with IL-17/TNF-α showed a near arrest of microbead transport. Importantly, muco-ciliary transport was resumed when non-CF epithelia treated with the cytokine combination were stimulated for 3 hours with basolateral isoproterenol. In contrast, despite the addition of the β-adrenergic agonist, microbeads remained static in CF epithelia (Figure 42).

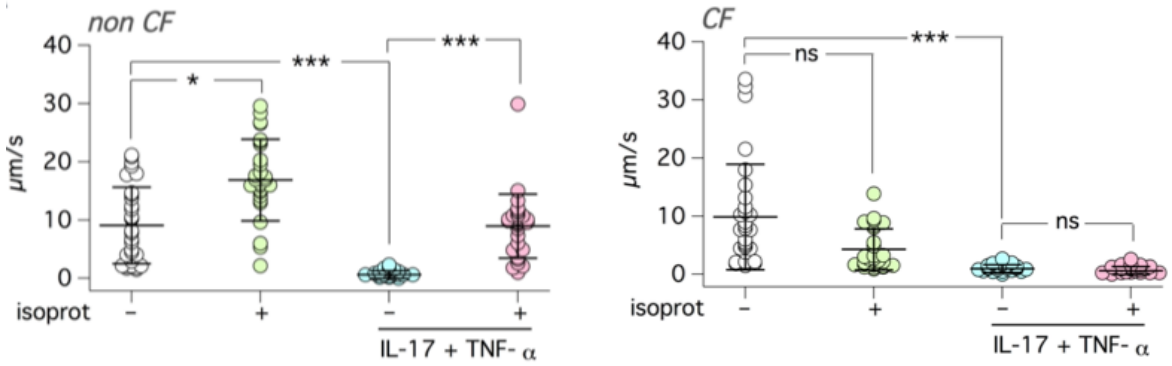

Figure 42. Analysis of mucociliary transport by video microscopy. The graphs report the velocity of microbeads on non-CF (left) and CF (right) cultured bronchial epithelia. Epithelia were treated for 72 h with/without IL-17/TNF-α and then stimulated for 3 h with isoproterenol or vehicle (100 nM). *, $p < 0.05$; **, $p < 0.01$; ***, $p < 0.001$; ns, not significant (Kruskal-Wallis and Dunn's test). Adapted from Guidone et al., 2022.

3.9 Alteration of airway surface viscosity by IL-17/TNF-α

To clarify the reason for the arrest of microbead transport, we investigated the properties of the apical surface with the FRAP technique. To apply FRAP, we needed a short distance between the objective and the epithelium, which was impeded by the narrow cup-like shape of the porous support (Snapwell) used to generate the epithelia. To overcome this limitation, we seeded epithelial cells on the opposite side of the porous membrane. To obtain the ALI condition, the medium was removed from the bottom part. Control short circuit recordings showed that, under this upside-down configuration, cells are still able to form tight epithelia with normal ion transport properties.

We added FITC-dextran dissolved in a small volume (5 μL) of saline solution and waited for 3 hours. Representative images in Figure 43, show that photobleaching was followed by a fast recovery in CF and non-CF epithelia kept under untreated conditions. After 72 hours of treatment with IL-17/TNF-α, we observed a dramatic slowing down of fluorescence recovery. In most cases, there was nearly no recovery at all. Importantly, when we added isoproterenol to the basolateral (top) side, we observed in non-CF epithelia a significant restoration of fluorescence recovery (Figure 43). In contrast, CF epithelia did not respond to isoproterenol (Figure 43).

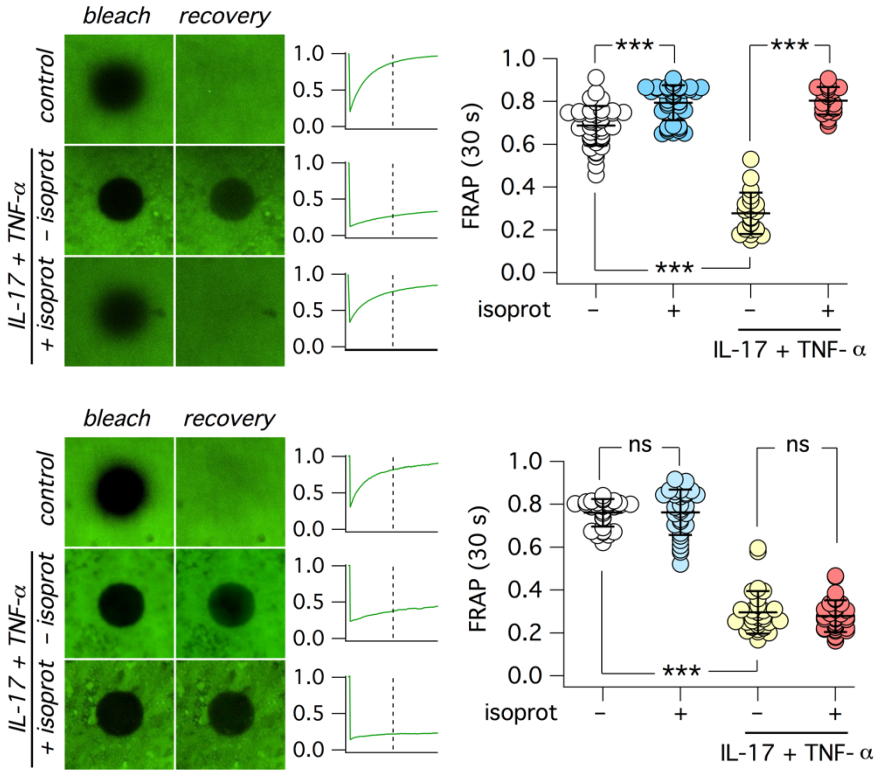

Figure 43. Effect of IL-17 + TNF-α and β-adrenergic stimulus on airway surface properties. Data from FRAP experiments on non-CF (top) or CF (bottom) epithelia treated with/without IL-17/TNF-α (72 hours). Where indicated, isoproterenol (100 nM) was added for 3 hours on the basolateral side before experiments. Representative images (left) show the epithelial surface, labeled with FITC-dextran, after photobleaching of a circular area and then after a 60-second recovery time. The traces on the side of each image pair report the time course of fluorescence recovery. The vertical dashed line indicates the 30-second time point. Scatter dot plots (right) show the normalized fluorescence value measured at 30 seconds after photobleaching. ***, $p < 0.001$ (Kruskal-Wallis and Dunn's test). Adapted from Guidone et al., 2022.

3.10 Effect of IL-17/TNF-α and β-adrenergic stimulus on apical pH

We investigated the effect of IL-17/TNF-α and isoproterenol on apical pH level using conditions that included HCO_3^-. In one set of experiments, we added a fixed volume (200 µL) of saline solution to the apical side of epithelia (large volume ex situ pH assay, see Materials and Methods

2.7.2). We also added mineral oil to minimize exchange of CO_2 between the solution and the atmosphere. After 6 hours, the aqueous apical solution was recovered to measure pH with SNARF-1 dextran conjugate. We found that the solution was essentially acidic, with a pH value close to 6.3 in both CF and non-CF epithelia (Figure 44). The pH only slightly changed by IL-17/TNF-α treatment. However, in agreement with ATP12A upregulation, epithelia treated with the cytokine combination showed a large alkalinization (approximately 0.9–1.0 pH units) when exposed to ouabain (Figure 44). Epithelia treated with IL-17/TNF-α also responded to the SLC26A4 inhibitor PDS_{inh}-A01 (Haggie et al., 2016), with a small (approximately 0.2–0.3 pH units) but significant acidic shift in pH (Figure 44). These results indicate that both ATP12A and SLC26A4 are involved in setting the apical pH, possibly with a larger contribution by ATP12A. Surprisingly, stimulation of epithelia with isoproterenol elicited a significant alkalinization (approximately 0.6 pH units) in both CF and non-CF epithelia previously treated with IL-17/TNF-α (Figure 44). The alkalinization by isoproterenol was significantly reduced by PDS_{inh}-A01 in CF epithelia and showed no additivity with ouabain (Figure 44).

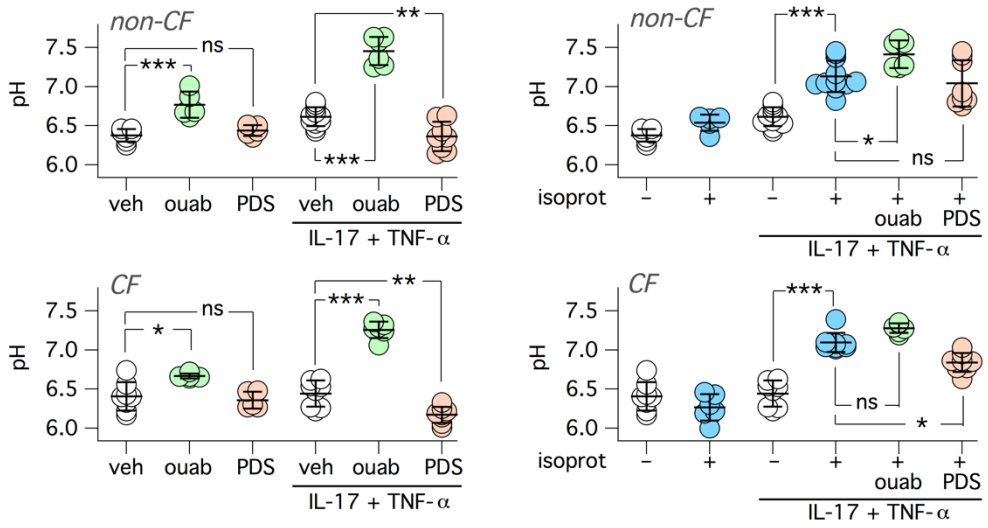

Figure 44. Effect of IL-17 + TNF-α and β-adrenergic stimulus on apical pH. Measurement of pH in the apical solution (large volume ex situ pH assay) for non-CF (top) and CF (bottom) epithelia, treated with/without IL-17/TNF-α. Where indicated, the apical solution contained ouabain (ouab, 200 μM) or PDS_{inh}-A01 (PDS, 25 μM), whereas the basolateral solution included isoproterenol (100 nM). *, $p < 0.5$; **, $p < 0.01$; ***, $p < 0.001$ (ANOVA with Tukey's post hoc test). Adapted from Guidone et al., 2022.

We tested YS-01 as a second type of SLC26A4 inhibitor (Lee et al., 2020). We compared side-by-side PDS_{inh}-A01 and YS-01 on SLC26A4 transport with a functional assay in FRT cells (Figure 45). Both compounds were effective, although YS-01 appeared more potent, with near total SLC26A4 inhibition at 5 µM (Figure 45).

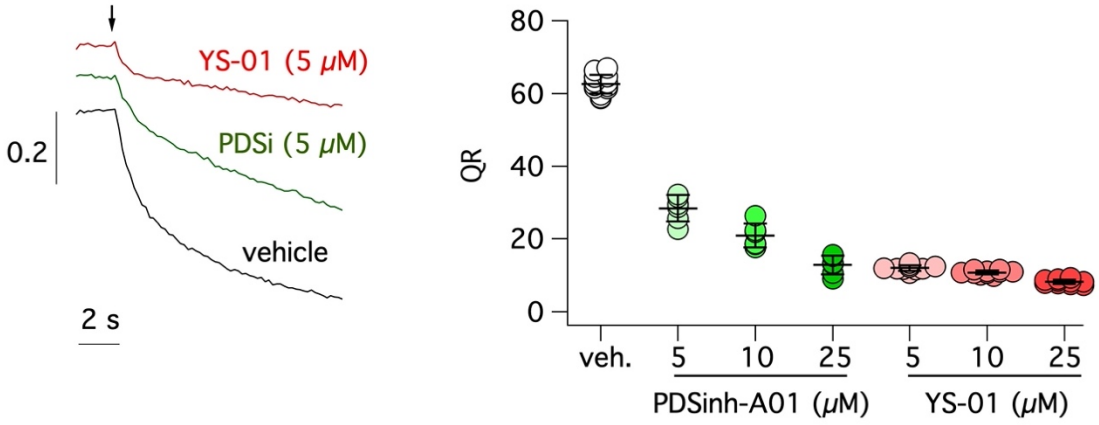

Figure 45. Evaluation of SLC26A4 inhibitors. Left: representative traces showing quenching of halide-sensitive yellow fluorescent protein (HS-YFP) caused by extracellular addition of I^- (arrow) in FRT cells expressing SLC26A4. SLC26A4 inhibitors (YS-01; PDSinh-A01, PDSi) slow down I^- uptake and hence HS-YFP quenching. Right: summary of data showing quenching rate (QR) of HS-YFP with vehicle and SLC26A4 inhibitors at the indicated concentrations. Adapted from Guidone et al., 2022.

We tested the effect of YS-01 on the apical pH of epithelia treated with IL-17/TNF-α (Figure 46). YS-01 generated a significant acidic shift in both CF and non-CF epithelia. A similar effect was also seen in CF but not in non-CF epithelia after stimulation with isoproterenol.

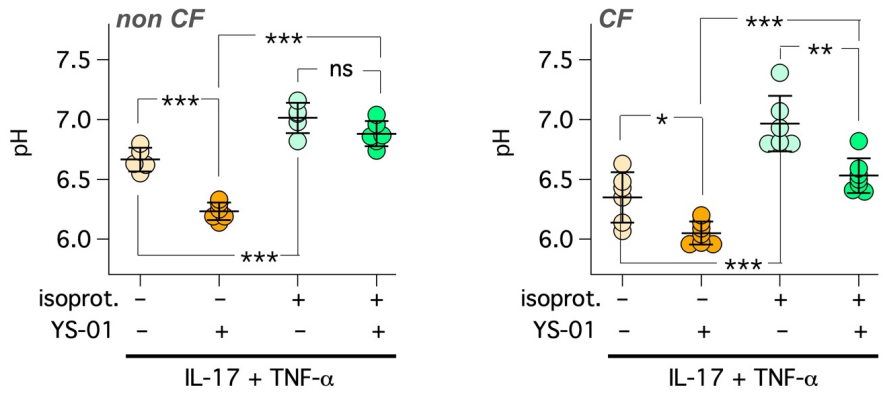

Figure 46. Contribution of pendrin to apical pH in bronchial epithelial cells. Apical pH measured with the large volume ex situ assay in non-CF and CF cultured bronchial epithelia treated for 72 h with the IL-17/TNF-α combination. Where indicated, in the last 3 h, epithelia were stimulated with/without isoproterenol (100 nM) in the absence/presence of YS-01 (5 μM). *, $p < 0.05$; **, $p < 0.01$; ***, $p < 0.001$; ns, not significant (ANOVA with Tukey's post hoc test). Adapted from Guidone et al., 2022.

We asked whether the alkalinization by isoproterenol is due to SLC26A4 upregulation or ATP12A inhibition. We reasoned that, if isoproterenol increases the activity of SLC26A4, we should have seen a significant change in pH in the presence of ouabain. However, this was not the case, since the pH values with ouabain plus/minus isoproterenol were essentially identical (Figure 47).

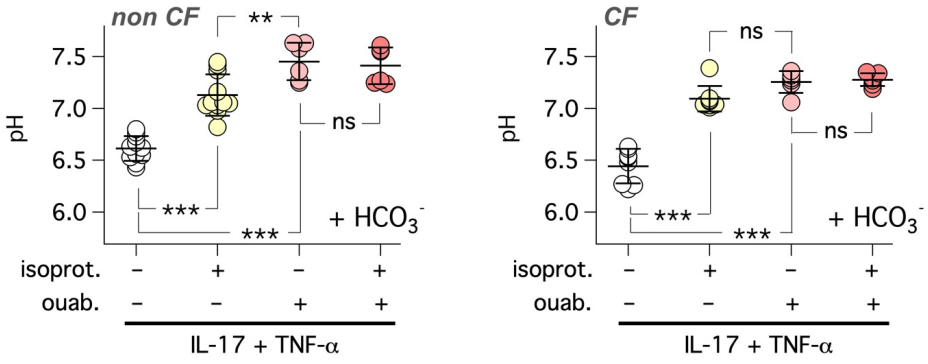

Figure 47. Analysis of isoproterenol effect on apical pH in HCO_3^--rich condition. The graphs report the apical pH (large volume ex situ assay) measured in non-CF (left) and CF (right) bronchial epithelia kept in HCO_3^--rich basolateral media. All epithelia were treated for 72 h with IL-17/TNF-α. Where indicated, epithelia were stimulated with basolateral isoproterenol (100 nM) in the absence/presence of ouabain (200 μM). **, $p < 0.01$; ***, $p < 0.001$; ns, not significant (ANOVA with Tukey's post hoc test). Adapted from Guidone et al., 2022.

Furthermore, isoproterenol also caused a significant alkalinization under HCO_3^--free conditions, which excludes SLC26A4 contribution (Figure 48). Such results indicate that the effect of isoproterenol on pH is due to inhibition of ATP12A.

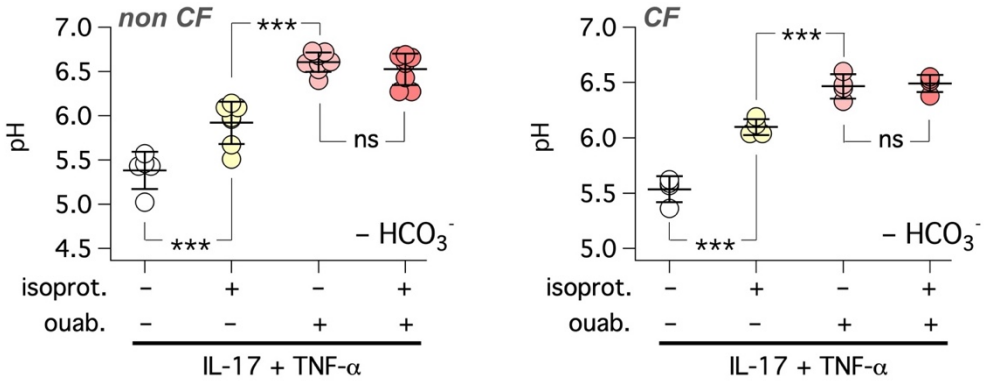

Figure 48. Analysis of isoproterenol effect on apical pH in HCO_3^--free condition. The graphs report the apical pH (large volume ex situ assay) measured in non-CF (left) and CF (right) bronchial epithelia kept in HCO_3^--free basolateral media. All epithelia were treated for 72 h with IL-17/TNF-α. Where indicated, epithelia were stimulated with basolateral isoproterenol (100 nM) in the absence/presence of ouabain (200 μM). ***, $p < 0.001$; ns, not significant (ANOVA with Tukey's post hoc test). Adapted from Guidone et al., 2022.

In a second set of experiments, to measure apical pH in a more physiological context, we "stained" the apical surface with a small volume (5 μL) of saline solution containing SNARF-1 dextran (small volume in situ pH assay, see Materials and Methods 2.7.3). With this technique, we could confirm that isoproterenol caused significant alkalinization of the apical surface in CF and non-CF epithelia (Figure 49, top). While carrying out these experiments, we noticed a peculiar behavior of SNARF-1 dextran whose distribution, as a colored pattern, could be easily detected by the naked eye and with a low magnification stereomicroscope. In epithelia kept under control conditions, the probe appeared to diffuse on a large area of the epithelium (Figure 49, bottom). In epithelia treated with IL-17/TNF-α, the probe remained confined in a smaller circular area characterized by very sharp borders. In non-CF epithelia, stimulation with isoproterenol reversed this situation, allowing rapid diffusion of the probe over the epithelium. In CF epithelia, isoproterenol was ineffective.

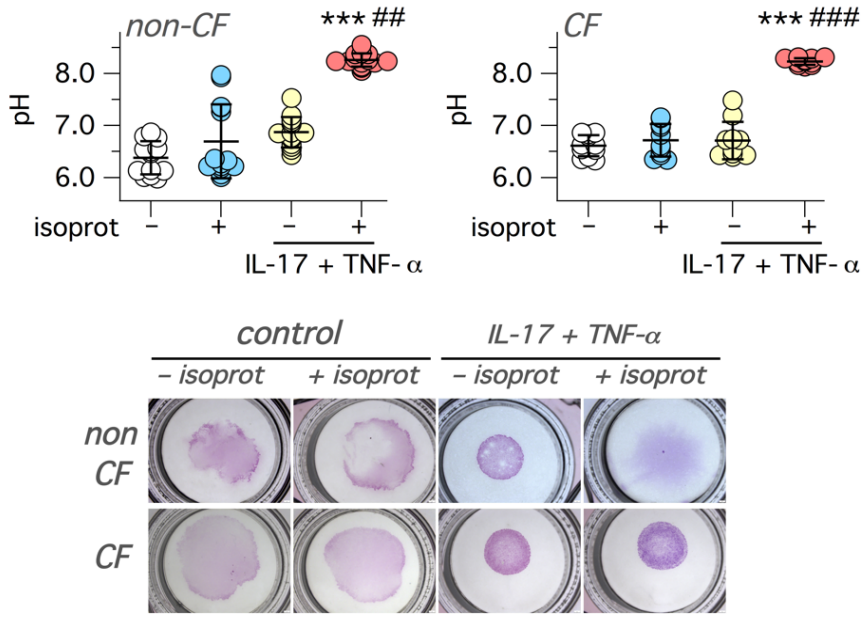

Figure 49. ASL pH measurement in small volume by SNARF-1 staining. Top: measurement of pH on the apical surface (small volume in situ pH assay) in non-CF (left) and CF (right) epithelia treated with/without IL-17/TNF-α (72 hours). Where indicated, the basolateral solution included isoproterenol (100 nM, for 3 hours before experiment). The scatter dot plots show pH values for the indicated conditions. ***, $p < 0.001$ versus untreated cells (no cytokine treatment, no isoproterenol). ##, $p < 0.01$; ###, $p < 0.001$ versus cells with cytokine treatment/without isoproterenol (Kruskal-Wallis and Dunn's test). Bottom: the images show the pattern of SNARF-1 dextran distribution on epithelial surface for the indicated conditions. Adapted from Guidone et al., 2022.

3.11 Consequence of bicarbonate transport and pendrin activity on airway surface viscosity

We asked how HCO_3^- transport affects the properties of airway surface in epithelia treated with IL-17/TNF-α. Therefore, we carried out, in parallel, FRAP experiments in the presence and absence of HCO_3^- in the basolateral medium, with 5% CO_2 and pure air in the atmosphere, respectively. Surprisingly, the apical surface of epithelia treated with the cytokine combination remained fluid under HCO_3^--free conditions, whereas epithelia in the presence of HCO_3^- developed the expected viscous state (Figure 50).

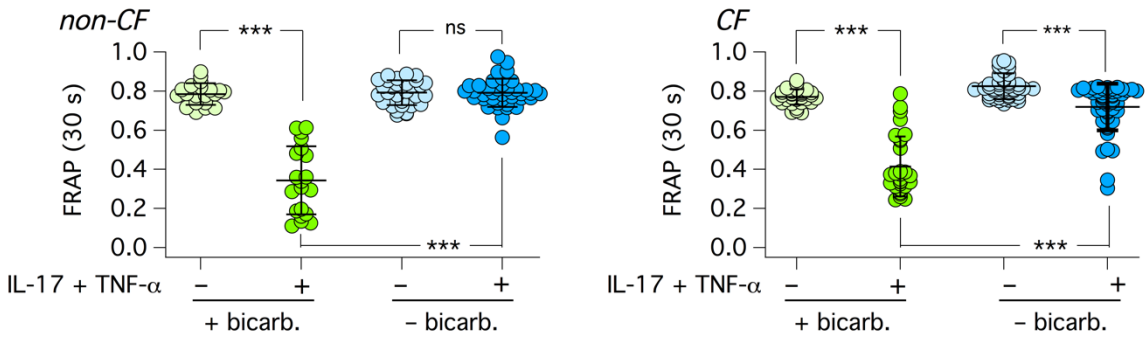

Figure 50. Effect of HCO_3^- transport on airway surface properties. The graphs show the results of FRAP experiments on bronchial epithelia that were pretreated for 72 hours with/without IL-17/TNF-α. Data were obtained in non-CF (left) and CF (right) bronchial epithelia with HCO_3^- or Hepes buffered media on the basolateral side for 3 hours before measurements. ***, $p < 0.001$; ns = not significant (Kruskal-Wallis and Dunn's test). Adapted from Guidone et al., 2022.

We also carried out experiments with YS-01 to block SLC26A4 function. YS-01 decreased viscosity in both non-CF and CF epithelia treated with IL-17/TNF-α, indicating that SLC26A4 has an important role in establishing the viscous state by the cytokine combination (Figure 51).

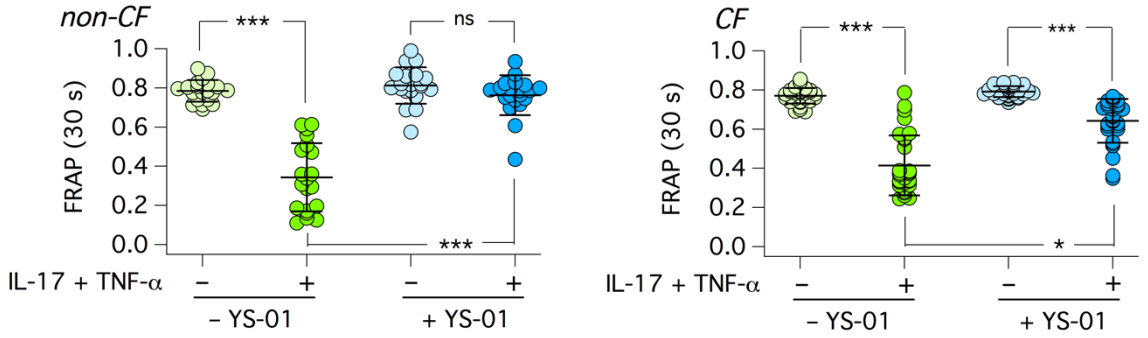

Figure 51. Effect of pendrin inhibition on airway surface properties. The graphs show the results of FRAP experiments on bronchial epithelia that were pretreated for 72 hours with/without IL-17/TNF-α. Data from experiments in non-CF (left) and CF (right) bronchial epithelia with YS-01 (5 μM) added to the basolateral side for 3 hours before measurements. *, $p < 0.05$; ***, $p < 0.001$; ns = not significant (Kruskal-Wallis and Dunn's test). Adapted from Guidone et al., 2022.

3.12 Effect of CFTR rescue with correctors on apical viscosity

Finally, we asked whether mutant CFTR rescue in CF epithelia with pharmacological correctors of F508del mutation (Elborn, 2016) is effective in decreasing apical viscosity. We treated epithelia for 72 hours with/without IL-17/TNF-α. In the last 24 hours, epithelia were treated with the corrector combination VX-809/VX-445 or with vehicle. Then, all epithelia were stimulated with isoproterenol. CF epithelia treated with IL-17/TNF-α and vehicle showed the expected slow fluorescence recovery. However, epithelia that were pretreated with correctors showed a significant improvement in airway surface properties, as indicated by faster fluorescence recovery (Figure 52).

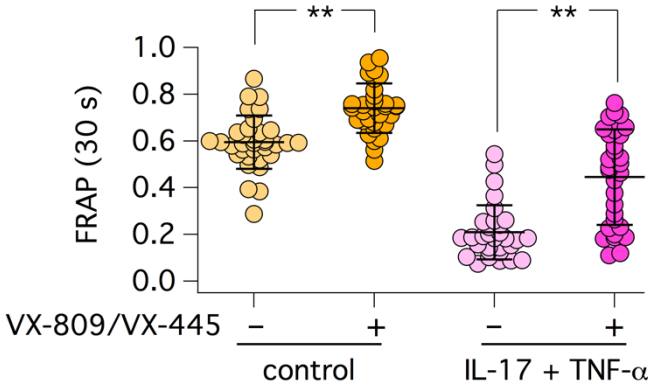

Figure 52. Effect of CFTR rescue on airway surface properties. The graphs show the results of FRAP experiments on F508del/F508del CF bronchial epithelia that were pretreated for 72 hours with/without IL-17/TNF-α. Where indicated, epithelia were treated with the VX-809 (1 μM) plus VX-445 (5 μM) or vehicle in the last 24 hours before measurements. All epithelia were stimulated with isoproterenol (100 nM, basolateral) for 3 hours. **, $p < 0.01$ (Kruskal-Wallis and Dunn's test). Adapted from Guidone et al., 2022.

4. DISCUSSION

4.1 ATP12A upregulation is linked to pro-inflammatory stimuli and is particularly increased by IL-17+TNF-α

In a previous work from our group (Scudieri et al., 2018), we investigated ATP12A expression in human bronchi from CF and non-CF patients, and found that is upregulated in CF. We wondered if this upregulation is directly due to CFTR basic defect or to infection and inflammation that occur in end-stage disease. A first suggestion that ATP12A overexpression is linked to inflammation derives from data obtained in cultured bronchial epithelial cells under sterile conditions, in which ATP12A expression does not differ between CF and non-CF. Furthermore, treatment with bacterial supernatant or IL-4 strongly upregulates ATP12A (Scudieri et al., 2018). Therefore, our starting hypothesis was that ATP12A expression could be modulated by different types of pro-inflammatory stimuli and that its upregulation in CF is due to inflammation rather than to the absence of CFTR itself.

First, we decided to investigate ATP12A expression in nasal brushings. The low-invasive procedure of nasal brushing allowed us to obtain a high variety of samples with respect to bronchi from transplanted patients and to analyze the nasal mucosa of subjects with different clinical conditions and age. The comparison between CF and non-CF individuals confirmed ATP12A upregulation in CF as it occurs in bronchi. In general, we found a broad range of ATP12A expression that could be explained with different levels of nasal mucosa inflammation at the time of cell collection. ATP12A signal results more intense also in non-CF samples with rhinitis. The absence of correlation between ATP12A-positive cells and FEV1 suggests that ATP12A upregulation does not depend on pulmonary function. Moreover, there is no correlation between ATP12A-positive cells and age, since some very young patients in an early-stage of CF disease show high ATP12A level. An intriguing finding is the aberrant localization of ATP12A signal in ciliated cells, since normally it is present on the apical membrane of mucus-producing cells (Gorrieri et al., 2016). It has been reported that expression of ATP12A in ciliated cells is an early sign of transdifferentiation of ciliated cells to goblet cells (Vieira-Braga et al., 2019). We plotted ATP12A expression in ciliated cells versus the global cell population and we found a positive

correlation. Therefore, expression of ATP12A in ciliated cells of CF patients could be associated with goblet cell hyperplasia and airway inflammation.

Given the results obtained in nasal brushings, we decided to test various types of stimuli in vitro in order to mimic the inflammation occurring in CF airways. Recently, CF disease has been associated with Th17 inflammation rather than to Th2 immune response, that resembles more allergic and asthma conditions (Lambrecht et al., 2019; Hagner et al., 2021). We found that the combination of IL-17+TNF-α was particularly effective in enhancing ATP12A expression. To correlate ATP12A expression and function, we performed pH measurements in the apical compartment under HCO_3^- -free conditions. The results confirmed ATP12A upregulation also at the functional level, as indicated by strong enhancement of the ouabain-sensitive component. It has been shown that airway epithelia, particularly of distal bronchi, display proton secretion mediated by the electrogenic V-ATPase (Li et al., 2021). This activity could be dependent on CFTR that, by transporting Cl^-, provides the counter ion required for electroneutrality. In agreement with this notion, we found that a bafilomycin-sensitive component was present in non-CF but not in CF epithelia. This finding probably explains why pH was actually more acidic in non-CF epithelia under resting conditions. Interestingly, the bafilomycin-sensitive proton secretion disappeared in non-CF epithelia after treatment with IL-17/TNF-α.

4.2 IL-17 plus TNF-α treatment elicits profound gene expression changes in bronchial epithelial cells

We determined the changes in gene expression profile elicited by IL-17/TNF-α cytokines by bulk mRNA sequencing and scRNAseq. This analysis revealed a broad transcriptional response of pathways involved in cytokines and chemokines signaling, TLR signaling pathway, modulation of immune response and antimicrobial activity. However, IL-17/TNF-α also modulates genes with high relevance in transepithelial ion transport and innate defense function, such as ADRB2, SGK1, SCNN1A, SCNN1B, MUC5B, SLC26A4, and ATP12A.

By scRNAseq, these genes are mapped in the same cell cluster (cluster 1) that appears in the population of cells stimulated with cytokine combination. We interpret this as the activation of a

specific transcriptional program that may affect epithelial surface properties. The specificity of this gene expression profile was also pointed out by the comparison with IL-4 treatment, that differs in the types of genes induced (e.g., MUC5AC, ANO1).

4.3 IL-17 plus TNF-α cytokine combination increases ENaC- and CFTR-dependent ion transport activity

To evaluate the overall effect of IL-17/ TNF-α on electrogenic ion transport we carried out short-circuit current recordings. Surprisingly, IL-17/TNF-α treatment increased ENaC-dependent Na^+ absorption and CFTR-dependent Cl^- secretion. TMEM16A-dependent Cl^- secretion was not altered, in agreement with gene expression profile. Moreover, the epithelia treated with IL-17/TNF-α showed a residual current that we identified as the Na^+-dependent glucose uptake by SLC5A1. Indeed, this transporter was upregulated by transcriptome analysis and the current we noticed during the recordings resulted sensitive to SLC5A1 inhibitor mizaglifozin. The upregulation of SLC5A1 is particularly interesting, since it could be an anti-bacterial defense mechanism through which the epithelium depletes the surface of glucose as potential nutrient for bacteria.

To our knowledge, it was the first time in which ENaC upregulation by pro-inflammatory cytokines is reported, since other inflammatory stimuli decrease ENaC activity (Danahay et al., 2002; Galietta et al., 2002; Gray et al., 2004). Since the transcriptomic upregulation of SCNN1A and SCNN1B by IL-17/TNF-α was relatively modest, we considered a post-transcriptional mechanism to explain ENaC upregulation.

ENaC function is tightly regulated by a complex process involving trafficking to the plasma membrane, channel activation by proteolysis, and fast internalization/degradation by a ubiquitin-dependent mechanism (Gaillard et al., 2010; Rossier & Stutts, 2009; de la Rosa et al., 2002; Kabra et al., 2008; Knight et al., 2006; Rotin & Staub, 2021). ENaC ubiquitination and internalization is prevented by SGK1-dependent phosphorylation (Debonneville et al., 2001). During short-circuit current recordings, the lack of elastase effect on both control and IL-17/TNF-α suggests that ENaC is fully cleaved in both conditions, excluding an enhanced proteolytic activation of ENaC by the

cytokine treatment. To further investigate the basis of ENaC upregulation we used camostat as a protease inhibitor that prevents ENaC activation. Camostat allowed us to follow the internalization process of the channels cleaved before camostat addition. Addition of camostat during short-circuit current recordings induced a fast rundown of ENaC-dependent currents in control-treated epithelia. Importantly, ENaC function rundown was significantly slower in epithelia treated with IL-17/TNF-α. This finding indicates that ENaC upregulation elicited by the cytokine treatment may depend on a slower rate of internalization. In this respect, one of the genes induced by IL-17/TNF-α is SGK1. To test SGK1 involvement, we used GSK650394 as a SGK1 inhibitor. This compound elicited a rapid rundown of ENaC currents. Furthermore, it is reported that mTORC2 complex regulates ENaC through SGK1 (Lu et al., 2010; Gleason et al., 2015). Inhibition of mTORC2 by PP242 compound also caused rundown of ENaC currents. Such results suggest that SGK1 upregulation may be responsible, at least in part, for the higher ENaC function in epithelia treated with IL-17/TNF-α. The enhancement of ENaC function by IL-17/TNF-α is expected to worsen the impairment of MCC caused in CF by CFTR loss of function. Enhanced activity of ENaC in CF airways, with the consequent hyperabsorption of Na^+ and fluid, has been a debated topic (Boucher et al., 1988; Nagel et al., 2001; Collawn et al., 2012; Itani et al., 2011; Mall et al., 1998). Our findings reveal a mechanism to explain ENaC upregulation in CF, not directly linked to CFTR defect but to the associated inflammation and provide a further rationale for the use of ENaC inhibitors to treat CF patients (Shei et al., 2018).

We further investigated the increase in CFTR current in bronchial epithelia treated with IL-17/TNF-α. In particular, we focused on the transcriptomic data that revealed an upregulation of ADRB2, a receptor that when stimulated causes an intracellular cAMP increase. Therefore, we directly stimulated ADRB2 to check whether it led to CFTR activation. Accordingly, during current recordings, we applied the β-adrenergic agonist isoproterenol. Isoproterenol elicited a current that: i) was larger with IL-17/TNF-α respect to control condition; ii) was totally blocked by the β-adrenergic antagonist propranolol; iii) was blocked by $CFTR_{inh}$-172. This confirms that in IL-17/TNF-α-treated epithelia the upregulation of β-adrenergic receptor is a mechanism that leads to an increase in CFTR activity. However, since the application of cAMP analogue (CPT-cAMP) also shows a higher CFTR current in IL-17/TNF-α epithelia, we cannot exclude mechanism directly involving CFTR upregulation, as reported by other studies (Rehman et al., 2021).

4.4 IL-17/TNF-α induces an hyperviscous state of ASL that is turned off, only in non-CF epithelia, by β-adrenergic stimulation

We asked how the upregulation of different channels and transporters (ENaC, CFTR, pendrin, and ATP12A) by IL-17/TNF-α affects the properties of the airway surface. Measurements of mucociliary transport by MPT revealed a profound inhibition induced by the cytokine treatment. Importantly, mucociliary transport was restored only in non-CF epithelia stimulated with a β-adrenergic agonist, while in CF the microbeads remain nearly immobile. Such changes were in agreement with the properties of the apical surface measured with the FRAP technique. Indeed, the diffusion of the high–molecular weight fluorescent dextran was nearly abolished in epithelia treated with IL-17/TNF-α, but it was recovered, only in non-CF epithelia, by isoproterenol stimulation. Such results suggest that impairment of mucociliary transport in epithelia treated with the cytokine combination is caused by hyperviscosity and dehydration of airway surface. This condition could result from the combination of enhanced Na^+ absorption and apical surface acidification due to ENaC and ATP12A upregulation, respectively. In this regard, it should be noted that ATP12A upregulation by IL-13 was previously found to be associated with airway surface hyperviscosity (Lennox et al., 2018). The evidence that β-adrenergic stimulation through isoproterenol resumes ASL hydration and mucociliary transport only in non-CF highlights the central role of CFTR in this process.

To further inspect the modulation of ASL properties by cytokine treatment, we measured pH in presence of HCO_3^- to assess the role of ATP12A and SLC26A4. In agreement with ATP12A and SLC26A4 upregulation, epithelia treated with IL-17/TNF-α showed alkalinization and acidification with ouabain and SLC26A4 inhibitors (PDS_{inh}-A01 and YS-01), respectively. These results indicate that both transporters contribute to setting apical pH. Interestingly, isoproterenol caused a marked alkalinization, which is of similar amplitude in both CF and non-CF epithelia and which, in part, resembled that produced by ouabain. The effect of isoproterenol was further confirmed by the low-volume pH assay, in which we measured pH in a more physiological context by minimally altering ASL. Since this alkalinization by isoproterenol is present in both CF and non-CF, we can exclude that it was CFTR-dependent and reasoned that could either be caused by SLC26A4 activation or ATP12A inhibition. To test the first hypothesis, we measured pH in HCO_3^--rich medium and in presence of ouabain to block ATP12A activity. We considered that, in

presence of ouabain, the pH values plus/minus isoproterenol should differ if isoproterenol activates pendrin, but this was not the case. To test the second hypothesis, we measured pH in HCO_3^--free condition. Isoproterenol caused a significant alkalinization also under HCO_3^--free conditions, which further excludes SLC26A4 contribution. Moreover, in this condition, the effects of isoproterenol and ouabain on pH were not additive. In conclusion, pH experiments suggest that the alkalinization by isoproterenol should derive from downregulation of ATP12A activity that would uncover SLC26A4-dependent HCO_3^- export. In this respect, we found that the SLC26A4 inhibitor indeed lowered pH in CF epithelia stimulated with isoproterenol. This effect was much lower in non-CF epithelia, possibly suggesting that another mechanism, perhaps CFTR, is contributing to HCO_3^- secretion when SLC26A4 is inhibited.

Taking together the results of pH and FRAP experiments, we found that isoproterenol elicits alkalinization of apical fluid also in CF epithelia, but it did not affect viscosity. Therefore, we conclude that the increase in pH is not able per se to make airway surface less viscous. In fact, the recovery of mucociliary transport elicited by isoproterenol only in non-CF epithelia implies that CFTR is endowed with a key function that controls the overall effect of cytokine treatment. The central role of CFTR was further highlighted by the results of FRAP experiments performed on epithelia from CF patients with F508del mutation, in which treatment with CFTR pharmacological correctors VX-809/VX-445 significantly improved ASL fluidity.
We asked if it is possible to improve ASL fluidity by acting on other targets besides CFTR, so we carried out FRAP experiments in the presence of the pendrin inhibitor YS-01. We found that pendrin inhibition restored apical fluidity, thus indicating that pendrin plays an important role in establishing the viscous state induced by cytokines combination.

4.5 Conclusions

Our experiments that were initially guided to understand the basis of ATP12A upregulation in CF airways have revealed that IL-17/TNF-α is a potent stimulus that, besides affecting ATP12A, modifies other processes with high relevance to airway epithelium barrier function. To summarize the overall output of the complex changes induced by IL-17/TNF-α combination, we propose the model depicted in Figure 53. It considers the coordinated activity of ENaC, ATP12A, SLC26A4

with a key role of CFTR and β-adrenergic stimulus in switching the epithelium between an absorptive and a secretory state. As found in the distal nephron, we propose that ENaC and SLC26A4 work in parallel to generate a net NaCl absorption (Patel-Chamberlin et al., 2016). Indeed, the absorption of Na^+ through ENaC is followed by the uptake of Cl^- mediated by SLC26A4. Then, it is expected that inhibition of pendrin stops NaCl/fluid absorption. In this respect, Haggie and colleagues demonstrated that inhibition of pendrin indeed results in decreased fluid absorption in airway epithelia (Haggie et al., 2016). Our FRAP experiments agrees with this study, indeed we found that pendrin inhibition improves apical fluidity. SLC26A4 activity implies also that HCO_3^- is released on the apical side. Excessive accumulation of HCO_3^-, which could reverse the direction of transported anions by SLC26A4, should be prevented to support NaCl absorption. The upregulation of ATP12A could be a way to neutralize extruded HCO_3^-. The combined secretion of H^+ and HCO_3^- by ATP12A and pendrin would push the production of CO_2 that leaves the apical surface to airway lumen. Furthermore, we cannot exclude that ATP12A H^+ pumping, by preventing excessive alkalinization, sustains ENaC activity that is favored by acidic pH (Garland et al., 2013).

In summary, the upregulation of ENaC, SLC26A4, and ATP12A by IL-17/TNF-α would be instrumental to promote NaCl/fluid absorption. In this respect, the presence of HCO_3^- appears to be crucial for fluid absorption, since in its absence, we found that the apical surface remains fluid despite the treatment with the cytokine combination. The requirement of HCO_3^- to generate the viscous state is unexpected and prompts reconsideration of the role of this anion in the homeostasis of airway surface properties.

Importantly, we found that the absorptive state induced by IL-17/TNF-α is turned off by the β-adrenergic stimulus. Isoproterenol decreased the viscosity of apical surface in non-CF epithelia treated with IL-17/TNF-α. The lack of effect of isoproterenol in CF epithelia highlights the key role of CFTR in this process. Also, we obtained results suggesting that the β-adrenergic stimulus inhibits ATP12A activity. To integrate these results, we postulate that isoproterenol switches the epithelium state from absorptive to secretory. Indeed, the opening of CFTR channel would allow Cl^- efflux (Figure 53). Therefore, Cl^- entering the cell by SLC26A4 would be recycled back to the apical surface. The net effect of CFTR and SLC26A4 working in parallel would be the enhanced secretion of HCO_3^-. We cannot exclude that part of HCO_3^- secretion is also directly mediated by CFTR. Coupled to ATP12A inhibition, this would result in accumulation of HCO_3^-. This is

expected to improve the fluidity of the apical surface and to promote antimicrobial activity (Hoegger et al., 2014; Garcia et al., 2009; Gustafsson et al., 2012; Pezzulo et al., 2012; Shah et al., 2016).

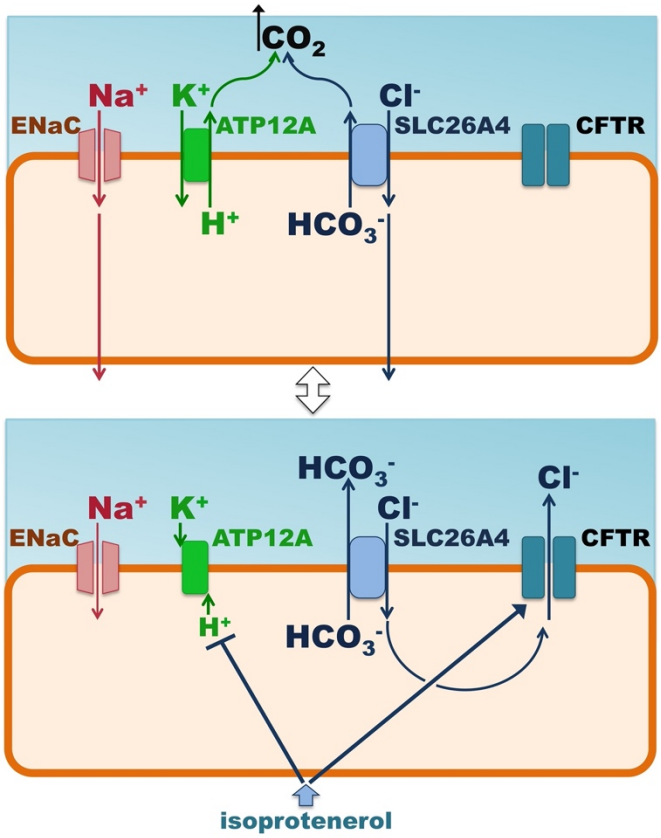

Figure 53. Graphical model of the switch from absorptive to secretory state induced by isoproterenol in IL-17/TNF-α treated cells. The illustration shows the proposed changes in ion transport that occur when epithelia treated with IL-17/TNF-α are stimulated with the β-adrenergic agonist. Adapted from Guidone et al., 2022.

To further support this model, additional evidence will need to be provided in future experiments. In particular, other pharmacological inhibitors of ATP12A, with improved selectivity with respect to ouabain, need to be found. Also, methods to measure local changes in HCO_3^- concentration will need to be developed. Moreover, alteration of airway surface properties may also involve changes in solid content and Ca^{2+} concentration, parameters that we did not evaluate in our study.

IL-17/TNF-α is associated with bacterial infection and neutrophilic infiltration (Rehman et al., 2020). The increased viscosity of the apical surface by IL-17/TNF-α treatment appears to be detrimental, since mucociliary transport is believed to be beneficial as an antibacterial defense mechanism. However, we speculate that transient and local immobilization of bacteria, which would result from increased viscosity, could be useful to avoid dispersion of bacteria over large surfaces and to promote killing by localized epithelium- and neutrophil-dependent mechanisms. In this respect, we found that IL-17/TNF-α enhances the expression of potential antimicrobial genes. When needed, the absorptive state induced by IL-17/TNF-α would be turned off by the β-adrenergic stimulus to restore mucociliary transport. This switch would be disrupted in CF airways, thus triggering a cycle of inflammation and mucociliary transport impairment. Importantly, our experiments with CFTR correctors show that rescue of F508del-CFTR function allows CF epithelia to acquire, at least in part, the low-viscosity state associated with β-adrenergic stimulus, potentially breaking the damaging cycle. It would be important to find out how the persistent hyperviscous state can be corrected in CF patients with undruggable CFTR mutations. Our results indicate that SLC26A4 inhibition could be an effective approach that could improve MCC in such patients. Our findings are also of high relevance to clarify the pathogenic mechanisms and to find possible therapeutic interventions for other, nongenetic, chronic obstructive respiratory diseases.

5. BIBLIOGRAPHY

Abou Alaiwa, M. H., Beer, A. M., Pezzulo, A. A., Launspach, J. L., Horan, R. A., Stoltz, D. A., Starner, T. D., Welsh, M. J., & Zabner, J. (2014). Neonates with cystic fibrosis have a reduced nasal liquid pH; a small pilot study. *Journal of cystic fibrosis : official journal of the European Cystic Fibrosis Society*, *13*(4), 373–377. https://doi.org/10.1016/j.jcf.2013.12.006

Adams, K. M., Abraham, V., Spielman, D., Kolls, J. K., Rubenstein, R. C., Conner, G. E., Cohen, N. A., & Kreindler, J. L. (2014). IL-17A induces Pendrin expression and chloride-bicarbonate exchange in human bronchial epithelial cells. *PloS one*, *9*(8), e103263. https://doi.org/10.1371/journal.pone.0103263

Ahmad, T., Ertuglu, L. A., Masenga, S. K., Kleyman, T. R., & Kirabo, A. (2023). The epithelial sodium channel in inflammation and blood pressure modulation. *Frontiers in cardiovascular medicine*, *10*, 1130148. https://doi.org/10.3389/fcvm.2023.1130148

Anagnostopoulou, P., Riederer, B., Duerr, J., Michel, S., Binia, A., Agrawal, R., Liu, X., Kalitzki, K., Xiao, F., Chen, M., Schatterny, J., Hartmann, D., Thum, T., Kabesch, M., Soleimani, M., Seidler, U., & Mall, M. A. (2012). SLC26A9-mediated chloride secretion prevents mucus obstruction in airway inflammation. *The Journal of clinical investigation*, *122*(10), 3629–3634. https://doi.org/10.1172/JCI60429

Anders, S., Pyl, P. T., & Huber, W. (2015). HTSeq--a Python framework to work with high-throughput sequencing data. *Bioinformatics (Oxford, England)*, *31*(2), 166–169. https://doi.org/10.1093/bioinformatics/btu638

Bakouh, N., Bienvenu, T., Thomas, A., Ehrenfeld, J., Liote, H., Roussel, D., Duquesnoy, P., Farman, N., Viel, M., Cherif-Zahar, B., Amselem, S., Taam, R. A., Edelman, A., Planelles, G., & Sermet-Gaudelus, I. (2013). Characterization of SLC26A9 in patients with CF-like lung disease. *Human mutation*, *34*(10), 1404–1414. https://doi.org/10.1002/humu.22382

Balázs, A., & Mall, M. A. (2018). Role of the SLC26A9 Chloride Channel as Disease Modifier and Potential Therapeutic Target in Cystic Fibrosis. *Frontiers in pharmacology*, *9*, 1112. https://doi.org/10.3389/fphar.2018.01112

Bals, R., & Hiemstra, P. S. (2004). Innate immunity in the lung: how epithelial cells fight against respiratory pathogens. *The European respiratory journal*, *23*(2), 327–333. https://doi.org/10.1183/09031936.03.00098803

Bartoszewski, R., Matalon, S., & Collawn, J. F. (2017). Ion channels of the lung and their role in disease pathogenesis. *American journal of physiology. Lung cellular and molecular physiology*, *313*(5), L859–L872. https://doi.org/10.1152/ajplung.00285.2017

Boers, J. E., den Brok, J. L., Koudstaal, J., Arends, J. W., & Thunnissen, F. B. (1996). Number and proliferation of neuroendocrine cells in normal human airway epithelium. *American journal of respiratory and critical care medicine*, *154*(3 Pt 1), 758–763. https://doi.org/10.1164/ajrccm.154.3.8810616

Boucher, R. C., Cotton, C. U., Gatzy, J. T., Knowles, M. R., & Yankaskas, J. R. (1988). Evidence for reduced Cl- and increased Na+ permeability in cystic fibrosis human primary cell cultures. *The Journal of physiology*, *405*, 77–103. https://doi.org/10.1113/jphysiol.1988.sp017322

Breton, S., & Brown, D. (2007). New insights into the regulation of V-ATPase-dependent proton secretion. *American journal of physiology. Renal physiology*, *292*(1), F1–F10. https://doi.org/10.1152/ajprenal.00340.2006

Bustamante-Marin, X. M., & Ostrowski, L. E. (2017). Cilia and Mucociliary Clearance. *Cold Spring Harbor perspectives in biology*, *9*(4), a028241. https://doi.org/10.1101/cshperspect.a028241

Button, B., Cai, L. H., Ehre, C., Kesimer, M., Hill, D. B., Sheehan, J. K., Boucher, R. C., & Rubinstein, M. (2012). A periciliary brush promotes the lung health by separating the mucus layer from airway epithelia. *Science (New York, N.Y.)*, *337*(6097), 937–941. https://doi.org/10.1126/science.1223012

Button, B., Okada, S. F., Frederick, C. B., Thelin, W. R., & Boucher, R. C. (2013). Mechanosensitive ATP release maintains proper mucus hydration of airways. *Science signaling*, *6*(279), ra46. https://doi.org/10.1126/scisignal.2003755

Caputo, A., Caci, E., Ferrera, L., Pedemonte, N., Barsanti, C., Sondo, E., Pfeffer, U., Ravazzolo, R., Zegarra-Moran, O., & Galietta, L. J. (2008). TMEM16A, a membrane protein associated with calcium-dependent chloride channel activity. *Science (New York, N.Y.)*, *322*(5901), 590–594. https://doi.org/10.1126/science.1163518

Chen, G., Sun, L., Kato, T., Okuda, K., Martino, M. B., Abzhanova, A., Lin, J. M., Gilmore, R. C., Batson, B. D., O'Neal, Y. K., Volmer, A. S., Dang, H., Deng, Y., Randell, S. H., Button, B., Livraghi-Butrico, A., Kesimer, M., Ribeiro, C. M., O'Neal, W. K., & Boucher, R. C. (2019). IL-1β dominates the promucin secretory cytokine profile in cystic fibrosis. *The Journal of clinical investigation*, *129*(10), 4433–4450. https://doi.org/10.1172/JCI125669

Collaco, A. M., Geibel, P., Lee, B. S., Geibel, J. P., & Ameen, N. A. (2013). Functional vacuolar ATPase (V-ATPase) proton pumps traffic to the enterocyte brush border membrane and require CFTR. *American journal of physiology. Cell physiology*, *305*(9), C981–C996. https://doi.org/10.1152/ajpcell.00067.2013

Collawn, J. F., Lazrak, A., Bebok, Z., & Matalon, S. (2012). The CFTR and ENaC debate: how important is ENaC in CF lung disease?. *American journal of physiology. Lung cellular and molecular physiology*, *302*(11), L1141–L1146. https://doi.org/10.1152/ajplung.00036.2012

Coote, K., Atherton-Watson, H. C., Sugar, R., Young, A., MacKenzie-Beevor, A., Gosling, M., Bhalay, G., Bloomfield, G., Dunstan, A., Bridges, R. J., Sabater, J. R., Abraham, W. M., Tully, D., Pacoma, R., Schumacher, A., Harris, J., & Danahay, H. (2009). Camostat attenuates airway epithelial sodium channel function in vivo through the inhibition of a channel-activating protease. *The Journal of pharmacology and experimental therapeutics*, *329*(2), 764–774. https://doi.org/10.1124/jpet.108.148155

Crambert G. (2014). H-K-ATPase type 2: relevance for renal physiology and beyond. *American journal of physiology. Renal physiology*, *306*(7), F693–F700. https://doi.org/10.1152/ajprenal.00605.2013

Crystal, R. G., Randell, S. H., Engelhardt, J. F., Voynow, J., & Sunday, M. E. (2008). Airway epithelial cells: current concepts and challenges. *Proceedings of the American Thoracic Society*, *5*(7), 772–777. https://doi.org/10.1513/pats.200805-041HR

Danahay, H. L., Lilley, S., Fox, R., Charlton, H., Sabater, J., Button, B., McCarthy, C., Collingwood, S. P., & Gosling, M. (2020). TMEM16A Potentiation: A Novel Therapeutic Approach for the Treatment of Cystic Fibrosis. *American journal of respiratory and critical care medicine*, *201*(8), 946–954. https://doi.org/10.1164/rccm.201908-1641OC

Danahay, H., Atherton, H., Jones, G., Bridges, R. J., & Poll, C. T. (2002). Interleukin-13 induces a hypersecretory ion transport phenotype in human bronchial epithelial cells. *American journal of physiology. Lung cellular and molecular physiology*, *282*(2), L226–L236. https://doi.org/10.1152/ajplung.00311.2001

Dang, S., Feng, S., Tien, J., Peters, C. J., Bulkley, D., Lolicato, M., Zhao, J., Zuberbühler, K., Ye, W., Qi, L., Chen, T., Craik, C. S., Jan, Y. N., Minor, D. L., Jr, Cheng, Y., & Jan, L. Y. (2017). Cryo-EM structures of the TMEM16A calcium-activated chloride channel. *Nature*, *552*(7685), 426–429. https://doi.org/10.1038/nature25024

de la Rosa, D., Li, H., & Canessa, C. M. (2002). Effects of aldosterone on biosynthesis, traffic, and functional expression of epithelial sodium channels in A6 cells. *The Journal of general physiology*, *119*(5), 427–442. https://doi.org/10.1085/jgp.20028559

Debonneville, C., Flores, S. Y., Kamynina, E., Plant, P. J., Tauxe, C., Thomas, M. A., Münster, C., Chraïbi, A., Pratt, J. H., Horisberger, J. D., Pearce, D., Loffing, J., & Staub, O. (2001). Phosphorylation of Nedd4-2 by Sgk1 regulates epithelial Na(+) channel cell surface expression. *The EMBO journal*, *20*(24), 7052–7059. https://doi.org/10.1093/emboj/20.24.7052

Decraene, A., Willems-Widyastuti, A., Kasran, A., De Boeck, K., Bullens, D. M., & Dupont, L. J. (2010). Elevated expression of both mRNA and protein levels of IL-17A in sputum of stable Cystic Fibrosis patients. *Respiratory research*, *11*(1), 177. https://doi.org/10.1186/1465-9921-11-177

Diakov, A., & Korbmacher, C. (2004). A novel pathway of epithelial sodium channel activation involves a serum- and glucocorticoid-inducible kinase consensus motif in the C terminus of the channel's alpha-subunit. *The Journal of biological chemistry*, *279*(37), 38134–38142. https://doi.org/10.1074/jbc.M403260200

Dobin, A., Davis, C. A., Schlesinger, F., Drenkow, J., Zaleski, C., Jha, S., Batut, P., Chaisson, M., & Gingeras, T. R. (2013). STAR: ultrafast universal RNA-seq aligner. *Bioinformatics (Oxford, England)*, *29*(1), 15–21. https://doi.org/10.1093/bioinformatics/bts635

Elborn J. S. (2016). Cystic fibrosis. *Lancet (London, England)*, *388*(10059), 2519–2531. https://doi.org/10.1016/S0140-6736(16)00576-6

Evans, C. M., Williams, O. W., Tuvim, M. J., Nigam, R., Mixides, G. P., Blackburn, M. R., DeMayo, F. J., Burns, A. R., Smith, C., Reynolds, S. D., Stripp, B. R., & Dickey, B. F. (2004). Mucin is produced by clara cells in the proximal airways of antigen-challenged mice. *American journal of respiratory cell and molecular biology*, *31*(4), 382–394. https://doi.org/10.1165/rcmb.2004-0060OC

Everett, L. A., Glaser, B., Beck, J. C., Idol, J. R., Buchs, A., Heyman, M., Adawi, F., Hazani, E., Nassir, E., Baxevanis, A. D., Sheffield, V. C., & Green, E. D. (1997). Pendred syndrome is caused by mutations in a putative sulphate transporter gene (PDS). *Nature genetics*, *17*(4), 411–422. https://doi.org/10.1038/ng1297-411

Fajac, I., & Sermet-Gaudelus, I. (2021). Therapeutic pipeline for individuals with cystic fibrosis with mutations nonresponsive to current cystic fibrosis transmembrane conductance regulator modulators. *Current opinion in pulmonary medicine*, *27*(6), 567–574.

Fanen, P., Wohlhuter-Haddad, A., & Hinzpeter, A. (2014). Genetics of cystic fibrosis: CFTR mutation classifications toward genotype-based CF therapies. *The international journal of biochemistry & cell biology*, *52*, 94–102. https://doi.org/10.1016/j.biocel.2014.02.023

Fulcher, M. L., Gabriel, S., Burns, K. A., Yankaskas, J. R., & Randell, S. H. (2005). Well-differentiated human airway epithelial cell cultures. *Methods in molecular medicine*, *107*, 183–206. https://doi.org/10.1385/1-59259-861-7:183

Gaillard, E. A., Kota, P., Gentzsch, M., Dokholyan, N. V., Stutts, M. J., & Tarran, R. (2010). Regulation of the epithelial Na+ channel and airway surface liquid volume by serine proteases. *Pflugers Archiv : European journal of physiology*, *460*(1), 1–17. https://doi.org/10.1007/s00424-010-0827-z

Galietta, L. J., Pagesy, P., Folli, C., Caci, E., Romio, L., Costes, B., Nicolis, E., Cabrini, G., Goossens, M., Ravazzolo, R., & Zegarra-Moran, O. (2002). IL-4 is a potent modulator of ion transport in the human bronchial epithelium in vitro. *Journal of immunology (Baltimore, Md. : 1950)*, *168*(2), 839–845. https://doi.org/10.4049/jimmunol.168.2.839

Garcia, M. A., Yang, N., & Quinton, P. M. (2009). Normal mouse intestinal mucus release requires cystic fibrosis transmembrane regulator-dependent bicarbonate secretion. *The Journal of clinical investigation*, *119*(9), 2613–2622. https://doi.org/10.1172/JCI38662

Garland, A. L., Walton, W. G., Coakley, R. D., Tan, C. D., Gilmore, R. C., Hobbs, C. A., Tripathy, A., Clunes, L. A., Bencharit, S., Stutts, M. J., Betts, L., Redinbo, M. R., & Tarran, R. (2013). Molecular basis for pH-dependent mucosal dehydration in cystic fibrosis airways. *Proceedings of the National Academy of Sciences of the United States of America*, *110*(40), 15973–15978. https://doi.org/10.1073/pnas.1311999110

Garnett, J. P., Hickman, E., Burrows, R., Hegyi, P., Tiszlavicz, L., Cuthbert, A. W., Fong, P., & Gray, M. A. (2011). Novel role for pendrin in orchestrating bicarbonate secretion in cystic fibrosis transmembrane conductance regulator (CFTR)-expressing airway serous cells. *The Journal of biological chemistry*, *286*(47), 41069–41082. https://doi.org/10.1074/jbc.M111.266734

Genovese, M., Buccirossi, M., Guidone, D., De Cegli, R., Sarnataro, S., di Bernardo, D., & Galietta, L. J. V. (2023). Analysis of inhibitors of the anoctamin-1 chloride channel (transmembrane member 16A, TMEM16A) reveals indirect mechanisms involving alterations in calcium signalling. *British journal of pharmacology*, *180*(6), 775–785. https://doi.org/10.1111/bph.15995

Genovese, M., Guidone, D., Buccirossi, M., Borrelli, A., Rodriguez-Gimeno, A., Bertozzi, F., Bandiera, T., & Galietta, L. J. V. (2022). Pharmacological potentiators of the calcium signaling cascade identified by high-throughput screening. *PNAS nexus*, *2*(1), pgac288. https://doi.org/10.1093/pnasnexus/pgac288

Gleason, C. E., Frindt, G., Cheng, C. J., Ng, M., Kidwai, A., Rashmi, P., Lang, F., Baum, M., Palmer, L. G., & Pearce, D. (2015). mTORC2 regulates renal tubule sodium uptake by promoting ENaC activity. *The Journal of clinical investigation*, *125*(1), 117–128. https://doi.org/10.1172/JCI73935

Gorrieri, G., Scudieri, P., Caci, E., Schiavon, M., Tomati, V., Sirci, F., Napolitano, F., Carrella, D., Gianotti, A., Musante, I., Favia, M., Casavola, V., Guerra, L., Rea, F., Ravazzolo, R., Di Bernardo, D., & Galietta, L. J. (2016). Goblet Cell Hyperplasia Requires High Bicarbonate Transport To Support Mucin Release. *Scientific reports*, *6*, 36016. https://doi.org/10.1038/srep36016

Gray, T., Coakley, R., Hirsh, A., Thornton, D., Kirkham, S., Koo, J. S., Burch, L., Boucher, R., & Nettesheim, P. (2004). Regulation of MUC5AC mucin secretion and airway surface liquid metabolism by IL-1beta in human bronchial epithelia. *American journal of physiology. Lung cellular and molecular physiology*, *286*(2), L320–L330. https://doi.org/10.1152/ajplung.00440.2002

Grubb, B. R., & Boucher, R. C. (1999). Pathophysiology of gene-targeted mouse models for cystic fibrosis. *Physiological reviews*, *79*(1 Suppl), S193–S214. https://doi.org/10.1152/physrev.1999.79.1.S193

Gudis, D., Zhao, K. Q., & Cohen, N. A. (2012). Acquired cilia dysfunction in chronic rhinosinusitis. *American journal of rhinology & allergy*, *26*(1), 1–6. https://doi.org/10.2500/ajra.2012.26.3716

Gustafsson, J. K., & Johansson, M. E. V. (2022). The role of goblet cells and mucus in intestinal homeostasis. *Nature reviews. Gastroenterology & hepatology*, *19*(12), 785–803. https://doi.org/10.1038/s41575-022-00675-x

Gustafsson, J. K., Ermund, A., Ambort, D., Johansson, M. E., Nilsson, H. E., Thorell, K., Hebert, H., Sjövall, H., & Hansson, G. C. (2012). Bicarbonate and functional CFTR channel are required for proper mucin secretion and link cystic fibrosis with its mucus phenotype. *The Journal of experimental medicine*, *209*(7), 1263–1272. https://doi.org/10.1084/jem.20120562

Haggie, P. M., Phuan, P. W., Tan, J. A., Zlock, L., Finkbeiner, W. E., & Verkman, A. S. (2016). Inhibitors of pendrin anion exchange identified in a small molecule screen increase airway surface liquid volume in cystic fibrosis. *FASEB journal : official publication of the Federation of American Societies for Experimental Biology*, *30*(6), 2187–2197. https://doi.org/10.1096/fj.201600223R

Hagner, M., Albrecht, M., Guerra, M., Braubach, P., Halle, O., Zhou-Suckow, Z., Butz, S., Jonigk, D., Hansen, G., Schultz, C., Dittrich, A. M., & Mall, M. A. (2021). IL-17A from innate and adaptive lymphocytes contributes to inflammation and damage in cystic fibrosis lung disease. *The European respiratory journal*, *57*(6), 1900716. https://doi.org/10.1183/13993003.00716-2019

Hao, Y., Hao, S., Andersen-Nissen, E., Mauck, W. M., 3rd, Zheng, S., Butler, A., Lee, M. J., Wilk, A. J., Darby, C., Zager, M., Hoffman, P., Stoeckius, M., Papalexi, E., Mimitou, E. P., Jain, J., Srivastava, A., Stuart, T., Fleming, L. M., Yeung, B., Rogers, A. J., … Satija, R. (2021). Integrated analysis of multimodal single-cell data. *Cell*, *184*(13), 3573–3587.e29. https://doi.org/10.1016/j.cell.2021.04.048

Helve, O., Pitkänen, O., Janér, C., & Andersson, S. (2009). Pulmonary fluid balance in the human newborn infant. *Neonatology*, *95*(4), 347–352. https://doi.org/10.1159/000209300

Hemmi, H., & Akira, S. (2005). TLR signalling and the function of dendritic cells. *Chemical immunology and allergy*, *86*, 120–135. https://doi.org/10.1159/000086657

Higgins, G., Ringholz, F., Buchanan, P., McNally, P., & Urbach, V. (2015). Physiological impact of abnormal lipoxin A_4 production on cystic fibrosis airway epithelium and therapeutic potential. *BioMed research international*, *2015*, 781087. https://doi.org/10.1155/2015/781087

Hoegger, M. J., Fischer, A. J., McMenimen, J. D., Ostedgaard, L. S., Tucker, A. J., Awadalla, M. A., Moninger, T. O., Michalski, A. S., Hoffman, E. A., Zabner, J., Stoltz, D. A., & Welsh, M. J. (2014). Impaired mucus detachment disrupts mucociliary transport in a piglet model of cystic fibrosis. *Science (New York, N.Y.)*, *345*(6198), 818–822. https://doi.org/10.1126/science.1255825

Huang, daW., Sherman, B. T., & Lempicki, R. A. (2009). Bioinformatics enrichment tools: paths toward the comprehensive functional analysis of large gene lists. *Nucleic acids research*, *37*(1), 1–13. https://doi.org/10.1093/nar/gkn923

Huang, daW., Sherman, B. T., & Lempicki, R. A. (2009). Systematic and integrative analysis of large gene lists using DAVID bioinformatics resources. *Nature protocols*, *4*(1), 44–57. https://doi.org/10.1038/nprot.2008.211

Itani, O. A., Chen, J. H., Karp, P. H., Ernst, S., Keshavjee, S., Parekh, K., Klesney-Tait, J., Zabner, J., & Welsh, M. J. (2011). Human cystic fibrosis airway epithelia have reduced Cl- conductance but not increased Na+ conductance. *Proceedings of the National Academy of Sciences of the United States of America*, *108*(25), 10260–10265. https://doi.org/10.1073/pnas.1106695108

Jayaraman, S., Song, Y., Vetrivel, L., Shankar, L., & Verkman, A. S. (2001). Noninvasive in vivo fluorescence measurement of airway-surface liquid depth, salt concentration, and pH. *The Journal of clinical investigation*, *107*(3), 317–324. https://doi.org/10.1172/JCI11154

Kabra, R., Knight, K. K., Zhou, R., & Snyder, P. M. (2008). Nedd4-2 induces endocytosis and degradation of proteolytically cleaved epithelial Na+ channels. *The Journal of biological chemistry*, *283*(10), 6033–6039. https://doi.org/10.1074/jbc.M708555200

Kaiko, G. E., Horvat, J. C., Beagley, K. W., & Hansbro, P. M. (2008). Immunological decision-making: how does the immune system decide to mount a helper T-cell response?. *Immunology*, *123*(3), 326–338. https://doi.org/10.1111/j.1365-2567.2007.02719.x

Keating, D., Marigowda, G., Burr, L., Daines, C., Mall, M. A., McKone, E. F., Ramsey, B. W., Rowe, S. M., Sass, L. A., Tullis, E., McKee, C. M., Moskowitz, S. M., Robertson, S., Savage, J., Simard, C., Van Goor, F., Waltz, D., Xuan, F., Young, T., Taylor-Cousar, J. L., … VX16-445-001 Study Group (2018). VX-445-Tezacaftor-Ivacaftor in Patients with Cystic Fibrosis and One or Two Phe508del Alleles. *The New England journal of medicine*, *379*(17), 1612–1620. https://doi.org/10.1056/NEJMoa1807120

Kim, C. H., Kim, K. E., Yoon, J. H., & Song, K. S. (2009). Upregulation of MUC5AC gene expression by IL-4 through CREB in human airway epithelial cells. *Journal of cellular biochemistry*, *108*(4), 974–981. https://doi.org/10.1002/jcb.22330

Kim, D., Huang, J., Billet, A., Abu-Arish, A., Goepp, J., Matthes, E., Tewfik, M. A., Frenkiel, S., & Hanrahan, J. W. (2019). Pendrin Mediates Bicarbonate Secretion and Enhances Cystic Fibrosis Transmembrane Conductance Regulator Function in Airway Surface Epithelia. *American journal of respiratory cell and molecular biology*, *60*(6), 705–716. https://doi.org/10.1165/rcmb.2018-0158OC

Kitamura, K., & Tomita, K. (2010). Regulation of renal sodium handling through the interaction between serine proteases and serine protease inhibitors. *Clinical and experimental nephrology*, *14*(5), 405–410. https://doi.org/10.1007/s10157-010-0299-7

Knight, K. K., Olson, D. R., Zhou, R., & Snyder, P. M. (2006). Liddle's syndrome mutations increase Na+ transport through dual effects on epithelial Na+ channel surface expression and proteolytic cleavage. *Proceedings of the National Academy of Sciences of the United States of America*, *103*(8), 2805–2808. https://doi.org/10.1073/pnas.0511184103

Knowles, M. R., & Boucher, R. C. (2002). Mucus clearance as a primary innate defense mechanism for mammalian airways. *The Journal of clinical investigation*, *109*(5), 571–577. https://doi.org/10.1172/JCI15217

Ko, S. B., Zeng, W., Dorwart, M. R., Luo, X., Kim, K. H., Millen, L., Goto, H., Naruse, S., Soyombo, A., Thomas, P. J., & Muallem, S. (2004). Gating of CFTR by the STAS domain of SLC26 transporters. *Nature cell biology*, *6*(4), 343–350. https://doi.org/10.1038/ncb1115

Kondo, M., Tamaoki, J., Takeyama, K., Nakata, J., & Nagai, A. (2002). Interleukin-13 induces goblet cell differentiation in primary cell culture from Guinea pig tracheal epithelium. *American journal of respiratory cell and molecular biology*, *27*(5), 536–541. https://doi.org/10.1165/rcmb.4682

Kreda, S. M., Mall, M., Mengos, A., Rochelle, L., Yankaskas, J., Riordan, J. R., & Boucher, R. C. (2005). Characterization of wild-type and deltaF508 cystic fibrosis transmembrane regulator in human respiratory epithelia. *Molecular biology of the cell*, *16*(5), 2154–2167. https://doi.org/10.1091/mbc.e04-11-1010

Kurkowiak, M., Ziętkiewicz, E., & Witt, M. (2015). Recent advances in primary ciliary dyskinesia genetics. *Journal of medical genetics*, *52*(1), 1–9. https://doi.org/10.1136/jmedgenet-2014-102755

Lachowicz-Scroggins, M. E., Boushey, H. A., Finkbeiner, W. E., & Widdicombe, J. H. (2010). Interleukin-13-induced mucous metaplasia increases susceptibility of human airway epithelium to rhinovirus infection. *American journal of respiratory cell and molecular biology*, *43*(6), 652–661. https://doi.org/10.1165/rcmb.2009-0244OC

Lambrecht, B. N., Hammad, H., & Fahy, J. V. (2019). The Cytokines of Asthma. *Immunity*, *50*(4), 975–991. https://doi.org/10.1016/j.immuni.2019.03.018

Lee, E. H., Shin, M. H., Gi, M., Park, J., Song, D., Hyun, Y. M., Ryu, J. H., Seong, J. K., Jeon, Y., Han, G., Namkung, W., Park, M. S., & Choi, J. Y. (2020). Inhibition of Pendrin by a small molecule reduces Lipopolysaccharide-induced acute Lung Injury. *Theranostics*, *10*(22), 9913–9922. https://doi.org/10.7150/thno.46417

Lennox, A. T., Coburn, S. L., Leech, J. A., Heidrich, E. M., Kleyman, T. R., Wenzel, S. E., Pilewski, J. M., Corcoran, T. E., & Myerburg, M. M. (2018). ATP12A promotes mucus dysfunction during Type 2 airway inflammation. *Scientific reports*, *8*(1), 2109. https://doi.org/10.1038/s41598-018-20444-8

Li, H., Salomon, J. J., Sheppard, D. N., Mall, M. A., & Galietta, L. J. (2017). Bypassing CFTR dysfunction in cystic fibrosis with alternative pathways for anion transport. *Current opinion in pharmacology*, *34*, 91–97. https://doi.org/10.1016/j.coph.2017.10.002

Li, X., Villacreses, R., Thornell, I. M., Noriega, J., Mather, S., Brommel, C. M., Lu, L., Zabner, A., Ehler, A., Meyerholz, D. K., Stoltz, D. A., & Zabner, J. (2021). V-Type ATPase Mediates Airway Surface Liquid Acidification in Pig Small Airway Epithelial Cells. *American journal of respiratory cell and molecular biology*, *65*(2), 146–156. https://doi.org/10.1165/rcmb.2020-0349OC

Liu, F., Zhang, Z., Csanády, L., Gadsby, D. C., & Chen, J. (2017). Molecular Structure of the Human CFTR Ion Channel. *Cell*, *169*(1), 85–95.e8. https://doi.org/10.1016/j.cell.2017.02.024

Liu, Q., Liu, K., Cui, G., Huang, X., Yao, S., Guo, W., Qin, Z., Li, Y., Yang, R., Pu, W., Zhang, L., He, L., Zhao, H., Yu, W., Tang, M., Tian, X., Cai, D., Nie, Y., Hu, S., Ren, T., … Zhou, B. (2019). Lung regeneration by multipotent stem cells residing at the bronchioalveolar-duct junction. *Nature genetics*, *51*(4), 728–738. https://doi.org/10.1038/s41588-019-0346-6

Liu, Q., Zhang, X., Huang, H., Chen, Y., Wang, F., Hao, A., Zhan, W., Mao, Q., Hu, Y., Han, L., Sun, Y., Zhang, M., Liu, Z., Li, G. L., Zhang, W., Shu, Y., Sun, L., & Chen, Z. (2023). Asymmetric pendrin homodimer reveals its molecular mechanism as anion exchanger. *Nature communications*, *14*(1), 3012. https://doi.org/10.1038/s41467-023-38303-0

Livraghi, A., & Randell, S. H. (2007). Cystic fibrosis and other respiratory diseases of impaired mucus clearance. *Toxicologic pathology*, *35*(1), 116–129. https://doi.org/10.1080/01926230601060025

Lu, M., Wang, J., Jones, K. T., Ives, H. E., Feldman, M. E., Yao, L. J., Shokat, K. M., Ashrafi, K., & Pearce, D. (2010). mTOR complex-2 activates ENaC by phosphorylating SGK1. *Journal of the American Society of Nephrology : JASN*, *21*(5), 811–818. https://doi.org/10.1681/ASN.2009111168

Ma, T., Thiagarajah, J. R., Yang, H., Sonawane, N. D., Folli, C., Galietta, L. J., & Verkman, A. S. (2002). Thiazolidinone CFTR inhibitor identified by high-throughput screening blocks cholera toxin-induced intestinal fluid secretion. *The Journal of clinical investigation*, *110*(11), 1651–1658. https://doi.org/10.1172/JCI16112

Mall M. A. (2008). Role of cilia, mucus, and airway surface liquid in mucociliary dysfunction: lessons from mouse models. *Journal of aerosol medicine and pulmonary drug delivery*, *21*(1), 13–24. https://doi.org/10.1089/jamp.2007.0659

Mall, M., Bleich, M., Greger, R., Schreiber, R., & Kunzelmann, K. (1998). The amiloride-inhibitable Na+ conductance is reduced by the cystic fibrosis transmembrane conductance regulator in normal but not in cystic fibrosis airways. *The Journal of clinical investigation*, *102*(1), 15–21. https://doi.org/10.1172/JCI2729

Mall, M., Grubb, B. R., Harkema, J. R., O'Neal, W. K., & Boucher, R. C. (2004). Increased airway epithelial Na+ absorption produces cystic fibrosis-like lung disease in mice. *Nature medicine*, *10*(5), 487–493. https://doi.org/10.1038/nm1028

Montoro, D. T., Haber, A. L., Biton, M., Vinarsky, V., Lin, B., Birket, S. E., Yuan, F., Chen, S., Leung, H. M., Villoria, J., Rogel, N., Burgin, G., Tsankov, A. M., Waghray, A., Slyper, M., Waldman, J., Nguyen, L., Dionne, D., Rozenblatt-Rosen, O., Tata, P. R., … Rajagopal, J. (2018). A revised airway epithelial hierarchy includes CFTR-expressing ionocytes. *Nature*, *560*(7718), 319–324. https://doi.org/10.1038/s41586-018-0393-7

Moran O. (2017). The gating of the CFTR channel. *Cellular and molecular life sciences : CMLS*, *74*(1), 85–92. https://doi.org/10.1007/s00018-016-2390-z

Mou, H., Vinarsky, V., Tata, P. R., Brazauskas, K., Choi, S. H., Crooke, A. K., Zhang, B., Solomon, G. M., Turner, B., Bihler, H., Harrington, J., Lapey, A., Channick, C., Keyes, C., Freund, A., Artandi, S., Mense, M., Rowe, S., Engelhardt, J. F., Hsu, Y. C., … Rajagopal, J. (2016). Dual SMAD Signaling Inhibition Enables Long-Term Expansion of Diverse Epithelial Basal Cells. *Cell stem cell*, *19*(2), 217–231. https://doi.org/10.1016/j.stem.2016.05.012

Nagel, G., Szellas, T., Riordan, J. R., Friedrich, T., & Hartung, K. (2001). Non-specific activation of the epithelial sodium channel by the CFTR chloride channel. *EMBO reports*, *2*(3), 249–254. https://doi.org/10.1093/embo-reports/kve045

Nofziger, C., Dossena, S., Suzuki, S., Izuhara, K., & Paulmichl, M. (2011). Pendrin function in airway epithelia. *Cellular physiology and biochemistry : international journal of experimental cellular physiology, biochemistry, and pharmacology*, *28*(3), 571–578. https://doi.org/10.1159/000335115

Ohana, E., Yang, D., Shcheynikov, N., & Muallem, S. (2009). Diverse transport modes by the solute carrier 26 family of anion transporters. *The Journal of physiology*, *587*(Pt 10), 2179–2185. https://doi.org/10.1113/jphysiol.2008.164863

Patel-Chamberlin, M., Varasteh Kia, M., Xu, J., Barone, S., Zahedi, K., & Soleimani, M. (2016). The Role of Epithelial Sodium Channel ENaC and the Apical Cl-/HCO3- Exchanger Pendrin in Compensatory Salt Reabsorption in the Setting of Na-Cl Cotransporter (NCC) Inactivation. *PloS one*, *11*(3), e0150918. https://doi.org/10.1371/journal.pone.0150918

Paulino, C., Kalienkova, V., Lam, A. K. M., Neldner, Y., & Dutzler, R. (2017). Activation mechanism of the calcium-activated chloride channel TMEM16A revealed by cryo-EM. *Nature*, *552*(7685), 421–425. https://doi.org/10.1038/nature24652

Pedemonte, N., & Galietta, L. J. (2014). Structure and function of TMEM16 proteins (anoctamins). *Physiological reviews*, *94*(2), 419–459. https://doi.org/10.1152/physrev.00039.201

Pedemonte, N., Caci, E., Sondo, E., Caputo, A., Rhoden, K., Pfeffer, U., Di Candia, M., Bandettini, R., Ravazzolo, R., Zegarra-Moran, O., & Galietta, L. J. (2007). Thiocyanate transport in resting and IL-4-stimulated human bronchial epithelial cells: role of pendrin and anion channels. *Journal of immunology (Baltimore, Md. : 1950)*, *178*(8), 5144–5153. https://doi.org/10.4049/jimmunol.178.8.5144

Pezzulo, A. A., Tang, X. X., Hoegger, M. J., Abou Alaiwa, M. H., Ramachandran, S., Moninger, T. O., Karp, P. H., Wohlford-Lenane, C. L., Haagsman, H. P., van Eijk, M., Bánfi, B., Horswill, A. R., Stoltz, D. A., McCray, P. B., Jr, Welsh, M. J., & Zabner, J. (2012). Reduced airway surface pH impairs bacterial killing in the porcine cystic fibrosis lung. *Nature*, *487*(7405), 109–113. https://doi.org/10.1038/nature11130

Plasschaert, L. W., Žilionis, R., Choo-Wing, R., Savova, V., Knehr, J., Roma, G., Klein, A. M., & Jaffe, A. B. (2018). A single-cell atlas of the airway epithelium reveals the CFTR-rich pulmonary ionocyte. *Nature*, *560*(7718), 377–381. https://doi.org/10.1038/s41586-018-0394-6

Qiu, L. Y., Swarts, H. G. P., Tonk, E. C. M., Willems, P. H. G. M., Koenderink, J. B., & De Pont, J. J. H. H. M. (2006). Conversion of the low affinity ouabain-binding site of non-gastric H,K-ATPase into a high affinity binding site by substitution of only five amino acids. *The Journal of biological chemistry*, *281*(19), 13533–13539. https://doi.org/10.1074/jbc.M600551200

Raidt, J., Wallmeier, J., Hjeij, R., Onnebrink, J. G., Pennekamp, P., Loges, N. T., Olbrich, H., Häffner, K., Dougherty, G. W., Omran, H., & Werner, C. (2014). Ciliary beat pattern and frequency in genetic variants of primary ciliary dyskinesia. *The European respiratory journal*, *44*(6), 1579–1588. https://doi.org/10.1183/09031936.00052014

Rehman, T., Karp, P. H., Tan, P., Goodell, B. J., Pezzulo, A. A., Thurman, A. L., Thornell, I. M., Durfey, S. L., Duffey, M. E., Stoltz, D. A., McKone, E. F., Singh, P. K., & Welsh, M. J. (2021). Inflammatory cytokines TNF-α and IL-17 enhance the efficacy of cystic fibrosis transmembrane conductance regulator modulators. *The Journal of clinical investigation*, *131*(16), e150398. https://doi.org/10.1172/JCI150398

Rehman, T., Thornell, I. M., Pezzulo, A. A., Thurman, A. L., Romano Ibarra, G. S., Karp, P. H., Tan, P., Duffey, M. E., & Welsh, M. J. (2020). TNFα and IL-17 alkalinize airway surface liquid through CFTR and pendrin. *American journal of physiology. Cell physiology*, *319*(2), C331–C344. https://doi.org/10.1152/ajpcell.00112.2020

Ridley, C., & Thornton, D. J. (2018). Mucins: the frontline defence of the lung. *Biochemical Society transactions*, *46*(5), 1099–1106. https://doi.org/10.1042/BST20170402

Robinson, M. D., McCarthy, D. J., & Smyth, G. K. (2010). edgeR: a Bioconductor package for differential expression analysis of digital gene expression data. *Bioinformatics (Oxford, England)*, *26*(1), 139–140. https://doi.org/10.1093/bioinformatics/btp616

Rock, J. R., & Hogan, B. L. (2011). Epithelial progenitor cells in lung development, maintenance, repair, and disease. *Annual review of cell and developmental biology*, *27*, 493–512. https://doi.org/10.1146/annurev-cellbio-100109-104040

Rock, J. R., Onaitis, M. W., Rawlins, E. L., Lu, Y., Clark, C. P., Xue, Y., Randell, S. H., & Hogan, B. L. (2009). Basal cells as stem cells of the mouse trachea and human airway epithelium. *Proceedings of the National Academy of Sciences of the United States of America*, *106*(31), 12771–12775. https://doi.org/10.1073/pnas.0906850106

Rossier, B. C., & Stutts, M. J. (2009). Activation of the epithelial sodium channel (ENaC) by serine proteases. *Annual review of physiology*, *71*, 361–379. https://doi.org/10.1146/annurev.physiol.010908.163108

Rotin, D., & Staub, O. (2021). Function and Regulation of the Epithelial Na^+ Channel ENaC. *Comprehensive Physiology*, *11*(3), 2017–2045. https://doi.org/10.1002/cphy.c200012

Ruysseveldt, E., Martens, K., & Steelant, B. (2021). Airway Basal Cells, Protectors of Epithelial Walls in Health and Respiratory Diseases. *Frontiers in allergy*, *2*, 787128. https://doi.org/10.3389/falgy.2021.787128

Saint-Criq, V., & Gray, M. A. (2017). Role of CFTR in epithelial physiology. *Cellular and molecular life sciences : CMLS*, *74*(1), 93–115. https://doi.org/10.1007/s00018-016-2391-y

Salomon, J. J., Spahn, S., Wang, X., Füllekrug, J., Bertrand, C. A., & Mall, M. A. (2016). Generation and functional characterization of epithelial cells with stable expression of SLC26A9 Cl- channels. *American journal of physiology. Lung cellular and molecular physiology*, *310*(7), L593–L602. https://doi.org/10.1152/ajplung.00321.2015

Schroeder, B. C., Cheng, T., Jan, Y. N., & Jan, L. Y. (2008). Expression cloning of TMEM16A as a calcium-activated chloride channel subunit. *Cell*, *134*(6), 1019–1029. https://doi.org/10.1016/j.cell.2008.09.003

Schultz, A., Puvvadi, R., Borisov, S. M., Shaw, N. C., Klimant, I., Berry, L. J., Montgomery, S. T., Nguyen, T., Kreda, S. M., Kicic, A., Noble, P. B., Button, B., & Stick, S. M. (2017). Airway surface liquid pH is not acidic in children with cystic fibrosis. *Nature communications*, *8*(1), 1409. https://doi.org/10.1038/s41467-017-00532-5

Scudieri, P., Caci, E., Bruno, S., Ferrera, L., Schiavon, M., Sondo, E., Tomati, V., Gianotti, A., Zegarra-Moran, O., Pedemonte, N., Rea, F., Ravazzolo, R., & Galietta, L. J. (2012). Association of TMEM16A chloride channel overexpression with airway goblet cell metaplasia. *The Journal of physiology*, *590*(23), 6141–6155. https://doi.org/10.1113/jphysiol.2012.240838

Scudieri, P., Musante, I., Caci, E., Venturini, A., Morelli, P., Walter, C., Tosi, D., Palleschi, A., Martin-Vasallo, P., Sermet-Gaudelus, I., Planelles, G., Crambert, G., & Galietta, L. J. (2018). Increased expression of ATP12A proton pump in cystic fibrosis airways. *JCI insight*, *3*(20), e123616. https://doi.org/10.1172/jci.insight.123616

Scudieri, P., Musante, I., Venturini, A., Guidone, D., Genovese, M., Cresta, F., Caci, E., Palleschi, A., Poeta, M., Santamaria, F., Ciciriello, F., Lucidi, V., & Galietta, L. J. V. (2020). Ionocytes and CFTR Chloride Channel Expression in Normal and Cystic Fibrosis Nasal and Bronchial Epithelial Cells. *Cells*, *9*(9), 2090. https://doi.org/10.3390/cells9092090

Sertl, K., Takemura, T., Tschachler, E., Ferrans, V. J., Kaliner, M. A., & Shevach, E. M. (1986). Dendritic cells with antigen-presenting capability reside in airway epithelium, lung parenchyma, and visceral pleura. *The Journal of experimental medicine*, *163*(2), 436–451. https://doi.org/10.1084/jem.163.2.436

Shah, V. S., Meyerholz, D. K., Tang, X. X., Reznikov, L., Abou Alaiwa, M., Ernst, S. E., Karp, P. H., Wohlford-Lenane, C. L., Heilmann, K. P., Leidinger, M. R., Allen, P. D., Zabner, J., McCray, P. B., Jr, Ostedgaard, L. S., Stoltz, D. A., Randak, C. O., & Welsh, M. J. (2016). Airway acidification initiates host defense abnormalities in cystic fibrosis mice. *Science (New York, N.Y.)*, *351*(6272), 503–507. https://doi.org/10.1126/science.aad5589

Shcheynikov, N., Ko, S. B., Zeng, W., Choi, J. Y., Dorwart, M. R., Thomas, P. J., & Muallem, S. (2006). Regulatory interaction between CFTR and the SLC26 transporters. *Novartis Foundation symposium*, *273*, 177–264.

Shei, R. J., Peabody, J. E., Kaza, N., & Rowe, S. M. (2018). The epithelial sodium channel (ENaC) as a therapeutic target for cystic fibrosis. *Current opinion in pharmacology*, *43*, 152–165. https://doi.org/10.1016/j.coph.2018.09.007

Snouwaert, J. N., Brigman, K. K., Latour, A. M., Malouf, N. N., Boucher, R. C., Smithies, O., & Koller, B. H. (1992). An animal model for cystic fibrosis made by gene targeting. *Science (New York, N.Y.)*, *257*(5073), 1083–1088. https://doi.org/10.1126/science.257.5073.1083

Sweadner, K. J., & Donnet, C. (2001). Structural similarities of Na,K-ATPase and SERCA, the Ca(2+)-ATPase of the sarcoplasmic reticulum. *The Biochemical journal*, *356*(Pt 3), 685–704. https://doi.org/10.1042/0264-6021:3560685

Twigg, M. S., Brockbank, S., Lowry, P., FitzGerald, S. P., Taggart, C., & Weldon, S. (2015). The Role of Serine Proteases and Antiproteases in the Cystic Fibrosis Lung. *Mediators of inflammation*, *2015*, 293053. https://doi.org/10.1155/2015/293053

Van Goor, F., Hadida, S., Grootenhuis, P. D., Burton, B., Cao, D., Neuberger, T., Turnbull, A., Singh, A., Joubran, J., Hazlewood, A., Zhou, J., McCartney, J., Arumugam, V., Decker, C., Yang, J., Young, C., Olson, E. R., Wine, J. J., Frizzell, R. A., Ashlock, M., … Negulescu, P. (2009). Rescue of CF airway epithelial cell function in vitro by a CFTR potentiator, VX-770. *Proceedings of the National Academy of Sciences of the United States of America*, *106*(44), 18825–18830. https://doi.org/10.1073/pnas.0904709106

Vieira Braga, F. A., Kar, G., Berg, M., Carpaij, O. A., Polanski, K., Simon, L. M., Brouwer, S., Gomes, T., Hesse, L., Jiang, J., Fasouli, E. S., Efremova, M., Vento-Tormo, R., Talavera-López, C., Jonker, M. R., Affleck, K., Palit, S., Strzelecka, P. M., Firth, H. V., Mahbubani, K. T., … Teichmann, S. A. (2019). A cellular census of human lungs identifies novel cell states in health and in asthma. *Nature medicine*, *25*(7), 1153–1163. https://doi.org/10.1038/s41591-019-0468-5

Walter, J. D., Sawicka, M., & Dutzler, R. (2019). Cryo-EM structures and functional characterization of murine Slc26a9 reveal mechanism of uncoupled chloride transport. *eLife*, *8*, e46986. https://doi.org/10.7554/eLife.46986

Widdicombe J. H. (2002). Regulation of the depth and composition of airway surface liquid. *Journal of anatomy*, *201*(4), 313–318. https://doi.org/10.1046/j.1469-7580.2002.00098.x
Wullschleger, S., Loewith, R., & Hall, M. N. (2006). TOR signaling in growth and metabolism. *Cell*, *124*(3), 471–484. https://doi.org/10.1016/j.cell.2006.01.016

Xu, J., Yu, H., & Sun, X. (2020). Less Is More: Rare Pulmonary Neuroendocrine Cells Function as Critical Sensors in Lung. *Developmental cell*, *55*(2), 123–132. https://doi.org/10.1016/j.devcel.2020.09.024

Yang, Y. D., Cho, H., Koo, J. Y., Tak, M. H., Cho, Y., Shim, W. S., Park, S. P., Lee, J., Lee, B., Kim, B. M., Raouf, R., Shin, Y. K., & Oh, U. (2008). TMEM16A confers receptor-activated calcium-dependent chloride conductance. *Nature*, *455*(7217), 1210–1215. https://doi.org/10.1038/nature07313

Young, V. C., Nakanishi, H., Meyer, D. J., Nishizawa, T., Oshima, A., Artigas, P., & Abe, K. (2022). Structure and function of H^+/K^+ pump mutants reveal Na^+/K^+ pump mechanisms. *Nature communications*, *13*(1), 5270. https://doi.org/10.1038/s41467-022-32793-0

Zabner, J., Smith, J. J., Karp, P. H., Widdicombe, J. H., & Welsh, M. J. (1998). Loss of CFTR chloride channels alters salt absorption by cystic fibrosis airway epithelia in vitro. *Molecular cell*, *2*(3), 397–403. https://doi.org/10.1016/s1097-2765(00)80284-1

Zheng, G. X., Terry, J. M., Belgrader, P., Ryvkin, P., Bent, Z. W., Wilson, R., Ziraldo, S. B., Wheeler, T. D., McDermott, G. P., Zhu, J., Gregory, M. T., Shuga, J., Montesclaros, L., Underwood, J. G., Masquelier, D. A., Nishimura, S. Y., Schnall-Levin, M., Wyatt, P. W., Hindson, C. M., Bharadwaj, R., … Bielas, J. H. (2017). Massively parallel digital transcriptional profiling of single cells. *Nature communications*, *8*, 14049. https://doi.org/10.1038/ncomms14049

6. FIGURE LEGENDS

Figure 1. Schematic representation of human respiratory system. The image shows the separation between conducting and respiratory zones and how the respiratory system branches into bronchi, bronchioles and alveoli. In the bottom part, the cell types that compose the epithelial surface are indicated. Adapted from Bustamante-Marin & Ostrowski, 2017.

Figure 2. Ciliated cells, axonemal structure and ciliary beating. A, left: cilia localization in a human tracheobronchial epithelial cell culture. **A, right:** cross-section view of cilia axonemal structure by TEM microscopy. Modified from Livraghi & Randell, 2007. **B:** schematic representation of axonemal structure. Adapted from Bustamante-Marin & Ostrowski, 2017. **C, left:** image of nasal epithelium by SEM. Adapted from Gudis et al., 2012. **C, right:** immunofluorescence of ciliated cell from nasal brushing, staining for acetylated tubulin (Ac-tubulin, magenta). **D:** diagram of ciliary beat cycle. Adapted from Raidt et al., 2014.

Figure 3. Structure and function of goblet cells. A: schematic representation of mucus production, packaging, expansion and release from a goblet cell. Modified from Gustaffson & Johansson, 2022. **B, top:** immunofluorescence of goblet cell from nasal brushing, staining for MUC5AC (red). **B, bottom:** image of tracheal guinea pig goblet cell by TEM. Adapted from Kondo et al., 2002.

Figure 4. New schematic representation of cell types that compose the airway epithelium. Beside basal, ciliated and goblet cells, new rare cell types (Tuft, PNeC, ionocytes, Hillock) have been identified. Adapted from Montoro et al., 2018.

Figure 5. ASL composition. **A, top:** perfluorocarbon-OsO_4 fixation of cultured human tracheobronchial epithelial cells preserves PCL and ML structure. **A, bottom:** TEM of the black box area indicated in the top image, in which PCL an ML are indicated. Modified from Livraghi & Randell, 2007. **B:** schematic representation of normal and collapsed PCL and ML. Adapted from Button et al., 2012.

Figure 6. Schematic representation of transepithelial ion transport (simplified). The cartoon shows main ion channels and transporters that are expressed in the airway epithelial cells. The ion transport activity is indicated for each of them. This model does not depict other channels and transporters that are not taken into consideration in the following paragraphs and their differential expression in different cell types. Created with Biorender.com.

Figure 7. ENaC channel structure. A: structural model of the rat αENaC subunit. The two transmembrane regions with intracellular N- and C- termini and the large extracellular loop are represented. Modified from Gaillard et al., 2010. **B:** ENaC channel with α,β and ɣ subunits. Adapted from Ahmad et al., 2023.

Figure 8. ENaC proteolytic activation, ubiquitination and degradation. Graphical representation of ENaC trafficking into the plasma membrane, activation by proteases and ubiquitination and degradation process controlled by SGK1. Created with Biorender.com.

Figure 9. CFTR channel. Structure of human CFTR in the dephosphorylated, ATP-free conformation. Adapted from Liu et al., 2017.

Figure 10. CFTR mutations. CFTR mutations are divided into six classes based on their implication on channel function. Adapted from Elborn et al., 2016.

Figure 11. TMEM16A structure. Left: electron microscopy density map of TMEM16A. **Right:** TM1-10 superimposed on the electron microscopy density map. Adapted from Dang et al., 2017.

Figure 12. Structure of non-gastric H^+/K^+-ATPase (ATP12A). Electron density map and cartoon model of ATP12A. The α and β subunit (ATP1B1) are shown in cyan and gray, respectively. K^+ ions are shown as purple spheres. The cytoplasmic A, P and N domains are indicated. Adapted from Young et al., 2022.

Figure 13. Structure of SLC26A4 (Pendrin). Schematic topology of pendrin: the NTD, core region, gate region and STAS domain are indicated in yellow, blue, green and pink, respectively. The anion binding pocket is shown as a dashed circle in cyan. Adapted from Liu et al., 2023.

Figure 14: Experimental workflow for analysis of freshly collected nasal epithelial cells. The nasal cells collected by cytological brush were freshly fixed and shipped to the laboratory, where were processed for immunofluorescence. Created with Biorender.com.

Figure 15: Expansion and differentiation steps for bronchial epithelial cells. Stem cells were collected by explanted lungs and expanded in a proliferative medium containing SMAD and Rho kinase inhibitors. The cells were then plated on porous support and after 24 hours the apical medium was completely removed, starting the differentiation process under ALI configuration. After 14-21 days, full mucociliary differentiation was achieved. Created with Biorender.com.

Figure 16: Experimental workflow for immunofluorescence of cultured bronchial epithelial cells. The bronchial epithelial cells grown on porous supports were fixed in formalin once achieved full differentiation. They were stained with appropriate primary and secondary antibodies, then the porous membrane was excised and mounted on slide for confocal microscopy imaging. Created with Biorender.com.

Figure 17: Experimental workflow for Western blot of bronchial epithelial cells. The bronchial epithelial cells grown on porous support were lysed. The obtained lysates were then processed for Western blot as described. Created with Biorender.com.

Figure 18: Schematic representation of short-circuit current recordings. The porous supports carrying the differentiated airway epithelia were mounted on a specific slot for Transwell or Snapwell and inserted in the vertical Ussing-like chamber, formed by the apical and basolateral hemichambers, both filled with Ringer solution and connected to voltage and current electrodes. Two connecting tubes allow 5% CO_2/95% air bubbling, and the instrument was heated to 37 °C. Every chamber is connected to a pre-amplifier and to the acquisition system. Created with Biorender.com.

Figure 19: Experimental workflow for FRAP experiments. The bronchial epithelial cells were seeded on porous supports in upside-down configuration. The apical surface was stained with FITC-dextran and, after 3 hours of incubation, they were mounted on Nikon Eclipse Ti-E Spinning Disk in a controlled atmosphere. The photobleaching of a circular ROI was applied and the fluorescence recovery was followed. Created with Biorender.com.

Figure 20: Experimental workflow for MPT. The bronchial epithelial cells were seeded on porous and black microbeads were added on the apical surface. Then MPT was acquired with Leica M205FA stereomicroscope and analyzed as reported. Created with Biorender.com.

Figure 21: Experimental workflow for large volume in situ pH assay. 60 µl of SNARF-1 dextran +/- compounds were added on the apical surface and incubated for 3 hours. Then, fluorescence was read in a microplate reader and values of fluorescence were converted to pH through a calibration curve. Created with Biorender.com.

Figure 22: Experimental workflow for large volume ex situ pH assay. 200 µl of PBS +/- compounds plus 200 µl of mineral oil were added on the apical surface and incubated for 6 hours. Then, the fluid was recovered and centrifuged to separate the oil from the aqueous solution. 50 µl of the liquid phase were added to a 96-well plate with 0.5 µl of SNARF-1 dextran. Fluorescence was read in a microplate reader and values of fluorescence were converted to pH through a calibration curve. Created with Biorender.com.

Figure 23: Experimental workflow for small volume in situ pH assay. 5 µl of SNARF-1 dextran were added on the apical surface and incubated for 3 hours. Then, fluorescence was read in a microplate reader and values of fluorescence were converted to pH through a calibration curve. At the same time, images of SNARF-1 spot were taken by Leica M205FA stereomicroscope. Created with Biorender.com.

Figure 24. Detection of ATP12A protein in nasal brushings. Low-magnification (top) and high-magnification (bottom) of representative confocal microscope images showing ATP12A protein (green) in freshly fixed nasal brushings derived from non-CF (left) and CF (right) patients. MUC5AC (red) and acetylated tubulin (i.e., cilia, magenta) were also detected. Rectangles in the low-magnification images indicate the magnified regions. Rectangles in the high-magnification images show areas that were considered for ATP12A expression analysis. Scale bar: 20 µm. Adapted from Guidone et al., 2022.

Figure 25. Analysis of ATP12A protein detection in nasal brushings. Top, left: scatter dot plot showing percentage of $ATP12A^+$ cells in non-CF healthy individuals, CF patients, and in subjects with rhinitis. **, $p < 0.01$; ***, $p < 0.001$ versus healthy control group (Kruskal-Wallis followed by Dunn's post hoc test). Top, right: percentage of $ATP12A^+$ cells vs. FEV1, the straight line shows the best linear fit of the data. Bottom, left: percentage of $ATP12A^+$ cells vs. age, the straight line shows the best linear fit of the data. Bottom, right: percentage of $ATP12A^+$ ciliated cells versus percentage of $ATP12A^+$ cells in the total population, the straight line shows the best linear fit of the data (Pearson's $R = 0.6743$, $p < 0.001$). In all graphs: each symbol reports the average value of a single patient. Adapted from Guidone et al., 2022.

Figure 26. Upregulation of ATP12A by IL-17/TNF-α by immunofluorescence analysis. Left: representative confocal microscope images showing detection of ATP12A (green) and acetylated tubulin (i.e., cilia, magenta). Images are xy scans of CF cultured bronchial epithelial cells treated for 72 hours with/without cytokines (10 ng/mL for IL-6, IL-1β, TNF-α, IFN-α, and IFN-γ; 20 ng/mL for IL-17). Scale bar: 25 µm. Right: scatter dot plot reporting percentage of $ATP12A^+$ cells in bronchial epithelia with indicated treatments. *, $p < 0.05$; ***, $p < 0.001$ versus control; ###, $p < 0.001$ between indicated conditions (ANOVA and Tukey's post hoc test). Adapted from Guidone et al., 2022.

Figure 27. Upregulation of ATP12A by IL-17/TNF-α by Western blot analysis. Representative images (left) and summary of data (right) deriving from Western blot analysis of ATP12A protein in lysates of bronchial epithelial cells treated with/without single cytokines or cytokine combinations. The scatter dot

plots report the band intensity for ATP12A normalized for GAPDH expression. Data were obtained from 5 CF and 5 non-CF bronchial cell preparations. **, $p < 0.01$; ***, $p < 0.001$ versus control (ANOVA and Dunnett's post hoc test). Adapted from Guidone et al., 2022.

Figure 28. Upregulation of ATP12A function by IL-17/TNF-α. Apical fluid pH measurements with SNARF-1 dextran probe in non-CF (left) and CF (right) bronchial epithelia. Cells were treated with/without IL-17 + TNF-α. Experiments were done in HCO_3^--free conditions. Where indicated, the apical solution contained ouabain (200 μM), bafilomycin A1 (100 nM), or both compounds together. pH was measured after 3 hours of incubation under CO_2-free conditions. ***, $p < 0.001$ versus control; #, $p < 0.05$ and ###, $p < 0.001$ between indicated conditions; §, $p < 0.05$ and §§§, $p < 0.001$ for treated versus untreated epithelia (ANOVA and Tukey's post hoc test). Adapted from Guidone et al., 2022.

Figure 29. Top 80 genes upregulated by IL-17/TNF-α combination in cultured bronchial epithelia. The bar graph shows the extent of expression of indicated genes as determined by bulk RNAseq in non-CF cultured bronchial epithelia, in term of log_2fold change respect to control. Color codes indicate gene function. Adapted from Guidone et al., 2022.

Figure 30. Analysis of gene expression changes in epithelia treated with inflammatory stimuli. Bar graphs report the expression changes for indicated genes in epithelia treated with IL-17 + TNF-α, TNF-α, IL-17, and IL-4. Data were obtained by RNA-Seq. Red and green indicate statistically significant upregulation and downregulation, respectively. Adapted from Guidone et al., 2022.

Figure 31. Analysis of biological processes modulated in epithelia treated with inflammatory stimuli. Left: biological processes that were associated with gene expression changes induced by TNF-α/IL-17 treatment. Right: Venn diagram showing extent of overlap for genes whose expression was upregulated by indicated cytokine treatment. Adapted from Guidone et al., 2022.

Figure 32. Comparison of gene expression changes induced by IL-17/TNF-α in non-CF and CF cultured bronchial epithelia. The heat maps show the change in expression for the top 150 upregulated genes in CF and non-CF epithelia. Adapted from Guidone et al., 2022.

Figure 33. Analysis of epithelial transcriptome by scRNA-Seq. Top: global representation of gene expression in epithelia kept under control conditions (left) or treated with IL-17/TNF-α (right). Each dot represents a single cell, whose position in the 2D map reports the transcriptional similarity with respect to the neighbor cells. The different colors and numbers correspond to cells clusters with similar transcriptome. Bottom: two-dimensional maps showing the expression of indicated genes within the epithelial cell population. MUC5B, SLC26A4, ATP12A, ADRB2, SLC5A1, and SLC5A8 expression is particularly concentrated in the region corresponding to cluster 1, which is enriched by IL-17/TNF-α treatment. Adapted from Guidone et al., 2022.

Figure 34. Modification of electrogenic ion transport by IL-17/TNF-α. Representative traces and summary of data from short-circuit current recordings done on non-CF (top) and CF (bottom) bronchial epithelia, treated with/without IL-17/TNF-α combination. During recordings, epithelia were sequentially exposed to: amiloride (10 μM), CPT-cAMP (100 μM), $CFTR_{inh}$-172 (I-172, 20 μM), UTP (100 μM), and Ani9 (5 μM). Red arrowhead: higher residual current in cytokine treated epithelia. The scatter dot plots report, for control and IL-17/TNF-α–treated (I+T) epithelia, the amplitude of amiloride, $CFTR_{inh}$-172, and

UTP effects, which are representative of ENaC, CFTR, and TMEM16A function, respectively. *, $p < 0.05$; **, $p < 0.01$; and ***, $p < 0.001$ versus control (Mann-Whitney U test). Adapted from Guidone et al., 2022.

Figure 35. Functional upregulation of SLC5A1 transport by IL-17/TNF-α. Representative short-circuit current recordings (left) and summary of data (right) showing effect of mizagliflozin (10 μM) on control and IL-17/TNF-α–treated (I+T–treated) epithelia. Mizagliflozin was added in the presence of amiloride, $CFTR_{inh}$-172, and Ani9. ***, $p < 0.001$ versus control (Mann-Whitney U test). Adapted from Guidone et al., 2022.

Figure 36. Mechanism of ENaC upregulation by IL-17/TNF-α. Representative short-circuit current traces (left) and summary of data (right) for experiments on epithelia treated with/without IL-17/TNF-α for 72 hours. During recordings, elastase (1.5 μM) and amiloride (10 μM) were sequentially added. Where indicated, epithelia were apically treated with camostat (3 μM) for 18 hours. The scatter dot plot shows, for experiments with camostat pretreatment, the ratio I2/I1, where I1 and I2 are the current amplitudes before and after elastase, as indicated by blue and red arrows, respectively. **, $p < 0.01$ (Student's t test). Adapted from Guidone et al., 2022.

Figure 37. Analysis of ENaC current rundown induced by camostat. Left: Representative traces from experiments with/without IL-17/TNF-α treatment in which camostat (3 μM) and amiloride were sequentially added. Where indicated, experiments also included addition of elastase (1.5 μM) after camostat. Right: summary of data showing the rate of ENaC current decay after camostat addition (C, control; I+T, IL-17/TNF-α). Data ($t_{1/2}$) report the time at which the current decayed to half of initial amplitude. ***, $p < 0.001$ (Student's t test). Adapted from Guidone et al., 2022.

Figure 38. Detection of SCNN1A protein in bronchial epithelial cells. Representative confocal microscope images, from control- and IL-17/TNF-α–treated epithelia, in which SCNN1A, ZO-1, and cilia were detected by immunofluorescence. Scale bar: 25 μm. Adapted from Guidone et al., 2022.

Figure 39. ENaC current rundown induced by SGK1 inhibition. Top: representative short-circuit current traces (left) and summary of data (right) for experiments where control- and IL-17/TNF-α–treated epithelia were apically exposed to 25 μM GSK650394 before amiloride. The scatter dot plot reports the $t_{1/2}$ values for each condition, *, $p < 0.05$ versus control (Student's t test). Bottom: the figure shows representative short-circuit current recordings from cultured bronchial epithelia treated in control conditions or with IL-17/TNF-α, in which the addition of elastase in epithelia treated with GSK650394 is ineffective. Adapted from Guidone et al., 2022.

Figure 40. ENaC current rundown induced by mTORC2 inhibition. Representatives short-circuit current traces and summary of data for experiments where control- and IL-17/TNF-α–treated epithelia were apically exposed to 5 μM PP242 before amiloride. The scatter dot plots report the $t_{1/2}$ values for each condition (ns = not significant). Adapted from Guidone et al., 2022.

Figure 41. Effect of β-adrenergic stimulus on short circuit current recordings. Representative traces (left) and summary of data (right) for short-circuit current experiments on epithelia treated with/without IL-17/TNF-α, in which isoproterenol (10 and 100 nM) was added to stimulate CFTR activity. Where indicated $CFTR_{inh}$-172 (20 μM) and propranolol (5 μM) were also added. The scatter dot plot shows the amplitude of $CFTR_{inh}$-172 effect in epithelia previously stimulated with isoproterenol. ***, $p < 0.001$ versus control (Student's t test). Adapted from Guidone et al., 2022.

Figure 42. Analysis of mucociliary transport by video microscopy. The graphs report the velocity of microbeads on non-CF (left) and CF (right) cultured bronchial epithelia. Epithelia were treated for 72 h with/without IL-17/TNF-α and then stimulated for 3 h with isoproterenol or vehicle (100 nM). *, $p < 0.05$; **, $p < 0.01$; ***, $p < 0.001$; ns, not significant (Kruskal-Wallis and Dunn's test). Adapted from Guidone et al., 2022.

Figure 43. Effect of IL-17 + TNF-α and β-adrenergic stimulus on airway surface properties. Data from FRAP experiments on non-CF (top) or CF (bottom) epithelia treated with/without IL-17/TNF-α (72 hours). Where indicated, isoproterenol (100 nM) was added for 3 hours on the basolateral side before experiments. Representative images (left) show the epithelial surface, labeled with FITC-dextran, after photobleaching of a circular area and then after a 60-second recovery time. The traces on the side of each image pair report the time course of fluorescence recovery. The vertical dashed line indicates the 30-second time point. Scatter dot plots (right) show the normalized fluorescence value measured at 30 seconds after photobleaching. ***, $p < 0.001$ (Kruskal-Wallis and Dunn's test). Adapted from Guidone et al., 2022.

Figure 44. Effect of IL-17 + TNF-α and β-adrenergic stimulus on apical pH. Measurement of pH in the apical solution (large volume ex situ pH assay) for non-CF (top) and CF (bottom) epithelia, treated with/without IL-17/TNF-α. Where indicated, the apical solution contained ouabain (ouab, 200 μM) or PDS_{inh}-A01 (PDS, 25 μM), whereas the basolateral solution included isoproterenol (100 nM). *, $p < 0.5$; **, $p < 0.01$; ***, $p < 0.001$ (ANOVA with Tukey's post hoc test). Adapted from Guidone et al., 2022.

Figure 45. Evaluation of SLC26A4 inhibitors. Left: representative traces showing quenching of halide-sensitive yellow fluorescent protein (HS-YFP) caused by extracellular addition of I^- (arrow) in FRT cells expressing SLC26A4. SLC26A4 inhibitors (YS-01; PDSinh-A01, PDSi) slow down I^- uptake and hence HS-YFP quenching. Right: summary of data showing quenching rate (QR) of HS-YFP with vehicle and SLC26A4 inhibitors at the indicated concentrations. Adapted from Guidone et al., 2022.

Figure 46. Contribution of pendrin to apical pH in bronchial epithelial cells. Apical pH measured with the large volume ex situ assay in non-CF and CF cultured bronchial epithelia treated for 72 h with the IL-17/TNF-α combination. Where indicated, in the last 3 h, epithelia were stimulated with/without isoproterenol (100 nM) in the absence/presence of YS-01 (5 μM). *, $p < 0.05$; **, $p < 0.01$; ***, $p < 0.001$; ns, not significant (ANOVA with Tukey's post hoc test). Adapted from Guidone et al., 2022.

Figure 47. Analysis of isoproterenol effect on apical pH in HCO_3^--rich condition. The graphs report the apical pH (large volume ex situ assay) measured in non-CF (left) and CF (right) bronchial epithelia kept in HCO_3^--rich basolateral media. All epithelia were treated for 72 h with IL-17/TNF-α. Where indicated, epithelia were stimulated with basolateral isoproterenol (100 nM) in the absence/presence of ouabain (200 μM). **, $p < 0.01$; ***, $p < 0.001$; ns, not significant (ANOVA with Tukey's post hoc test). Adapted from Guidone et al., 2022.

Figure 48. Analysis of isoproterenol effect on apical pH in HCO_3^--free condition. The graphs report the apical pH (large volume ex situ assay) measured in non-CF (left) and CF (right) bronchial epithelia kept in HCO_3^--free basolateral media. All epithelia were treated for 72 h with IL-17/TNF-α. Where indicated, epithelia were stimulated with basolateral isoproterenol (100 nM) in the absence/presence of ouabain (200 μM). ***, $p < 0.001$; ns, not significant (ANOVA with Tukey's post hoc test). Adapted from Guidone et al., 2022.

Figure 49. ASL pH measurement in small volume by SNARF-1 staining. Top: measurement of pH on the apical surface (small volume in situ pH assay) in non-CF (left) and CF (right) epithelia treated with/without IL-17/TNF-α (72 hours). Where indicated, the basolateral solution included isoproterenol (100 nM, for 3 hours before experiment). The scatter dot plots show pH values for the indicated conditions. ***, $p < 0.001$ versus untreated cells (no cytokine treatment, no isoproterenol). ##, $p < 0.01$; ###, $p < 0.001$ versus cells with cytokine treatment/without isoproterenol (Kruskal-Wallis and Dunn's test). Bottom: the images show the pattern of SNARF-1 dextran distribution on epithelial surface for the indicated conditions. Adapted from Guidone et al., 2022.

Figure 50. Effect of HCO_3^- transport on airway surface properties. The graphs show the results of FRAP experiments on bronchial epithelia that were pretreated for 72 hours with/without IL-17/TNF-α. Data were obtained in non-CF (left) and CF (right) bronchial epithelia with HCO_3^- or Hepes buffered media on the basolateral side for 3 hours before measurements. ***, $p < 0.001$; ns = not significant (Kruskal-Wallis and Dunn's test). Adapted from Guidone et al., 2022.

Figure 51. Effect of pendrin inhibition on airway surface properties. The graphs show the results of FRAP experiments on bronchial epithelia that were pretreated for 72 hours with/without IL-17/TNF-α. Data from experiments in non-CF (left) and CF (right) bronchial epithelia with YS-01 (5 μM) added to the basolateral side for 3 hours before measurements. *, $p < 0.05$; ***, $p < 0.001$; ns = not significant (Kruskal-Wallis and Dunn's test). Adapted from Guidone et al., 2022.

Figure 52. Effect of CFTR rescue on airway surface properties. The graphs show the results of FRAP experiments on F508del/F508del CF bronchial epithelia that were pretreated for 72 hours with/without IL-17/TNF-α. Where indicated, epithelia were treated with the VX-809 (1 μM) plus VX-445 (5 μM) or vehicle in the last 24 hours before measurements. All epithelia were stimulated with isoproterenol (100 nM, basolateral) for 3 hours. **, $p < 0.01$ (Kruskal-Wallis and Dunn's test). Adapted from Guidone et al., 2022.

Figure 53. Graphical model of the switch from absorptive to secretory state induced by isoproterenol in IL-17/TNF-α treated cells. The illustration shows the proposed changes in ion transport that occur when epithelia treated with IL-17/TNF-α are stimulated with the β-adrenergic agonist. Adapted from Guidone et al., 2022.

7. LIST OF ABBREVIATIONS

air liquid interface (ALI)
airway surface liquid (ASL)
alpha-1 antytripsin (AAT)
anti-sigma factor antagonist domain (STAS)
antigen-presenting cells (APCs)
apical membrane (AM)
ATP-Binding Cassette (ABC)
bronchioalveolar stem cells (BASCs)
bicarbonate (HCO_3^-)
calcium (Ca^{2+})
channel-activating proteases (CAPs)
chloride (Cl^-)
chronic obstructive pulmonary disease (COPD)
ciliary beat frequency (CBF)
cyclic-AMP (cAMP)
cystic fibrosis (CF)
Cystic Fibrosis Transmembrane conductance Regulator (CFTR)
dendritic cells (DCs)
fluorescence recovery after photobleaching (FRAP)
hypothiocyanite ($OSCN^-$)
innate lymphoid cells (ILCs)
inner dynein arms (IDA)
interferon-γ (IFNγ)
interleukin (IL)
invariant natural killer T (iNKT)
iodide (I^-)
lipopolysaccharide (LPS)
major histocompatibility complex (MHC)
membrane-spanning domain (MSD)
micro particle transport (MPT)
mucociliary clearance (MCC)
mucus layer (ML)
N-terminal domain (NTD)
naïve T lymphocyte (Th0)
nucleotide binding domain (NBD)
outer dynein arms (ODA)
pathogen-associated molecular patterns (PAMPs)
pattern-recognition receptors (PRRs)
periciliary liquid (PCL)
potassium (K^+)
primary ciliary dyskinesia (PCD)
protease activated receptors (PARs)

protease nexin-1 (PN-1)
protein kinase A (PKA)
protons (H^+)
pseudohypoaldosteronism (PHA)
Pulmonary Neuroendocrine Cells (PNeC)
Rho kinase (ROCK)
secretory leukocyte protease inhibitor (SLPI)
short palate lung and nasal epithelial clone 1 (SPLUNC1)
single-cell RNA-sequencing (scRNAseq)
sodium (Na^+)
T helper type-1 (Th1)
T helper type-17 (Th17)
T helper type-2 (Th2)
thiocyanate (SCN^-)
Toll-like receptors (TLRs)
transmembrane domain (TMD)
tumor necrosis factor-α (TNF-α)
tumor necrosis factor-β (TNFβ)
vacuolar-ATPase (V-ATPase)